Engineering of Hybrid Quantum Diamond Structures for Sensing Applications

Von der Fakultät Mathematik und Physik der Universität Stuttgart zur Erlangung der Würde eines Doktors der Naturwissenschaften (Dr. rer. nat.) genehmigte Abhandlung

Vorgelegt von

Seyed Ali Momen Zadeh
aus
Esfahan (IRAN)

Hauptberichter: Prof. Dr. Jörg Wrachtrup
Mitberichter: Prof. Dr. Peter Michler

Tag der mündlichen Prüfung: 10.02.2017

3. Physikalisches Institut der Universität Stuttgart
2017

> "No fisherman shall ever find a pearl in a small brook
> which empties into a pool."
>
> Another Birth, Foroogh Farrokhzad (1935-1967)

Contents

Acknowledgments 7

List of Abbreviations 11

Summary 13

Zusammenfassung 17

1. Introduction 21

- 1.1. Diamond basic properties and synthesis . . . 21
  - 1.1.1. Lattice properties . . . 21
  - 1.1.2. Phononic and thermal properties . . . 22
  - 1.1.3. Electronic and optical properties . . . 22
  - 1.1.4. Synthesis techniques . . . 23
- 1.2. Nitrogen vacancy center (NVC) in diamond . . . 24
  - 1.2.1. Basic optical and spin properties . . . 25
  - 1.2.2. Creation techniques . . . 29
  - 1.2.3. Photon collection efficiency . . . 29
  - 1.2.4. Applications . . . 31

2. Diamond Micro- and Nanofabrication Techniques 33

- 2.1. Diamond thin films . . . 34
- 2.2. Electron beam lithography . . . 36
  - 2.2.1. Creation of NVC arrays via PMMA nano-apertures . . . 37
  - 2.2.2. Patterning flowable oxide (FOX 25) . . . 40
- 2.3. Reactive Ion Etching - Inductively-Coupled Plasma (RIE-ICP) . . . 41
  - 2.3.1. General principles of plasma etching . . . 41
  - 2.3.2. Applications of RIE-ICP process . . . 43
- 2.4. Summary and outlook . . . 46

3. Hybrid Diamond-NVC Photonic Structure 49
- 3.1. Theoretical backgrounds . . . 50
  - 3.1.1. Optical two-level system . . . 51
  - 3.1.2. Optical three-level system . . . 52
  - 3.1.3. Optical fibers . . . 54
  - 3.1.4. NVC as an electric dipole inside a fiber . . . 56
- 3.2. FEM simulations of diamond photonic structures . . . 57
  - 3.2.1. Geometry of the nanopillar . . . 60
  - 3.2.2. Position of the NVC inside the nanopillar geometry . . . 62
  - 3.2.3. Emission wavelength dependency . . . 63
- 3.3. Realization of the Nanopillar-NVC hybrid system . . . 63
- 3.4. Experimental characterization . . . 67
  - 3.4.1. Optical benchmark measurements . . . 67
  - 3.4.2. Spin-dephasing times measurements . . . 72
- 3.5. Summary and outlook . . . 76

4. Hybrid Diamond-NVC Mechanical Structures 79
- 4.1. Theoretical background . . . 80
  - 4.1.1. Mechanical degrees of freedom . . . 80
  - 4.1.2. Classical and quantum mechanical oscillators . . . 80
  - 4.1.3. Diamond mechanical properties . . . 82
  - 4.1.4. Interaction of NVC with mechanical degrees of freedom . . . 82
- 4.2. Thin circular diamond membrane and the embedded NVCs . . . 88
  - 4.2.1. Continuum mechanics and spin-stress model . . . 88
  - 4.2.2. Fabrication procedure . . . 91
  - 4.2.3. Experimental characterization . . . 94
  - 4.2.4. NVC-oscillator system . . . 99
- 4.3. Diamond microcantilevers and embedded NVCs . . . 102
  - 4.3.1. Cantilevers in continuum mechanics . . . 104
  - 4.3.2. Mechanical quantum bus . . . 105
  - 4.3.3. Fabrication procedure . . . 110
  - 4.3.4. Experimental characterization . . . 111
- 4.4. Summary and outlook . . . 112

A. Measurement Setup 117

Bibliography 121

List of Figures **139**

List of Publications **153**

Acknowledgments

This thesis as any other research project is not a unitary effort. Indeed, due to the interdisciplinary nature of this work, many people have been involved and greatly helped. Here, I try to give my best gratitude to them, without whom I was not able to write this thesis now!

- First of all, my best gratitude goes to PROF. DR. JÖRG WRACHTRUP, for giving me the opportunity to work in his internationally-famous research group. Importantly, I am thankful to him for the freedom and support he gave me to work during my PhD thesis and the trust he made on my work. In his group I did not only do my PhD work and publish several papers, however, I could also develop my character! I would like to also thank PROF. DR. PETER MICHLER for accepting to be the second supervisor of this thesis. Similarly, I am thankful to PROF. DR. GÜNTER WUNNER for being the chairman of the PhD defense session.

- During this thesis, I did not have a senior postdoc as the daily-basis fellow. Although this was sometimes sort of annoying, I could gain so much out of this fact instead. I could have the opportunity to take advantage of the wide-range knowledge of the people in this institute, and other research centers. I am thankful to DR. ANDREJ DENISENKO for his help regarding diamond, fabrication and NVC formation in diamond. Not only he helped me a lot with creation of NVCs, he was the person I could talk with whenever I was encountering a blind tedious problem in my cleanroom activities! A huge portion of my acknowledgments, humbly, goes to DR. RAINER STÖHR, who was always for me there. He was a great help during the nanopillar project, as well as writing this thesis. I am thankful to him also for his great proofreading. He offered me his help, whenever needed, with ZERO claim for any credit! Danke Rainer! I am thankful to DR. DURGA DASARI for the great discussions about the NVC-mechanical systems. His great expertise in theoretical physics is fascinating for me. A great acknowledgment is also addressed to DR. PHILIPP NEUMANN for the great collaboration on the NVC-mechanical system project. Whenever I could talk with him, I could easily realize that, he knows the NVC very well! I would like to send my best regards to DR. MARCUS DOHERTY from the Australian National University, Australia, for the great collaboration in the NVC-mechanical system subject. That was really amazing to collaborate with him.

- During the past years of working at the PI3 labs, I could meet several students and postdoc fellows coming originally from different corners of the world. That was awesome to work with them, sometimes to the midnight, and learn many things from them. One of the first gentlemen I could see was DR. PETER SIYUSHEV. Although our overlapping time was kind of short, I could learn many fundamental things in optics from him. I would like to also appreciate Dr. Ilja Gerhardt, Dr. Bernhard Grotz, Kim Kafenda, Dr. Sen Yang, Thai Hien Tran, Michael Klas, Julia Michl, and ... . I would like to express my gratitude to Dr. Helmut Fedder for the great help in the measurement software (Pi3diamond) and the measurement hardware such as FPGA etc. I am thankful also to Dr. Friedemann Reinhard for the nice collaboration in the nanopillar project. Additionally, many thanks go to Dr. Roman Kolesov, Thorsten Rendler, Matthias Widmann and Thomas Wolf for their assistance in the measurements, and fruitful discussions.

• I would like to express my special gratitude to Andreas Brunner for his initial efforts in the nanopillar development process as well as his great collaboration for the T_1 measurements at low temperature.

• An important part of this thesis was spent under the yellow light and special suits in the cleanrooms of PI3 and Max Planck Institute (MPI) for Solid State Research. For the great technical support of the cleanroom of PI3, I would like to send my deep acknowledgments to Stephan Hirschmann, Dr. Rolf Reuter, and Dr. Andrea Zappe. I could learn a lot by being in the cleanrooms of MPI. Foremost I could enjoy the great organization and friendly support of the technicians there. I am very much thankful to Thomas Reindl, Ulrike Weizmann, Achim Güth, Marion Hagel, and Bernhard Fenk for their great support. Definitely I should thank Dr. Jürgen Weiss for his great management and organization as well. I appreciate very much the people who taught me how to play efficiently with the Eline apparatus. In this way, I would like to thank Dr. Federico Paolucci, Dr. Konstantinos Panos, Prof. Dr. Klas Lindfors, and Dr. Alexander Hoyer for sharing their great expertise with me. Additionally I am very grateful to Monika Ubl for her great and friendly technical support.

• The excellent help of the people who only got my design file and order paper and could deliver me fantastic equipments, should not be left without any acknowledgment! Hereby, I am happy to thank the mechanical workshop of the physics department headed by Mr. Ralf Kamella, the glass workshop headed by Mr. Frank Schreiber, Mr. Werner Braun from the electronic workshop, and mechanical workshop of MPI headed by Mr. Thomas Frey.

• I am sure that the reader is aware of the great weight of paper works and bureaucratic affairs in Germany. Hereby, I would like to thank Ms. Claudia Unger, secretary of PI3, for her numerous great helps with paper works in the last years. Danke Frau Unger!

• Here, I would like to send my thanks to a gentleman who was my office mate, lab mate, collaborator, and a friend! I would like to thank Felipe for being such a nice buddy, for many rounds of fruitful discussions, many implantation and annealing efforts, meticulous proofreadings, and happy times we could create for ourselves, even in spite of the difficult situations we encountered. Obrigado Sr. Felipe Fávaro de Oliveira!

- I am happy to thank Dr. Amit Finkler and Anurag Kanase as the successors of my activities in the cleanroom. I enjoyed this short but nice overlap.
- Many thanks go to Ingmar Jakobi for the nice collaboration on the NVC pair implantation mask project.
- At this nice moment, I would like to thank my wife who joined me at the last year of this journey. Big thanks for the nice accompany and understanding she made. Thanks for your pure love during all the happy and hard times. Merci Fati! Merci!
- I must thank my parents and sisters here, but I do not know how I can manage it! I just wish to send my enormous acknowledgment to whom who were always with me even while being 5000 km away! I express my best appreciation to them for the great financial and emotional support whenever was needed, the great walk they did with me during my life, and many other things. Especially to my parents, who were always devotedly helping and supporting.
- I would like to also address my deep appreciation to my best friends, Ahmad & Maedeh, who were always beside my shoulders in the happy and uncomfortable times since my migration to Germany.
- Finally, I would like to thank all the members of PI3 who helped me during my PhD thesis. Your help is not forgotten.

List of Abbreviations

AFM	atomic force microscopy
AOM	acousto-optic modulator
APD	avalanche photodiode
BS	beam splitter
CMT	continuum mechanics theory
CPMG	Carr Purcell Meiboom Gill
CVD	chemical vapor deposition
DAQ	data acquisition
DEER	double electron-electron resonance
DM	dichroic mirror
DPSS	diode pumped solid state
EBL	electron beam lithography
ESR	electron spin resonance
FEM	finite elements method
FIB	focused ion beam
FOX	flowable oxide
FPGA	field-programmable gate array
FWHM	full width at half maximum
HBT	Hanbury Brown and Twiss
HF	hydrofluoric acid
HPHT	high pressure high temperature
HSQ	hydrogen silsesquioxane
IPA	isopropanol
LDOS	linear density of states
LT	low temperature
MDP	minimum detected pressure
MEMS	micro-electromechanical system
MIBK	methyl isobutyl ketone
MW	microwave
NA	numerical aperture

NEMS	nano-electromechanical system
NEP	N-Ethylpyrrolidone
NVC	nitrogen vacancy center
ODMR	optically-detected magnetic resonance
PCB	printed circuit board
PMMA	Poly(methyl methacrylate)
PSB	phonon sideband
PSF	point spread function
QED	quantum electrodynamics
RIE-ICP	reactive ion etching - inductively-coupled plasma
RMS	root mean square
SAW	surface acoustic wave
SEM	scanning electron microscopy
SMF	single mode fiber
SQL	standard quantum limit
TIR	total internal reflection
TMAH	tetramethylammonium hydroxide
UV	ultraviolet
XPS	x-ray photoelectron spectroscopy
ZPF	zero-point fluctuation
ZPL	zero phonon line

Summary

Fostering the mind-blowing achievements of quantum science and technology for the benefit of human society has been the motivation for generations of scientists. Quantum communication featuring higher security and quantum sensing with unprecedented sensitivity are only two examples of how this work is paving the way into a brighter future. For such complex tasks, however, it is not easy to find a single physical component being capable of fulfilling all criteria required for a multifunctional device. Instead, most approaches are based on the combination of multiple components by joining classical as well as quantum mechanical systems. Each of those sub-systems accomplishes a certain task based on its individual physical properties so that, when combined, their complementary functionalities add up to a revolutionarily new type of device. These so-called "hybrid" architectures typically include components such as photonic elements, magnetic materials, superconducting circuits, microwave resonators, mechanical nanostructures, and qubits. Among others, nitrogen vacancy centers (NVCs) in diamond have been utilized as qubits playing a key role in hybrid structures.

Diamond has been known since ancient times as a host substrate with outstanding characteristics. Today we know that this is in part due to a large energy band gap and therefore a unique optical transmission spectrum, a large Young's modulus, and low intrinsic dissipation, and chemical and biochemical inertness. Furthermore, we know that NVCs in diamond exhibit ultra-long coherence times and superb photostability even at room temperature, setting them apart from other competitors like quantum dots or single molecules. It is therefore not surprising that, diamond photonic and mechanical structures play a highlighted role as components in hybrid systems featuring NVCs.

Traditional semiconductor fabrication and structuring techniques as used e.g. for silicon and gallium arsenide cannot be directly applied to diamond substrates. In recent years, this has set a serious obstacle against further usage of diamond towards the goal of developing multifunctional quantum devices. For one thing, growth of ultra-pure, high-quality, single-crystalline diamond substrates is time-consuming, expensive, and requires very specialized equipments. Further, top-down fabrication approaches like lithography and etching techniques involving diamond substrates are more cumbersome and less efficient in comparison to the case of above-mentioned semiconductors. Besides several recent attempts reporting breakthrough developments to resolve these concerns, various deficiencies still exist which limit

the further application of diamond structures in hybrid architectures.

In this PhD thesis, development of novel hybrid quantum systems featuring engineered diamond photonic and mechanical structures and implanted NVCs as quantum nanosensors, towards quantum sensing applications will be presented. In particular, analytical and numerical calculations, fabrication, and characterization of i) conically-tapered diamond nanopillars, ii) thin circular diamond membranes and iii) diamond microcantilevers, all hosting embedded NVCs, will be demonstrated. Optimizing the sensitivity of magnetic field measurement (magnetometry) via augmenting the photon collection efficiency of the embedded NVCs is focused in i), where in ii) and iii) interaction of the embedded NVCs with the mechanical degrees of freedom of the host diamond structures is considered.
This thesis is therefore structured as follows:

• In the first chapter, introductory information about diamond and NVCs will be given. In a brief way, properties of diamond will be discussed, followed by reviewing different methods of diamond synthesis. Then, optical and spin properties of NVCs will be shortly reviewed, which will be continued by explaining the generation techniques of NVCs. At the end, interaction of NVCs with external degrees of freedom will be explained, based on which their applications will be briefly listed.

• As mentioned, one of the most important highlights of this thesis is to develop various fabrication techniques enabling novel hybrid diamond platforms. Therefore, in the second chapter, optimized fabrication techniques specifically designed for diamond substrates will be presented. In this way, initially, production of primarily-used diamond substrates in this thesis, i.e. diamond thin films (thickness $\sim$ 30 μm) will be schematically explained. Then, the two essential nanofabrication tools exploited in the course of this thesis, i.e. electron beam lithography and plasma etching (reactive ion etching - inductively-coupled plasma; RIE-ICP) techniques, will be illustrated. The developed recipes based on these procedures will be shown to enable the engineering of various structures from nanoscale to millimeter scale, and from overlay ones on top of the diamond substrate to topographic diamond structures. At the end, several exemplary fabricated structures following their fabrication recipes will be demonstrated.

• Besides other applications of NVCs, they have been shown as exquisite nanosensors for internal and external magnetic fields. In the third chapter, a novel hybrid platform consisting of a single NVC as the magnetometer and the hosting diamond photonic structure, namely conically-tapered nanopillar, will be presented. First, theoretical backgrounds of the photophysics of NVCs, as well as optical waveguides will be briefly given. Then, analytical and numerical simulations will be shown to achieve the optimized geometry for the nanopillar structure to enhance the photon collection efficiency of the embedded shallow NVCs. Based on them, conically-tapered diamond nanopillars with the approximate geometry of 400 nm, 900 nm, and 1.2 μm of top diameter, bottom diameter, and height, respectively, are set as the target photonic structure. As the next step, the fabrication of such a hybrid system will be illustrated. By characterizing them, it will be found that they can deliver net fluorescence rate of $\approx 1.7 \times 10^6$ counts/sec from single NVCs, which features $\approx$ 13 times enhancement in comparison to that of NVCs under the nonstructured diamond surface. Importantly, due to this geometry and the employed fabrication method, it will be shown that no negative effect on the optical properties as well as spin coherence times of NVCs is observed. So far, these two important achievements can yield in $\sim$ 3-fold enhancement in magnetometry sensitivity using NVCs. At the end, this developed nanostructure will be assessed at low temperatures. The T_1 relaxation time measurement of a single NVC inside a nanopillar geometry from room temperature to $\sim$ 5 K will be shown to vary from $\approx$ 5 ms to $\approx$ 300 ms, respectively. It will be shown that the temperature-dependency of the T_1 relaxation times of shallow NVCs can give information about their phononic environment in comparison to that of the bulk NVCs.

• In the fourth chapter, hybrid diamond mechanical systems including embedded NVCs will be presented. A short introduction about different mechanical degrees of freedom, as well as mechanical oscillators in classical and quantum mechanics, and mechanical properties of diamond will be presented. Then, interaction of different mechanical degrees of freedom, such as strain and periodic vibration, with the spin interface of NVCs will be discussed. Afterward, two different hybrid systems based on two diamond mechanical objects i.e. I) thin circular diamond membrane and II) mechanically-coupled diamond microcantilevers will be shown.

I) Fabrication and functionality of thin circular diamond membrane with the diameter of $\approx$ 1.1 mm, thickness of $\approx$ 1.2 μm, and surface roughness of $\approx$ 0.4 nm will be demonstrated. Prior to present the experimental results, extensive continuum mechanics theory background will be discussed to derive the formula explaining the response of the system to the applied pressure (stress). Then, the fabrication process based on developed Ar/SF$_6$ plasma and an auxiliary diamond substrate as the designed etching mask will be mentioned. Next, the embedded NVCs radially at the center of the membrane will be shown as nanosensors of different mechanical degrees of freedom of the membrane. The fluorescence profile and ground-state spin interface of individual embedded NVCs will be employed to detect the deflection of the membrane under static applied pressure and in-resonance vibration, as well as its residual stress. In this way, e.g. $\approx$ 14 μm of deflection and $\approx$ 2.2 MHz of ESR frequency shift for 1 bar of applied static pressure will be shown. By the same method, measuring $\approx$ 50 MPa of radial residual stress of the membrane will be demonstrated. Similarly, the minimum detected pressure by means of the optical interface of NVCs is registered to be $\approx$ 40 Pa, revealing $\approx$ 6 Pa/$\sqrt{\text{Hz}}$ of photon shot noise limit on the pressure sensitivity. Relying on these values, it will be discussed that the presented hybrid structure using NVCs shows similar performance compared with state-of-the-art pressure sensing devices based on MEMS/NEMS. Moreover, this hybrid arrangement will be characterized as a spin-oscillator system. Within this frame, further fundamental investigations on spin-phonon coupling regime will be pursued. In this regard, analytical calculations following experimental observations about the spin-phonon coupling strength will be shown.

II) So far, the interaction of NVCs with mechanical degrees of freedom of the host structure is studied. This interaction can be seen to act locally, i.e. within a single node. In the next step, multiplying and coupling of these nodes will be addressed. To that aim, another diamond mechanical object, i.e. an array of diamond microcantilevers will be presented. It will be discussed that this mechanically-coupled microcantilever geometry can play a role as a mechanical quantum bus to couple two distant NVCs, thus to scale up the hybrid NVC-mechanical systems. In this way, mechanically-coupled diamond microcantilevers will be analytically and numerically discussed and optimized. Then, to realize these structures, a delicate fabrication process based on double-resist electron beam lithography and RIE-ICP procedures will be presented. Next, by performing benchmark measurements, the resonance frequency of the microcantilevers as well as the corresponding quality factors will be obtained. Importantly, by observing the vibration spectrum of this system, their mechanical coupling concept will be proven.

At the end, a brief explanation about the measurement setup will be provided, which will be followed by bibliography.

Zusammenfassung

Die erstaunlichen Errungenschaften der Quantenforschung und Quantentechnologie für den gesellschaftlichen Fortschritt zu nutzen ist Antrieb und Motivation für ganze Generationen von Wissenschaftlern. Quantenkommunikation, welche die sichere Übermittlung von Daten ermöglicht, und Quantenmessverfahren mit beispielloser Sensitivität sind nur zwei Beispiele dafür, wie diese Arbeiten den Weg in eine neue Zukunft ebnen. Um solche komplexe Aufgaben zu bewältigen, ist es jedoch nicht möglich, ein einzelnes physikalisches System zu finden welches alle nötigen Kriterien für ein multifunktionales Bauteil erfüllt. Die meisten Ansätze basieren daher auf einer Kombination von mehreren Komponenten welche sowohl klassische wie auch quantenmechanische Systeme verbinden. Jedes dieser Teilsysteme erfüllt eine gewisse Aufgabe gemäß seinen individuellen physikalischen Eigenschaften, so dass durch die Kombination ihrer komplementären Funktionalitäten ein revolutionär neues Bauteil entsteht. Diese sogenannten Hybrid-Architekturen beinhalten typischerweise Komponenten wie photonische Elemente, magnetische Materialen, supraleitende Schaltkreise, Mikrowellen Resonatoren, mechanische Nanostrukturen und Qubits. Unter anderem spielen in Hybridstrukturen Stickstoff-Fehlstellen Zentren (NV Zenter, engl. nitrogen vacancy center, NVC) in Diamant eine zentrale Rolle als Qubits. Diamant ist bereits seit Jahrhunderten für seine einzigartigen Eigenschaften bekannt. Heute wissen wir, dass dies zum Teil auf eine große Energiebandlücke und das damit verbundene optische Transmissionsspektrum, ein großes Elastizitätsmodul, niedrige Dissipation sowie chemische und biologische Inertheit zurückgeht. Darüber hinaus wissen wir, dass anders als beispielsweise bei Quantendots und einzelnen Molekülen, NV Zentren in Diamant selbst bei Raumtemperatur besonders hohe Kohärenzzeiten und ausgezeichnete Photostabilität ausweisen. Es ist daher nicht verwunderlich, dass photonische und mechanische Diamantstrukturen eine exponierte Rolle als Komponenten in Hybridstrukturen mit NV Zentren spielen.

Herkömmliche Herstellung und Strukturierungsverfahren der Halbleitertechnik wie sie beispielsweise für Silizium und Galliumarsenid verwendet werden, können nicht direkt auf Diamant übertragen werden. In den vergangenen Jahren stellte dies ein großes Hindernis bei der Integration von Diamant in neuartige multifunktionale Quantenbauteile dar. Zum einen ist das Wachstum von hochreinen, hochqualitativen, und einzelkristallinen Diamantsubstraten sehr zeitintensiv und teuer und benötigt außerdem hochspezialisierte Geräte. Zum anderen ist die Anwendung von Herstellungsverfahren nach dem Top-down-Prinzip wie beispielsweise Lithographie und Ätztechniken bei Diamantsubtraten deutlich mühsamer und weniger effizient als bei Halbleitermaterialien. Trotz verschiedener bahnbrechender Erfolge auf diesem Gebiet, verbleiben diverse Einschränkungen welche die Anwendung von Diamant in Hybridstrukturen limitieren.

In dieser Doktorarbeit wird die Entwicklung von neuartigen Quantenhybridstrukturen basierend auf photonischen und mechanischen Diamantstrukturen mit implantierten NV Zentren und deren Anwendung im Gebiet der Quantensensorik vorgestellt. Insbesondere werden analytische und numerische Berechnungen sowie Herstellung und Charakterisierung von i) konisch zulaufenden Diamant-Nanosäulen ii) dünnen kreisförmigen Diamantmembranen und iii) freistehenden mikrometergroßen Diamant-Cantilevern, welche alle mit NV Zentren dotiert sind präsentiert. Die Sensitivität bei der Messung von magnetischen Feldern (Magnetometrie) durch die Verbesserung der Photonenkollektionseffizienz zu optimieren steht im Fokus von i) wohingegen bei ii) und iii) die Wechselwirkung der eingebetteten NV Zentren mit den mechanischen Freiheitsgraden des Diamantsubstrats im Vordergrund steht.

Die vorliegende Arbeit ist daher wie folgt gegliedert:

- Das erste Kapitel gibt einen Überblick über Diamant und NV Zentren. In kompakter Weise werden hier die relevanten Eigenschaften und die verschiedenen Arten der Herstellung von Diamantsubstraten diskutiert. Anschließend werden die optischen sowie die Spin-Eigenschaften von NV Zentren zusammen mit Verfahren zu deren Herstellung erläutert. Zum Schluss wird die Wechselwirkung von NV Zentren mit externen Freiheitsgraden erklärt und deren Anwendung aufgezeigt.
- Wie bereits erwähnt ist eines der zentralen Themen dieser Arbeit die Entwicklung diverser Herstellungsverfahren um Diamantstrukturen in neuartige Hybridplattformen zu integrieren. Im zweiten Kapitel werden daher speziell für Diamant entwickelte und optimierte Strukturierungstechniken präsentiert. Zunächst wird die Präparation von rund 30 μm dicken Diamantfilmen, welche als Ausgangsmaterial für alle weiteren Experimente dienen, schematisch dargestellt. Darauf folgend werden die zwei wichtigsten Werkzeuge der Nanostrukturierung - Elektronenstrahllithographie und Plasmaätzen (reaktives Ionenätzen mit induktiv gekoppeltem Plasma, RIE-ICP) - dargestellt. Die auf diesen Techniken aufbauenden Verfahren ermöglichen die Entwicklung von diversen Nano- und Mikro-Strukturen welche sowohl in topographischen Diamantstrukturen wie auch in Strukturen auf der Diamantoberfläche resultieren. Abschließend werden mehrere exemplarische Strukturen gemeinsam mit ihren Herstellungsverfahren vorgestellt und diskutiert.
- Neben anderen Anwendungen haben sich NV Zentren als hervorragende Nanosensoren für interne und externe magnetische Felder bewiesen. Im dritten Kapitel wird eine neue Hybridplattform bestehend aus einem einzelnen NV Zentrum als Magnetometer, welches in eine

konisch zulaufende Diamant-Nanosäule als photonische Struktur integriert ist, vorgestellt. Zunächst wird dabei der theoretische Hintergrund der Photophysik von NV Zentren sowie der von optischen Lichtleitern diskutiert. Anschließend werden analytische und numerische Simulationen besprochen welche dazu dienen, die optimale Geometrie für eine maximale Photonenkollektionseffizienz der Lichtleiter mit oberflächennahen NV Zentren zu finden. Darauf basierend wurden konisch zulaufende Nanosäulen mit einem unteren Durchmesser von etwa 900 nm, einem oberen Durchmesser von etwa 400 nm und einer Höhe von rund 1.2 μm als die Vorgabe für die experimentelle Umsetzung identifiziert. Im nächsten Schritt wird die Herstellung dieser Strukturen aufgezeigt. Ihre Charakterisierung ergab eine Fluoreszenzrate von $\approx 1.7 \times 10^6$ 1/s pro NV Zentrum was eine Erhöhung um Faktor 13 im Vergleich zu NV Zentren unter einer unstrukturierten Diamantoberfläche darstellt. Wichtig ist dabei, dass aufgrund der speziellen Geometrie und der verwendeten Strukturierungsverfahren kein negativer Einfluss auf die optischen Eigenschaften und die Spin-Kohärenzzeiten der NV Zentren beobachtet wurde. Diese zwei wichtigen Erfolge führen zu einer Verbesserung der Magnetometriesensitivität von NV Zentren um einen Faktor 3. Abschließend werden diese Nanostrukturen bei tiefen Temperaturen untersucht. Dabei zeigt sich, dass die T_1 Relaxationszeit eines einzelnen NV Zentrums innerhalb der Nanosäule von 5 ms bei Raumtemperatur zu 300 ms bei einer Temperatur von 5K ansteigt. Es wird weiterhin gezeigt werden, dass diese Temperaturabhängigkeit der T_1 Relaxationszeit von oberflächennahen NV Zentren Informationen über deren phononische Umgebung enthält, welche sich von der von tiefer implantierten NV Zentren unterscheidet.

- Im vierten Kapitel werden mechanische Hybridstrukturen mit integrierten NV Zentren diskutiert. Zunächst wird eine kurze Einführung in unterschiedliche mechanische Freiheitsgrade sowie mechanische Oszillationen in klassischen und quantenmechanischen Systemen und den mechanischen Eigenschaften von Diamant gegeben. Darauf aufbauend wird die Wechselwirkung von unterschiedlichen mechanischen Freiheitsgraden wie Dehnung und periodische Vibrationen mit dem Spin des NV Zentrums besprochen. Danach werden zwei unterschiedliche Hybridsysteme basierend auf zwei mechanischen Diamantstrukturen präsentiert: I) Dünne kreisförmige Diamantmembranen und II) mechanisch gekoppelte Diamant Mikrocantilever. I) Zunächst wird die Herstellung und die Funktionalität von dünnen kreisförmigen Membranen mit einem Durchmesser von $\approx$ 1.1 mm, einer Dicke von $\approx$ 1.2 μm und einer Oberflächenrauigkeit von $\approx$ 0.4 nm erläutert. Vor der Präsentation der experimentellen Ergebnisse wird ein umfangreicher kontinuumsmechanischer Hintergrund gegeben, um die Formeln, welche die Reaktion des Systems auf angelegten Druck beschreiben, abzuleiten. Anschließend wird das eigens hierfür entwickelte Herstellungsverfahren welches auf einem Ar/SF_6 Ätzprozess mit einem als Ätzmaske ausgebildeten zweiten Diamanten basiert, vorgestellt. Es wird weiter gezeigt werden, wie die im Zentrum der Membran eingebetteten NV

Zentren als Nanosensoren für mechanische Freiheitsgrade der Membran eingesetzt werden können. Das Fluoreszenzprofil sowie der Spin des Grundzustandes einzelner NV Zentren wird dabei zur Messung der Auslenkung der Membran unter statischem Druck sowie resonanter Schwingungen und remanenter Spannung genutzt werden. Dabei wird eine Auslenkung von $\approx 14\ \mu$m und eine ESR-Frequenzverschiebung von ≈ 2.2 MHz bei einem angelegten Druck von 1 bar beobachtet. Mit derselben Methode wird außerdem eine remanente Spannung der Membran von ≈ 50 MPa festgestellt. Der minimale, über das optische Interface gemessene Druck wurde auf ≈ 40 Pa bestimmt, was einer von Schottky-Rauschen beschränkten Drucksensitivität von ≈ 6 Pa/$\sqrt{\text{Hz}}$ entspricht. Basierend auf diesen Werten wird diskutiert, dass die hier vorgestellten NV-Hybridstrukturen Eigenschaften aufweisen, welche denen von MEMS/NEMS Bauteilen ebenbürtig sind. Darüber hinaus wird diese Hybridanordnung als Spin-Oszillator-System charakterisiert. Vor diesem Hintergrund werden weitere fundamentale Untersuchungen zur Spin-Phonon Kopplung durch analytische Berechnungen sowie experimentelle Ergebnisse diskutiert. II) Bisher wurde die Wechselwirkung von NV Zentren mit mechanischen Freiheitsgraden der Wirtsstruktur untersucht. Diese Wechselwirkung findet lokal, also innerhalb eines einzelnen Knotens statt. Im nächsten Schritt wird das Vervielfachen und das Koppeln solcher Knoten untersucht werden. Zu diesem Ziel wird eine weitere mechanische Diamantstruktur in Form von Mikrocantilevern vorgestellt. Es wird diskutiert werden, dass mechanisch gekoppelte Mikrocantilever wie eine Art Quanten-Bus agieren können um entfernte NV Zentren zu koppeln und um somit NV Zentren basierte mechanische Hybridstrukturen maßstäblich zu vergrößern. Hierfür werden mechanisch gekoppelte Mikrocantilever aus Diamant numerisch und analytisch untersucht und optimiert. Für deren experimentelle Realisierung wird ein neuartiges Verfahren basierend auf Doppel-Photoresist-Elektronenstrahllithograhie und RIE-ICP vorgestellt. Desweitern wird die experimentelle Bestimmung der Resonanzfrequenz und der Q-Faktoren demonstriert. Dabei wird durch die Messung der Schwingungsspektren des Systems die mechanische Kopplung zwischen den einzelnen Cantilevern nachgewiesen.

Am Schluss befindet sich eine kurze Erklärung des Messaufbaus gefolgt von dem Literaturverzeichnis.

1. Introduction

Diamond has been known due to its beauty, value, and mechanical stiffness since ancient times [1]. Back to several centuries ago, the most majestic diamonds Kooh-i-Nur and Darya-i-Nur (literally mean: mountain of light and sea of light, respectively) have been known as glorious symbols of beauty and imperial wealth [2]. In addition, diamond has been known historically as a strong material, which yields in its outstanding applications in drilling. Moreover, its unique thermal expansion and thermal conductivity range its applications further to high power devices [1]. Rapidly ongoing advances in growth and quality control of the synthetic diamonds have raised next-level applications in e.g. optical and electrical devices and pressure sensors [1, 3, 4]. In addition to a solid with incredibly excellent properties, it is also a host of hundreds of color defect centers [5, 6]. Among them, nitrogen vacancy center (NVC) [7] and silicon vacancy center (SiVC) [8] are the most famous ones, showing outstanding properties with applications ranging from classical to quantum field. Diamond and NVCs are the principal parts of this thesis. Therefore, before going through the experimental achievements of this thesis in the next chapters, a brief review about them will be given here.

1.1. Diamond basic properties and synthesis

In this section, basic properties of diamond will be reviewed. In some cases, the effect of external parameters such as pressure and temperature on those properties will be explained. Afterward, introductory information about diamond synthesis techniques will be mentioned.

1.1.1. Lattice properties

Diamond lattice is made of two inter-penetrating face centered cubic (fcc) lattices of carbon atoms, translated from each other diagonally by $\frac{a_0}{4}$ (1,1,1) (a_0 is the lattice constant of diamond). Diamond has two carbon isotopes, ^{12}C and ^{13}C, with natural abundance of 98.9% and 1.1% and nuclear spins of 0 and $\frac{1}{2}$, respectively. Lattice constant (a_0) of diamond with natural isotope contents at room temperature is measured to be $\sim$ 0.36 nm [1]. Different isotope contents and lattice impurities change this lattice constant, accordingly. The lattice constant is monotonically increasing with temperature, with the associated temperature (T)-dependent linear expansion coefficient of $\alpha = 1.08 \times 10^{-11} T^2$ (up to 500 K) [1].

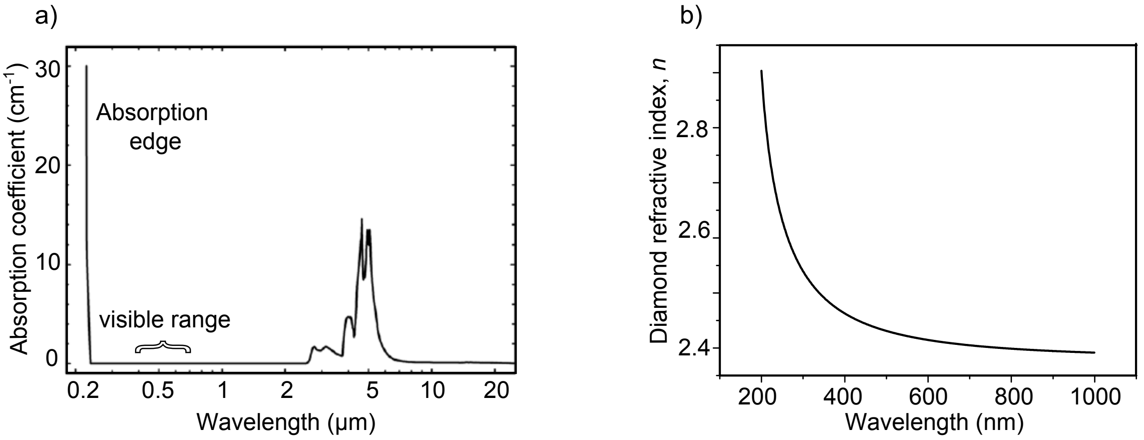

Figure 1.1.: a) Absorption coefficient of diamond is shown vs. the wavelength. As can be seen, diamond is transparent from the UV to IR region of the spectral range. Figure is taken from [9]. b) Refractive index of bulk diamond (*n*) is shown vs. the wavelength. As demonstrated, the refractive index of diamond decreases for $\approx$ 20% as the wavelength is increased from 200 nm to 1000 nm.

1.1.2. Phononic and thermal properties

Assuming no impurity in the diamond lattice, a pure bulk diamond sample does not have electrostatic dipole moments. However, a phonon distorting the diamond lattice can consequently create dipoles. Therefore, Raman spectroscopy of diamond lattice is possible, showing a sharp peak at $\approx$ 1332 cm^{-1} with full width at half maximum of 1.2 cm^{-1}, at room temperature [1]. The high contrast of the diamond Raman line offers further applications of diamond such as temperature and pressure sensing. Generally the relative shift of the Raman frequency is related to the relative change of the diamond crystal volume. For instance, applied hydrostatic compressive stress causes a linear shift in the Raman frequency. In this way, the relative shift in the Raman frequency vs. hydrostatic stress (up to 140 GPa) is given by approximately 2.8 cm^{-1}/GPa [1].

The heat conductivity of diamond is known to be the highest among the bulk materials, e.g. four times that of copper at room temperature. This value is highly dependent on temperature as well as the sample size and purity degree. For example, for a high quality pure diamond the heat conductivity is $\sim$ 15000 W/mK at $\sim$ 70 K which decays to $\sim$ 600 W/mK at $\sim$ 1000 K [1].

1.1.3. Electronic and optical properties

Pure diamond has indirect energy gap of $\approx$ 5.5 eV [1]. It is transparent in the visible and even the ultraviolet spectral range (see Figure 1.1-(a)) [1, 10]. The energy gap of diamond shifts towards higher energies under hydrostatic pressure. The relative shift of this energy vs. the applied pressure is $\approx$ 6.0 meV/GPa (for $P < 2.3$ GPa) [1]. This shift in the energy is almost an order of magnitude larger than the one caused by the phonons (see above).

By means of capacitance measurement, refractive index of 2.39 is obtained for bulk diamond sample. More precisely, refractive index of bulk diamond (n) at a given wavelength (λ) is given by [1]:

$$n^2 = 1 + \frac{0.33\lambda^2}{\lambda^2 - \lambda_1^2} + \frac{4.33\lambda^2}{\lambda^2 - \lambda_2^2}, \tag{1.1}$$

where λ_1 = 175 nm and λ_2 = 106 nm [1]. Based on Eq. (1.1), refractive index of bulk diamond vs. wavelength is plotted in Figure (1.1)-(b). Using this equation, refractive index of bulk diamond at wavelength of λ = 600 nm is achieved to be 2.41. Such a relatively high refractive index yields in reflection coefficient of $\approx$ 17 % at visible range. This information is essential for its applications in photonic devices, such as lenses and waveguides [1, 11].

For biological applications of diamond such as fluorescence imaging, it is required that the diamond substrate shows low amount of luminescence [9]. This can be managed by minimizing the amount of impurities and defect centers in diamond via optimizing its growth condition [9]. Another important criteria on the optical properties of diamond for its applications, is its low birefringence. A pure bulk diamond substrate is known to show no birefringence due to its structure properties. However, strain fields and lattice dislocations can generate birefringence in diamond. It is therefore of significant importance, to synthesize diamond substrates with low birefringence for polarization-sensitive optical applications [9]. Synthesis techniques of diamond will be explained briefly in following.

1.1.4. Synthesis techniques

While graphite is the stable allotrope of carbon at room temperature and ambient pressure, diamond cannot be naturally formed under these conditions [9]. Diamond is believed to be formed 200 kilometers below the earth's surface. Under these conditions, i.e. under high pressure and high temperature conditions (70-80 kbar of pressure and temperature of 1400-1600° C), diamond is known to be thermodynamically stable [9]. Nowadays, mimicking these conditions in industrial level is one of the most major methods to synthesize diamond substrates. This method, called as high pressure - high temperature, or shortly abbreviated as HPHT, was reported for the first time in 1955 [12]. In this method, application of a solvent metal such as iron or cobalt is essential. Using the HPHT method, mostly small diamond grains suitable for abrasive applications can be produced. Nevertheless, synthesis of large (several millimeters) ultrapure diamond substrates by means of HPHT method is also reported [9]. In this way, utilization of further getter mixtures, e.g. aluminum or titanium, helps to prevent the incorporation of impurities like nitrogen into the diamond lattice [9, 13].

Apart from the production of diamond in its thermodynamically-stable conditions via HPHT method, it can be synthesized also in its metastable regime [9]. Diamond growth by means of chemical vapor deposition (CVD) method was first reported several decades ago [9], which is nowadays another major way of diamond synthesis. In this way, growth of diamond is accomplished by using a small fraction of carbon (typically $< 5\%$) in an excess of hydrogen. By heating the molecular hydrogen up to temperatures of ~ 2000 K, a significant dissociation to the atomic hydrogen happens. Then, the diamond deposition can be performed on top of a suitable substrate. The heating process can be done via application of arc-jet, hot filament, microwave plasma, etc [9]. By controlling the purity of the deposition precursors as well as the chamber quality, CVD method offers a high-degree control of the quality of the diamond substrate [9, 14]. In addition to the quality of the diamond samples, CVD technique can yield additionally in large-scale diamond samples (~ 1 cm), as well as predefined geometries [9, 15, 16].

Diamond substrates, either natural or synthetic, can be divided into two main categories I and II, with each subcategories of a and b. This classification is usually performed based on the purity of the diamond substrate, e.g. based on the impurity concentration such as nitrogen and boron. For different types of diamond, the optical, electrical, and mechanical properties can be drastically different [9]. In this thesis, ultrapure single crystal CVD type-IIa diamond films containing less than 5 ppb (often below 1 ppb) and 1 ppb of nitrogen and boron impurities, respectively, provided by Element Six [17] are used as the starting material. For more details about the exploited diamond samples in this thesis, refer to chapter 2.

1.2. Nitrogen vacancy center (NVC) in diamond

As sources that emit only one photon at a time, i.e. single photon sources, single molecules, quantum dots, and single defects in solids can be considered. The defect centers in solids are highlighted single photon sources that are notably developed and exploited. Additionally, they get benefit from the capability to manipulate their electronic states through nanoscale control of their material host and geometry [18]. Three main criteria stand for an emitter to be employed as a single photon source [18]: i) they should be spatially isolated and addressable, b) they should be able to be optically excited, and c) their emitted photons should be collected and directed into the optical collection tools. Similar to other defect centers in diamond [6], nitrogen vacancy centers (NVCs) [7] and silicon vacancy centers (SiVCs) [8, 19] are single defect centers in diamond which are manifested to be single photon sources that fulfill these criteria. Importantly, NVC is an unbleachable stable photon source even at room temperature.

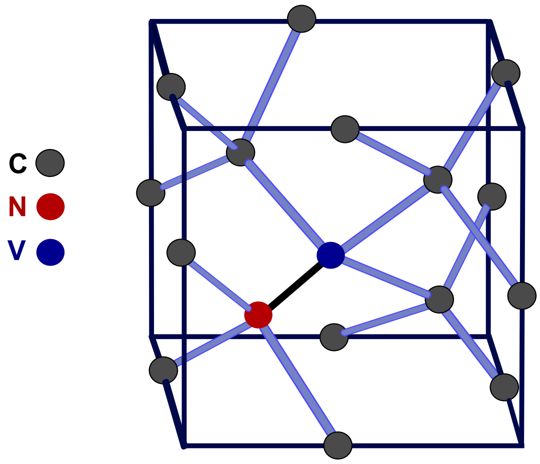

Figure 1.2.: Lattice structure of an NVC defect in diamond is depicted. As shown, NVC is formed of a substituting nitrogen impurity attached to the neighbor lattice vacancy.

Besides the eminent optical characteristics of NVC, it has an electron spin triplet ground state which can be addressed, manipulated, and readout with high fidelity [20].

NVC is a point lattice defect in diamond which is formed of a nitrogen impurity substituting a carbon atom, attached to the neighbor lattice vacancy (see Figure 1.2) [21]. It has three charge states, over which only the negatively-charged one is investigated in this thesis (through this thesis, NVC presents the negatively-charged nitrogen vacancy center in diamond). The electronic structure of the NVC is formed of six electrons; two electrons provided by the nitrogen atom, three electrons provided by the dangling bonds from the three carbon atoms surrounding the vacancy point, and one electron which is captured from the lattice [20].

NVC is of fundamental importance in the content of the present thesis. Therefore, in the rest of this chapter, a brief review about its properties will be given.

1.2.1. Basic optical and spin properties

The basic photophysics of an NVC can be described by assuming three electronic levels (see Figure 1.3-(a)); a ground state $|\mathrm{g}\rangle$, an excited state $|\mathrm{e}\rangle$ (with the radiative lifetime of $\approx$ 12 ns) and a metastable singlet state $|\mathrm{m}\rangle$ (with the lifetime of $\approx$ 250 ns) [20] (more details can be found in chapter 3). The ground and excited states are spin triplet states (S=1) which are further split into three spin sublevels, $m_s = 0$ and $m_s = \pm 1$. The $m_s = 0$ sublevel is energetically lower than the $m_s = \pm\ 1$ sublevels, and the $m_s = \pm 1$ sublevels are degenerate. The energy difference between the $m_s = 0$ and $m_s = \pm 1$ sublevels is given by the zero-field splitting D, given by $D = 2.87$ GHz and $D = 1.42$ GHz for the $|\mathrm{g}\rangle$ and $|\mathrm{e}\rangle$, respectively.

The NVC can be non-resonantly excited into the vibronic levels of the $|\mathrm{e}\rangle$ using a laser with wavelength of 532 nm. Then, the NVC decays from the $|\mathrm{e}\rangle$ either directly to the $m_s = 0$ of

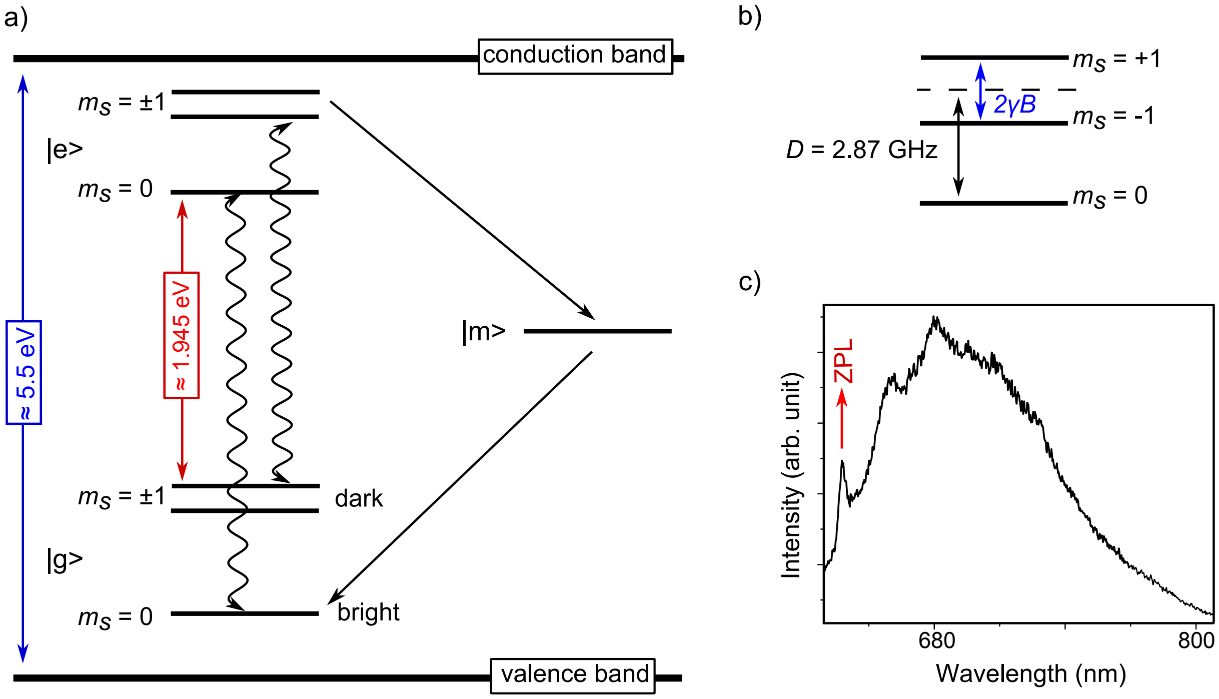
a)
conduction band
m_S = ±1
|e>
m_S = 0
≈ 5.5 eV
≈ 1.945 eV
|m>
m_S = ±1
dark
|g>
m_S = 0
bright
valence band
b)
m_S = +1
2γB
m_S = -1
D = 2.87 GHz
m_S = 0
c)
ZPL
Intensity (arb. unit)
680
800
Wavelength (nm)

Figure 1.3.: Energy structure diagram of an NVC in diamond in room temperature is depicted. a) The energy levels of NVC are located within the band gap of diamond. Ground state ($|g\rangle$), excited state ($|e\rangle$), and metastable singlet state ($|m\rangle$) form the energy scheme of an NVC. The allowed transitions between these states are depicted. The wavy arrows show the radiative transitions (which are also spin-preserving) where the straight solid arrows present the non-radiative ones. Figure is adapted from [20]. b) The $|g\rangle$ of an NVC is focused, noting the zero-field splitting term (D) and the magnetic Zeeman interaction. c) An emission spectrum of an NVC under pumping wavelength of 532 nm is demonstrated, showing the ZPL and broad phonon sideband.

the $|\mathrm{g}\rangle$, or by passing through the $|\mathrm{m}\rangle$ due to intersystem crossing. Only few percent of these emitted photons are spectrally located at the wavelength of $\approx$ 637 nm (zero-phonon line: ZPL, equivalent to 1.945 eV) where other photons stand in vibrational side bands (phonon sideband) in the spectral range of $\approx$ 650 nm to 800 nm (see Figure 1.3-(c)).

The level structure of the excited state of the NVC is well explored at room [22] and low temperature [23]. However, most of its applications are based on its ground state properties. The degeneracy between m_s = +1 and m_s = -1 sublevels can be lifted by magnetic fields based on Zeeman interaction (see Figure 1.3-(b)) with gyromagnetic ratio of γ = 2.8 MHz/G [20]. This is the key background of all the magnetic field sensing experiments based on NVCs. The metastable state $|\mathrm{m}\rangle$ plays a vital role in the optical readout of the NVCs. Due to different transitions shown in Figure 1.3-(a), an electron in the m_s = $\pm$ 1 of the $|\mathrm{e}\rangle$ decays with significant probability to the $|\mathrm{m}\rangle$ while the m_s = 0 of the $|\mathrm{e}\rangle$ decays directly to the m_s = 0 of the $|\mathrm{g}\rangle$. These two different transitions lead to an optical contrast of $\approx$ 30 % between the m_s = 0 and m_s = $\pm$ 1 of the ground state. This spin-dependent luminescence is a main tool which enables optical readout of the spin states of NVCs. To perform spectroscopy and individually address different levels of the $|\mathrm{g}\rangle$, an auxiliary microwave field is applied to the NVC. As the microwave frequency is tuned to be resonant with the relevant transition (m_s = 0 to m_s = $\pm$1), the associated excitation occurs which results in a reduction of the detected fluorescence intensity. This technique is called optically-detected magnetic resonance (ODMR) (demonstrated in 1997 [21]) which enables further ESR measurements utilizing NVCs. ODMR measurements will be used frequently in the experiments shown in chapters 3 and 4. An example of the ODMR spectrum of a single NVC under $\approx$ 64 G of magnetic field applied to its symmetry axis is shown in Figure 1.4-(a).

The electronic spin of the NVC is coupled to the nearby nuclear spins, e.g. the nitrogen and carbon nuclear spins, via the hyperfine interaction. By applying the ODMR technique, this information about the nearby nuclear spins can be also deduced. For example, the ODMR spectrum presenting two dips distanced by 3 MHz is depicted in Figure 1.4-(b), which proves the coupling to the nearby ^{15}N nuclear spin.

The m_s = 0 and m_s = $\pm$1 spin sublevels of an NVC form a two-level quantum mechanical system (qubit), on which the Bloch sphere concept and hence the coherence-related measurements can be carried out. For instance, the Rabi oscillations between the ground-state m_s = 0 and m_s = -1 sublevels is shown in Figure 1.4-(c), revealing Rabi period (π) of $\approx$ 100 ns. Given the transition frequency and the corresponding Rabi period, several pulsed measurements employing different pulse sequences can be used to assess the NVC coherence properties. For instance, a Hahn echo pulse sequence (see Figure 1.4-(d)) can be used to measure the spin-spin relaxation time (T_2) of NVCs. Hahn echo decay signals for two NVCs with different depths are presented in Figure 1.4-(e) to -(f) [24]. As can be seen in these figures, different mag-

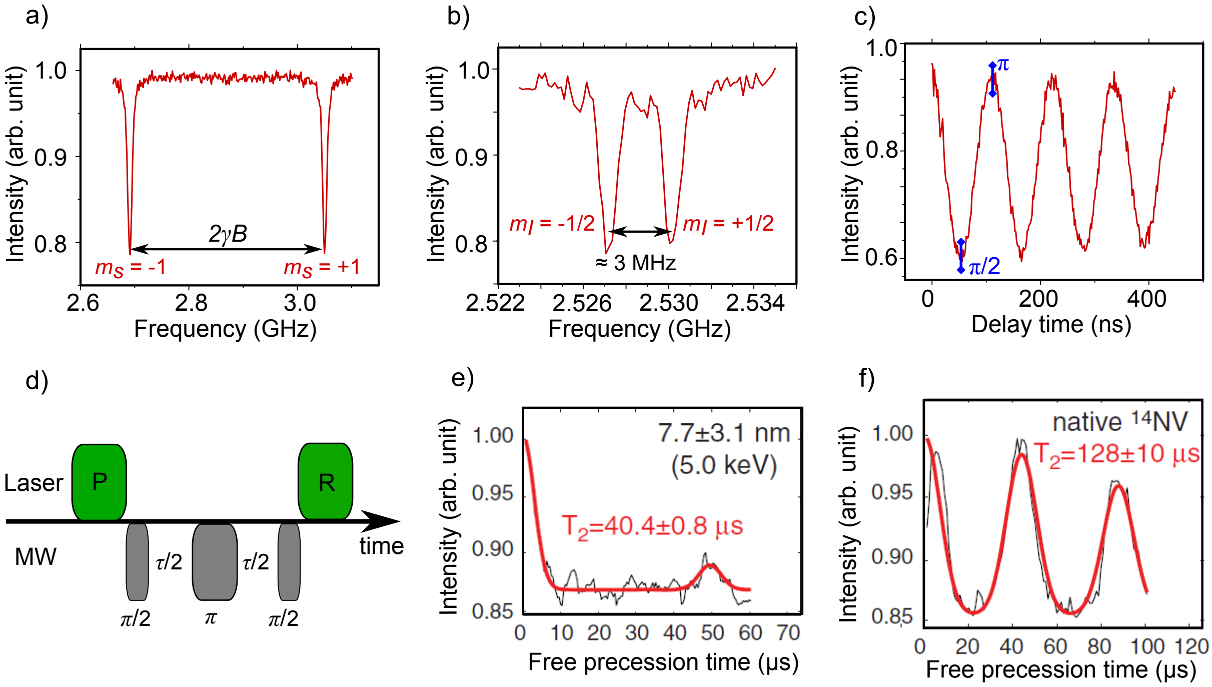

Figure 1.4.: a) ODMR measurement revealing the $m_s = \pm 1$ spin sublevels is shown. As can be seen, with respect to the Zeeman interaction, the ODMR technique can also give information about the magnetic field applied to the NVC. b) By applying ODMR technique, the present nearby ^{15}N nuclear spin coupled to the electron spin of the NVC can be detected. c) The ground-state spin sublevels of the NVC form a quantum mechanical two-level system for which, by applying the resonant MW pulses, the Rabi period can be measured to be $\approx$ 100 ns. d) The frequently-used Hahn echo scheme to measure the T_2 coherence times of NVCs is shown. Initially the NVC is pumped (P) into its $m_s = 0$ state. Then $\pi/2$-$\tau/2$-π-$\tau/2$-π sequence consisting of resonant MW pulses and delay times is applied to the NVC. Finally the readout (R) of the spin state of the NVC is performed. This process is repeated for multiple times to achieve sufficient signal-to-noise ratio. The Hahn echo decay signal for NVCs with different depths are shown in Figure 1.4-(e) to -(f). The decay behavior can be either Gaussian which is imposed by the slowly fluctuating ^{13}C nuclear spin environment, or be exponential which is set by rapidly fluctuating surface impurities. Figures (e) - (f) are taken from [24].

netic noises at the NVC location can yield in different decay shapes in the Hahn echo signal, causing in different T_2 values [24].

1.2.2. Creation techniques

It is unavoidable to synthesize a diamond substrate in which no NVC exists. Although these natural NVCs can be sufficient for some applications, mostly doping with more controlled NVCs is required. This control means, to have much higher concentration of NVCs in predefined lateral position and depth. The mostly-used generation technique of the NVCs in a bulk diamond substrate is a combination of ion implantation and annealing techniques. In this way, high concentration of nitrogen (ions or molecules) is introduced to the substrate, which consequently produces vacancies in the diamond lattice. Afterward, annealing the sample at temperatures of $\approx 1000^\circ$ C promotes diffusion of these vacancies which finally yields in formation of NVCs. The yield factor, i.e. the ratio of the generated NVCs per initial implanted nitrogen concentration, depends on the energy of the implantation [20]. Electron radiation or helium irradiation of diamond substrates with considerable amount of nitrogen concentration are alternative methods to generate NVCs [20, 25, 26].

1.2.3. Photon collection efficiency

Diamond has a relatively high refractive index in visible spectral optical range (see Eq. 1.1). This encourages the application of diamond in macro- to nanoscale photonic devices [11]. However, this imposes an obstacle on the collection efficiency of the photons emitted by the NVCs, even by using the best optical collection tools e.g. microscope objectives with very high numerical aperture [11]. With respect to the big mismatch in the refractive index of diamond ($n_d \approx 2.4$) and the collection medium (e.g. air, $n_a \approx 1$), most of the photons emitted by the NVC cannot pass through the diamond-air interface and reflect back to the diamond substrate. Only a small fraction of these photons which are within a certain angle with respect to the normal to the diamond substrate, can pass through this interface and get partially collected by the collection tools. This angle is defined as the critical angle ($\theta_c = 1/n_d \approx 24^\circ$) and this phenomenon is known as total internal reflection (TIR) (see Figure 1.5-(a)) [18]. Accordingly, via a confocal assembly, approximately 10^5 photons/sec can be collected from a single NVC located in a bulk diamond substrate at room temperature [28]. This value plays an important role in application of NVCs, since the readout process of the spin states of NVCs is optically performed. Several attempts have been reported to tackle the poor collection efficiency of the NVCs, which can be categorized into two main monolithic and non-monolithic groups.

Among the monolithic solutions, one can point to diamond solid immersion lens (SIL)

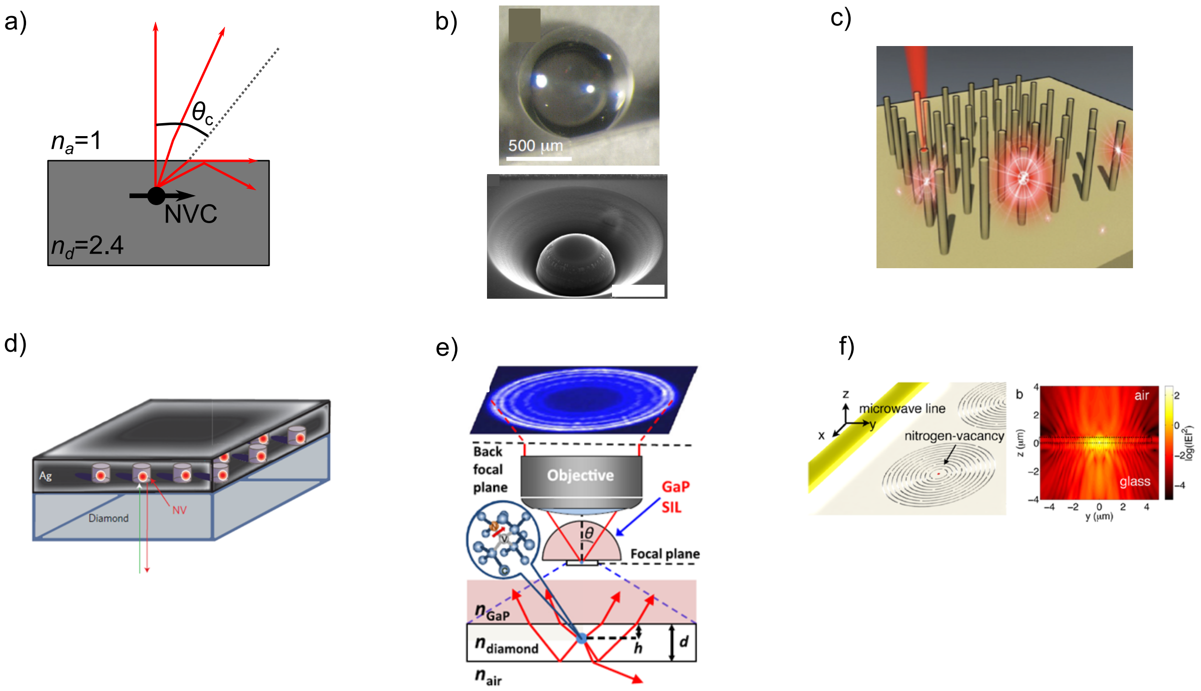
a)
θ_c
n_a=1
NVC
n_d=2.4
b)
500 µm
c)
d)
Ag
NV
Diamond
e)
Back focal plane
Objective
GaP SIL
θ
Focal plane
n_{GaP}
$n_{diamond}$
h
d
n_{air}
f)
z
x
y
microwave line
nitrogen-vacancy
b
air
glass
z (µm)
y (µm)
log(|E|²)

Figure 1.5.: a) Total internal reflection (TIR) process with the critical angle (θ_c) is shown as an obstacle imposing poor collection efficiency of NVCs. b) Macro- and microscale diamond solid immersion lenses (SILs) are developed to increase the photon collection efficiency of bulk NVCs. Figures are taken from [27, 28]. The scale bar in the lower figure presents 10 μm. c) Nanopillars are waveguides which are fabricated directly onto the diamond substrate to increase the number of collected photons from shallow and bulk NVCs. Figure is taken from [29]. Besides the monolithic solutions to the enhancement of photon collection efficiency of NVCs, non-monolithic solutions are also developed, as shown in d), e) and f). In d) silver layer is employed to apply Purcell enhancement to the photon count rate of NVCs integrated in the nanopillars. Figure is taken from [30]. e) Another approach can be utilization of a GaP lens which guides the photons emitted by the NVC to the objective lens. Figure is taken from [31]. f) By means of bullseye diamond structure which is mounted on top of a glass substrate, more than one order of magnitude enhancement is obtained in the photon collection efficiency of NVCs. Figure is taken from [32].

[27, 33, 28] (see Figure 1.5-(b)) and nanopillars [34, 35, 29] (see Figure 1.5-(c)). Diamond SILs are either individually machined macrolenses ($\sim$ 1 mm) from diamond including NVCs [27], or integrated microlenses ($\sim$ 10 μm) which are directly fabricated into the diamond substrate surrounding a predefined NVC [33, 28]. By providing a hemisphere geometry around the targeted NVC, SILs are reported to avoid the TIR effect and hence increase the photon collection efficiency of bulk NVCs by $\sim$ 5 times. To increase the photon collection efficiency of bulk [34, 29] and especially shallow NVCs [36], diamond nanopillars are developed. The emitted photons of the embedded NVCs can couple to the waveguide modes of these nanopillars and efficiently get collected by the collection tools. These nanopillars (diameter $\approx$ 200 nm, height $\sim$ 1-2 μm), which are fabricated directly onto the diamond substrate, can increase the photon collection efficiency of the host NVCs up to $\approx$ 10 times.

In other set of approaches to increase the photon collection efficiency of NVCs, application of other material is pointed. For instance, by providing silver layer surrounding the nanopillars, the electric environment of the NVC is manipulated, which yields in shorter excited-state lifetime and hence Purcell-enhanced increase in the number of collected photons of the NVCs [30] (see Figure 1.5-(d)). In another approach, a dielectric antenna i.e. a GaP lens is engineered for individual NVCs [31]. Benefiting from its higher refractive index in comparison to that of diamond ($n_{\mathrm{GaP}} \approx 3.3$) and accordingly larger θ_c, more photons are directed to the collection tools ($\approx$ 10 times). As another non-monolithic approach to augment the photon collection efficiency of the NVCs, diamond bullseye grating are developed which redistribute the emitted photons by the NVC into low-NA channel toward the microscope objective [32] (see Figure 1.5-(f)). Additionally, the electric environment of the NVCs is manipulated by positioning these structures on top of a glass substrate. By these two solutions, more than one order of magnitude enhancement is achieved.

1.2.4. Applications

A combination of notable spin and optical properties put NVCs in diamond ahead of the other competitor solid-state single photon source spin defects, such as SiVC [37] and rare-earth defects [38]. NVCs have been shown to be employed in several directions of the research activities in the last decade. Among them, fundamental quantum mechanical observations like entanglement [39] and quantum error correction [40] to experiments towards long-distance quantum communication [41] can be listed. Besides the mentioned applications, NVC has been shown as a versatile nanoscale quantum sensor for various physical quantities such as magnetic field [42], electric field [43], temperature [44], strain [45], etc [20]. In following, these sensing applications will be shortly reviewed.

Generally, all of the applications of NVC as a quantum nanoscale sensor are stemmed from the capability of high-fidelity initialization, manipulation, and optical readout of the spin levels of NVC. Additionally, sensitivity (interaction) of NVC electronic spin levels to (with) different physical quantities form the sensing basis of NVCs. These physical parameters play a role as perturbations to the spin energy levels of NVCs, which can be understood via the following Hamiltonian of NVC ($\hbar$ is assumed as 1) [20]:

$$H_{\mathrm{NVC}} = \underbrace{D\left(S_z^2 - \frac{2}{3}\right)}_{\text{ZFS}} + \underbrace{\gamma \mathbf{B}\cdot\mathbf{S}}_{\text{magnetic (Zeeman)}} \underbrace{+\varepsilon_z E_z\left(S_z^2 - \frac{2}{3}\right) + \varepsilon_{xy}\left\{E_x\left(S_x S_y + S_y S_x\right) + E_y\left(S_x^2 + S_x^2\right)\right\}}_{\text{electric}}, \tag{1.2}$$

where $\mathbf{B}$ and $\mathbf{E}$ are the magnetic and electric fields at the location of the NVC, respectively, $\mathbf{S}$ is the spin operator, and ε_z and ε_{xy} are the electric field coupling constants. Here, the z axis is the symmetry axis of the NVC ((111) diamond crystal axis). For moderate magnetic and electric fields, the zero-field splitting term is dominant (shown with ZFS) and the magnetic and electric fields act as perturbations. The zero-field splitting constant itself is dependent upon temperature and pressure [20], which provides NVCs with the capability of being used as temperature and pressure sensors. As can be seen, external magnetic field lifts the degeneracy of spin levels, whereas the electric field can either shift these spin levels or mix them [20, 45]. Based on the given coupling constants, it is deduced that the magnetic coupling is far stronger than the electric one. Commonly, to precisely measure these perturbations, direct CW ESR measurements, pulsed (time-evolution) measurements, and relaxometry measurements are performed so far [20]. The sensitivity of the magnetic field sensing is limited by the optical and spin properties of the NVC probe i.e. its photon flux and coherence times, as well as the required measurement time [20]. In this way, the corresponding shot-noise-limited magnetic field sensitivity (minimum detectable magnetic field within 1 s of acquisition time) δB_{min} is scaled with $\frac{1}{\sqrt{NT_C F}}$ where N is number of NVC probes and T_C is the coherence time of them. Additionally, F is the number of collected photons emitted by a single NVC per one measurement shot [46, 47]. Given the corresponding values for a single NVC, the magnetic field sensitivity of few nT/$\sqrt{\text{Hz}}$ is achieved [20].

Optimizing the magnetic field sensitivity as well as sensing the residual and applied stress is at the core of this thesis, which will be explored in more details in chapters 3 and 4, respectively.

2. Diamond Micro- and Nanofabrication Techniques

The demonstrated fabrication recipes in this chapter are partially employed in [25], F. Fávaro de Oliveira, S. Ali Momenzadeh *et al.* Appl. Phys. Lett. **107**, 073107 (2015) and [48], Ingmar Jakobi, S. Ali Momenzadeh *et al.* Journal of Physics: Conference Series, **752**, 012001, (2016).

Micro- and nanostructuring techniques are continually advancing to enable the fabrication of more complicated objects on smaller scales within a shorter time and with higher resolution. Achievements of those techniques are not only limited to laboratory-based micro- and nanoscale objects in electronics, mechanics, medicine, etc, however importantly is extended to daily routine human life. Among other fields, the mentioned techniques could show their magnificence also in basic research within the recent decades, as they could enable platforms on which many important classical and quantum physical concepts could be investigated, verified, and afterward transferred to application arena.

Similarly, state of the art fabrication techniques have been employed in diamond NVC research field which facilitated the development of e.g. nanophotonic and nanomechanical devices manifesting inestimable advancements. Besides different thin-film deposition techniques, various patterning methods such as electron-beam lithography (will be also mentioned afterward as EBL or e-beam lithography) [49], dry plasma etching [34, 50], and focused ion beam (FIB) milling [33, 28] are reported to fabricate several devices based on diamond and embedded NVCs.

This approach, i.e. development of fabrication procedures to create novel hybrid quantum diamond structures, is at the heart of this PhD thesis. In contrast to frequently-used materials in semiconductor technology such as silicon, fabrication of diamond is challenging. For instance, the well-known wet chemical etching methods are not functional for diamond [1].

Consequently, the known fabrication procedures and recipes are relatively limited. Therefore, several specific fabrication procedures have to be developed throughout this thesis to enable the realization of the targeted hybrid platforms. Each of these fabrication procedures are arranged as a sequence of conventional fabrication steps which are developed to be compatible with diamond. In addition to their functionality, these steps and the whole procedure are compelled to be harmless to the embedded NVCs; equivalently it means that these steps must not entail any degradation into the optical and spin properties of NVCs.

In this thesis, the starting diamond substrates are generally thin diamond films (thickness $\sim$ 30 μm) which are produced under a collaboration with external companies. These diamond thin films are shortly introduced, in prior to presenting the developed fabrication techniques. Then, lithography-based patterning for fabricating the NVC-diamond hybrid devices is focused on. In this way, e-beam lithography and reactive ion etching - inductively-coupled plasma (RIE-ICP) methods will be explained. Thereupon, a brief introduction about these techniques will be given which will be followed by an explanation of the developed fabrication recipes. For each technique, some devices will be demonstrated as the associated outputs.

2.1. Diamond thin films

In this thesis, only top-down fabrication approach is applied. Practically, given the diamond substrate, only further patterning steps are pursued on it, while no diamond overgrowth, etc, is performed. The initial diamond substrates are generally type-IIa (refer to chapter 1 about different types of diamond) ultrapure CVD (100)-oriented diamonds with ^{13}C natural abundance provided by Element Six, with lateral dimensions of few millimeter and thickness of approximately half a millimeter. These substrates are hereinafter called "bulk". The bulk substrates should be however thinned down further to be proper starting materials for the desired hybrid photonic and mechanical architectures (see chapters 3 and 4, respectively). Therefore, these substrates are thinned down to microscale thicknesses by Delaware Diamond Knives, Inc. (DDK) by means of laser cutting and mechanical polishing methods. As shown in Figure 2.1, the bulk substrate is first bisected through its thickness. Each of these divided parts are of the thickness of $\sim$ 100 μm, which show very rough cutting-induced features (can be up to $\sim$ 10 μm or even higher). Then, to smoothen the rough surface, they are polished by means of mechanical tools down to a thicknesses of $\sim$ 30 μm. This polishing step is of crucial importance for the sake of thin films' suitability regarding their applications. To be more clear, the surface roughness of the diamond film highly influences the optical and especially the spin properties of shallow NVCs, as well as performance of the diamond structure itself. The achieved averaged RMS surface roughness of these films is monitored by AFM to be $\leq$ 3 nm

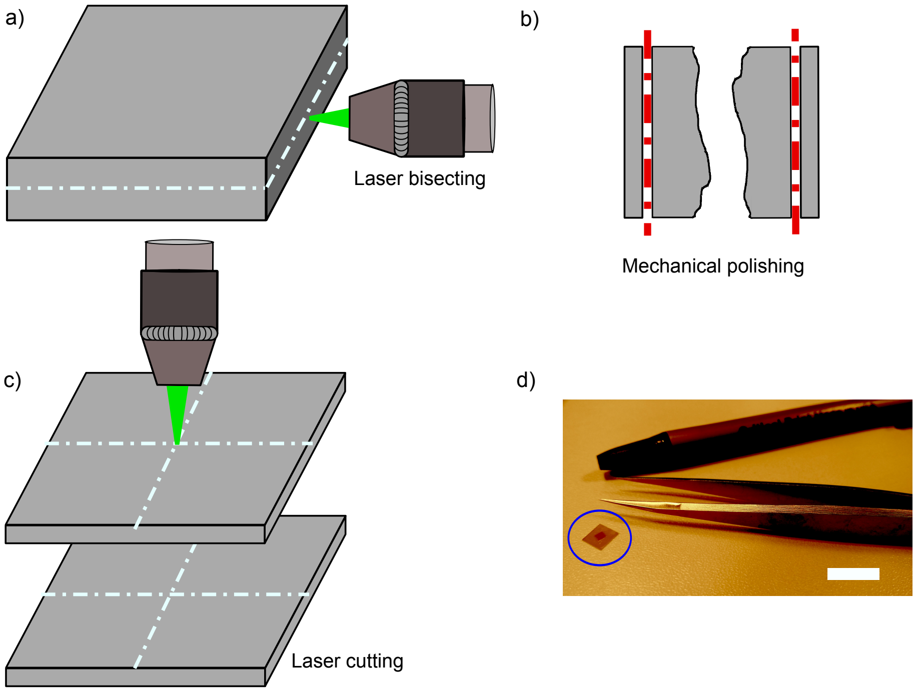

Figure 2.1.: Fabrication scheme of the diamond thin films from the starting bulk diamond substrate is depicted. (a) The bulk substrate is first bisected by means of high power laser beam (e.g. along the white lines). b) Then, to remove the cutting-induced rough surface and also approach the desired thickness, they are thinned down and polished by means of mechanical tools (e.g. along the red lines). This step is a time-consuming process which is of crucial importance for the suitability of the output films in their applications. (c) Afterward, to provide more diamond films, they are transversely cut into few more pieces, usually with the dimensions of ~ 2 mm $\times$ 2 mm $\times$ 30 μm (e.g. along the white lines). (d) As an illustrative presentation of the final thin diamond films, one of them, which is glued on top of a type-I diamond (marked with a blue circle), is shown. Scale bar shows 2 cm.

over scanning range of $\sim 10\ \mu$m $\times$ $10\ \mu$m. To be provided with more diamond films from an initial bulk substrate, they are afterward cut transversely into several pieces. The final diamond films usually have dimensions of ~ 2 mm $\times$ 2 mm $\times$ 30 μm. To provide structural support, if not conflicting with the fabrication steps, they are attached onto either diamond or silicon substrates. As depicted in Figure 2.1-(d), a diamond thin film with the above-mentioned dimension is glued on top of a type-I diamond substrate (see chapter 1 for different types of diamond) with lateral dimensions of ~ 1 cm. Still, a great care with handling is required due to their small dimensions. In Figure 2.1-(d) their relatively small size in comparison to the cleanroom tweezers is highlighted.

2.2. Electron beam lithography

Lithography techniques based on optical beam (UV, photolithography) or electron beam (e-beam lithography) have found their important roles in semiconductor technology for decades [51]. While the resolution of the photolithographically-shaped patterns are limited to ~ 100 nm due to the wavelength of the exposure light, e-beam lithography can result in structures with sub-10 nm resolution [51, 52]. By means of focused electron beam generated from high voltage sources (~ 10 kV), e-beam lithography is capable of forming arbitrary 2D patterns on a large scale. The perdurable part of the e-beam lithography is the electron resist (they are in liquid form which should be spin-coated on the substrate.). By exposure to the e-beam, they get ionized and consequently undergo some physical/chemical changes. With respect to the output of the further interaction with developer solution, they are either called positive, or negative tone e-beam resists. By immersing the electron-exposed positive (negative) resist into the developer solution, the exposed (nonexposed) fragments are dissolved from (formed on) the substrate, while the others remain to the substrate (dissolve in the developer solution). In this thesis, e-beam lithography has been exploited to form the e-beam resist mainly for two purposes: i) to serve as a mask for nitrogen implantation to generate predefined arrays of NVCs and ii) to produce the mask for the subsequent etching step. In this thesis PMMA (poly-methyl methacrylate) as a positive resist is used for both purposes, while FOX 25 (also known as HSQ (hydrogen silsesquioxane)) as a negative tone resist is only utilized for the latter purpose. To provide the reader with the prerequisite background, first, preparation of PMMA implantation mask will be presented. Then, plasma etching technique will be briefly reviewed, which will be followed by demonstration of some exemplary diamond nanostructures developed by means of the two above-mentioned methods.

2.2.1. Creation of NVC arrays via PMMA nano-apertures

Engineering and spatially controlling the NVCs in diamond holds a core importance towards their potential applications in quantum information processing, as well as quantum sensing [20, 49]. To that aim, e-beam lithography was presented as a tool to spatially control the position of the implanted nitrogen ions via nanofabricated apertures in electron resist, thus to form a predefined array of NVCs [49]. By preselecting the implantation dose with respect to the aperture size (sub 100 nm), single NVCs were formed with $\sim 30\%$ probability [49]. Similar NVC arrays were used as a platform to perform ultrasensitive temperature measurements (10.1 mK/$\sqrt{\mathrm{Hz}}$) [53].

Here, chip-scale production of coupled NVCs, i.e. $\geq$2 NVCs per aperture, is targeted. In the case of two NVCs separated by distance r, they interact via their magnetic moments with the associated short-range dipolar coupling strength scaled as $\frac{1}{r^3}$ [39, 48]. This coupling can be effective, if it acts within a timescale shorter than the coherence time of the NVCs. In order to enable a quantum register based on coupled NVCs, the coupling strength between them should be larger than each of their decoherence rates ($\frac{1}{T_2}$), thus enabling quantum information exchange between them. It denotes not only the crucial role of their distance, however their coherence times as well. To avoid truncation of the implanted NVCs' coherence times by magnetic or electric noises at the diamond surface [25, 26, 48], higher implantation energy of the nitrogen ions is favorable. An obstacle nevertheless raises here. The higher the energy of the ion implantation into the diamond lattice is, the higher is their scattering in the lattice ("straggling"). For instance, nitrogen ions with energy of 10 keV yield in mean scattering of $\approx$ 20 nm [48]. It shows that beyond a certain limit, shrinking the diameter of the implantation aperture is not favorable, since the straggling effect is mostly dominant. By performing simulations on the effect of different implantation parameters on the final coupling strength of two NVCs, implantation energy of 30 keV within the aperture size of 50 nm is revealed to be an optimized compromise [48].

To realize large-scale arrays of NVCs, a [100]-oriented diamond bulk substrate with ^{13}C natural abundance is chosen as the starting host platform. A PMMA layer of approximately 400 nm thickness is spin coated on top of the substrate. This thickness is chosen to guarantee the sufficient masking of PMMA layer against the implanted nitrogen ions. Then, the sample/resist is baked at 160° C for 4 minutes to get rid of the solvents of the resist solution. To avoid the charging effect during the e-beam lithography process [51], a 5 nm Cr layer is thermally evaporated on top of the PMMA resist. Then, e-beam lithography process with 30 kV and 10 μm as the acceleration voltage and aperture size, respectively (current $\sim$ 40 pA), is exploited to expose $\sim$ 5000 sites with the matrix distance of 4 μm in a form of several grids per sample. After this process, the anti-charging Cr layer is removed in Cr-etchant solution,

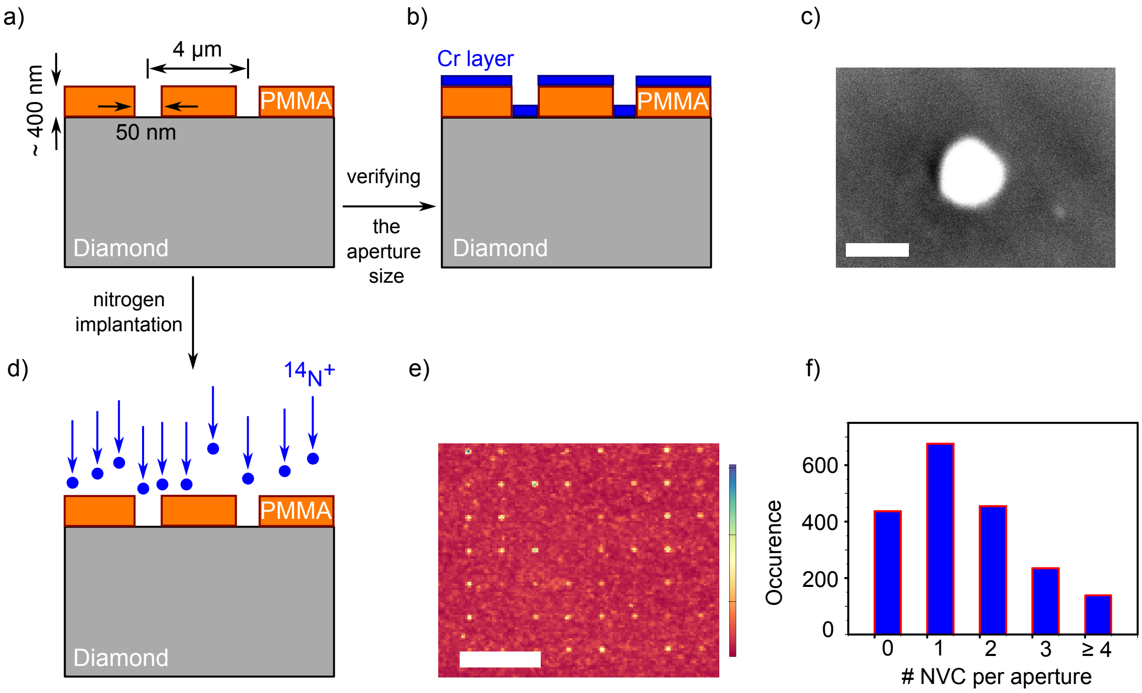
a)
4 µm
~ 400 nm
50 nm
PMMA
Diamond
b)
Cr layer
PMMA
Diamond
verifying the aperture size
c)
nitrogen implantation
d)
$^{14}N^+$
PMMA
Diamond
e)
f)
Occurence
600
400
200
0
0
1
2
3
≥ 4
# NVC per aperture

Figure 2.2.: Fabrication and characterization of the NVC array arrangement is demonstrated. (a) As the first step, $\sim$ 1000 apertures with the diameter of $\approx$ 50 nm are formed in $\approx$ 400 nm-thick PMMA with the matrix distance of 4 μm on top of a diamond substrate. (b) Then, 30 nm of chromium (Cr) is deposited by means of high vacuum thermal deposition technique on top of the whole mask. Next, the lift-off process is performed, which leaves finally only the deposited Cr layer within the PMMA apertures. This way is utilized to verify the PMMA aperture size. (c) An SEM image of one of these Cr points reveals a diameter of $\approx$ 52 nm. Scale bar shows 50 nm. (d) After verifying the right aperture size, step (a) is repeated again. Then, nitrogen ions are implanted through the PMMA apertures into the diamond lattice to generate NVCs. (e) An exemplary confocal image of the developed NVC array system is depicted. Scale bar shows 10 μm. (f) Statistics on the formation of NVCs within 1941 developed PMMA apertures is shown. As can be seen, $\sim$ 20% of the apertures possess double NVCs. The statistics is assessed based on the fluorescence intensity acquired from each spot.

followed by developing the PMMA resist in MIBK:IPA (1:3) solution for about 2 minutes (see Figure 2.2-(a)). To know the right aperture size, the electron exposure dose is varied among several grids. To verify the right dose and hence the correct aperture size, 30 nm of Cr is thermally evaporated on top of the sample area, pursued by lift-off process. This process is performed by immersing the sample about 1 hour inside NEP solution at the temperature of 65° C. The prepared Cr sites are then probed in scanning electron microscope (SEM) apparatus. As shown in Figure 2.2-(c), for electron exposure dose of $\sim 400\ \mu\mathrm{C/cm}^2$, aperture size with the diameter of ≈ 50 nm is achieved. Given the right parameters of the e-beam lithography process, the PMMA mask fabrication is again repeated on the same (clean) sample. Nitrogen ions ($^{14}\mathrm{N}^{+}$) of the energy and fluence of 30 keV and 10^4 ions/μm^2, respectively, are implanted into the diamond lattice through the lithographically-written PMMA apertures (see Figure 2.2-(d)). As the next step, the PMMA layer is removed, and the diamond substrate is annealed at $\approx 900°$ C under 10^{-7} mbar vacuum condition. Consequently, it is boiled in triacid mixture (H_2SO_4:HNO_3:$HClO_4$, 1:1:1) for almost 2 hours. This process removes the amorphous carbon layer at the surface of diamond, in addition to provide oxygen termination of the diamond surface.

To characterize the final NVC arrays, the sample is inspected by a home-built confocal microscope under ambient conditions. Figure 2.2-(e) shows an exemplary confocal scan of implanted NVC sites through the PMMA nano-apertures. To obtain the amount of NVCs per nano-aperture, ≈ 1900 spots are assessed based on their fluorescence intensity in comparison to that of a single NVC. It is found that the achieved statistics follows a Poissonian behavior with an average of 1.6 NVC per nano-aperture. In a similar way, the success rate to result in one and two NVC(s) per nano-aperture is derived to be 30 % and 20 %, respectively (see Figure 2.2-(f)). This statistics proves an efficient match between the simulation and experimental results to produce large-scale arrays of NVC registers.

To investigate the utilized method to form strongly-coupled NVC pair arrays, all of the bright sites showing a fluorescence signal at least twice of a single NVC's are marked. Further filtering on these sites is performed by measuring the T_2 coherence time of the NVCs. Therefore, implantation sites with NVCs possessing coherence times shorter than 20 μs are omitted from the study. By applying double electron-electron resonance (DEER) measurement, several strongly-coupled NVCs are recorded. The maximum coupling strength is monitored to be ≈ 3.9 MHz which yields in the distance of ≈ 3 nm between two NVCs. Consequently, the overall success rate of 0.1% in the formation of strongly-coupled NVC pairs is achieved, which is expected to be slightly trimmed by limitations of the measurements [48].

2.2.2. Patterning flowable oxide (FOX 25)

Leading application of e-beam lithography technique to produce the suitable etching mask towards developing high quality diamond structures is previously mentioned. Besides PMMA, another often-used electron resist in the course of this thesis is hydrogen silsesquioxane (HSQ) commercially named as FOX 25. It is available as the polymer solution in MIBK. With respect to its properties and also its behavior after developing in etching applications, it is known as a prominent alternative to silicon dioxide [54]. It can be exposed by electron beams as well as extreme UV, i.e. wavelengths below $\sim$ 150 nm [54] featuring negative tone resist characteristic. It is a well-documented electron resist in semiconductor technology essentially due to its unrivaled sub- 20 nm resolution [54] and high etch selectivity against oxygen plasma. The latter will be explained in more details in this chapter as well as next chapter.

The general way to process FOX on diamond substrate is as follows. As the first step, the resist solution should be spin-coated on top of the diamond substrate. Common to all of its applications in this thesis, 6000 rpm for 45 seconds is applied. Second, it is baked on a hotplate at temperature of 90° C for 1 minute. For electron exposure, in the course of this thesis, acceleration voltages of 20-30 kV are used. In contrast to PMMA, the required electron dose is highly dependent upon the structure size. For instance, nanostructures with the dimensions of $\sim$ 100 nm could be sufficiently exposed by electron dosage of $\sim$ 1000 μC/cm^2, whereas the structures as large as few microns can be sufficiently exposed by the electron dosage of $\sim$ 50 μC/cm^2. To develop the exposed pattern, the FOX/diamond chip is immersed in light solution of TMAH, commercially available as MF-322, for about 8 minutes. Via the above-mentioned recipe, FOX 25 layer with the thickness of $\sim$ 400-500 nm can be formed on top of the diamond surface. Of crucial threat to the functionality of FOX resist in diamond structuring applications, is its adhesion to the diamond surface. It is seen that for electrons induced from acceleration voltages up to 30 kV, no adhesion of FOX layer to the diamond surface can be achieved. To circumvent this problem, mostly, 5 nm of thermally-evaporated Cr as the adhesion layer is used. To remove the patterned FOX geometry, hydrofluoric acid (HF) or equivalently fluorine-containing plasma recipe (e.g. CF_4 or SF_6) are mostly used.

While FOX patterns can also be used as active photonic structures [51], here, their applications as etching mask are exclusively focused upon. To clarify the utilized etching procedures involving FOX 25 electron resist within the course of this thesis, in the coming section, the plasma etching procedure will be explained in more details.

2.3. Reactive Ion Etching - Inductively-Coupled Plasma (RIE-ICP)

The use of plasma-based technologies alongside e-beam lithography is the central part of nanomachining in semiconductor technology [55]. While plasma has widespread applications such as sputtering and deposition, dry plasma etching technique holds its unique role in micro- and nanofabrication methods. In this regard, the main reason is its high controllability and hence its precision, compatibility with automatized industry, ability of anisotropic etching, and accurate transfer of the mask pattern to the substrate, even at nanoscale [55, 56, 57]. For some materials like diamond, these capabilities are even more significant since wet etching of diamond substrates is almost impossible. In recent years, several plasma recipes have been demonstrated to structure diamond architectures [58, 59]. Similarly, this technique has been an inevitable part of this thesis. Therefore, general principles of plasma etching will be reviewed in the following. Afterward, several developed etching recipes through the course of this work will be shown. It should be mentioned that plasma etching procedure as an important tool in realization of photonic and mechanical diamond-NVC hybrid structures will be however explicitly demonstrated in chapters 3 and 4, respectively.

2.3.1. General principles of plasma etching

The so-called fourth state of matter, plasma, is the coexistence of ions and electrons [55, 60]. Plasma is usually formed when a large RF voltage (frequency of 13.56 MHz) is applied to a pair of capacitively-coupled parallel plate electrodes in a certain low-pressure gas atmosphere inside a reactor chamber [55, 60]. In the plasma, free electrons collide with neutral species like the gas molecules. Often they undergo ionization and dissociation processes which results in 2 electrons and 1 ion. These electrons will further collide with the reactor walls and electrodes, and will be removed consequently from the chamber. Therefore, the plasma would be left positively charged. To guarantee the plasmas' charge neutrality, a DC electric field (voltage) is applied such that the electrons are repelled from the walls of the chamber. The targeted sample to etch is placed on one electrode which then will be exposed to the ions that are accelerated from the other electrode. The ionized reactive species close to the sample then react with its surface, which yields in volatile species that will be desorbed from the sample surface and finally pumped out from the chamber. This reactive etching at low pressures result in anisotropic etching profile due to much higher rate of vertical ions towards the sample surface in comparison to the horizontal ones. This method of etching is thus named reactive ion etching (RIE). An example of the involved chemistry of the reactive ion etching process

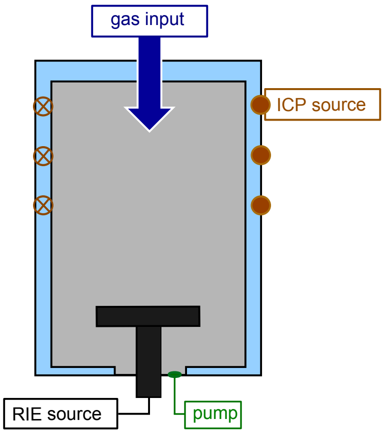

Figure 2.3.: Scheme of an RIE-ICP chamber is depicted. Gas molecules are introduced from top into the chamber. The substrate is positioned on top of the electrode connected to the RIE source. By interacting with the reactive species, the substrate is etched, then the volatile etch product gas will be pumped out from the chamber. In the case of RIE-ICP chambers, a separate power generator is exploited to control the magnetic field applied to the plasma through the coils surrounding the chamber (shown by brown symbols). This system gives high density of low-energy plasma with high uniformity, which yields in high etching rates associated with highly-anisotropic etching performance. Figure is adapted from [56].

of diamond can be explained therefore by using Ar/Cl_2 as the appropriate etching gas. During this process, Ar ions are utilized to sputter the diamond surface, which enables the chemical reaction of the chlorine ions with the carbon atoms of diamond in this way: $C + Cl_2 \rightarrow CCl_x$. The etch product CCl_x is volatile and will be pumped out and hence the final result is etching the diamond surface [58].

Given a specific substrate material and the corresponding etching gas, the amount of the etched material from the substrate surface per unit time is defined as the associated etching rate. To fabricate structures on a substrate, an etching mask is created on its surface prior to the etch process. It is desirable that the etching rate for the mask is significantly smaller compared with that of the substrate. The ratio between the two etching rates is defined as etch selectivity. [55, 60]. To achieve the best etching behavior in terms of etching rate and etch selectivity, the plasma parameters such as the RIE power, gas flow rate, pressure in the chamber, etc should be optimized. For instance, to achieve high aspect ratios of the designed geometry in the etched substrate, the ions should come in the most possible anisotropic way, i.e. at perpendicular angles to the substrate. To fulfill this, the chamber pressure must be reduced as much as possible, to reduce the secondary collisions of the ions. To that purpose, as well as for achieving higher etching rates, inductively-coupled plasma (ICP) can achieve a high quality and a high density plasma particularly at low pressures [56].

To realize the ICP arrangement, the RIE chamber is equipped further with a magnetic coil that is controlled by a separated power generator (see Figure 2.3). By applying an auxiliary magnetic field to the plasma, the density and uniformity of the plasma can be enhanced [56]. Consequently, higher etching rate and etch selectivity can be achieved, while higher quality of the etched area can be in parallel attained. Furthermore, separate control over the RIE and ICP systems offers individual control over the energy and density of the plasma accordingly [56]. In this work, RIE-ICP plasma apparatus has been intensively used as the primary plasma etching tool.

2.3.2. Applications of RIE-ICP process

In the following, several examples of RIE-ICP applications following the developed recipes will be mentioned. These applications can be divided into two main categories: (i) exploiting plasma to generate a high quality oxygen-terminated diamond surface without any etch-induced degradation of the spin and optical properties of NVCs. This developed procedure is even observed to enhance the coherence times of the shallow NVCs underneath. ii) To etch predefined structures in the diamond substrate. In this regard, high quality plasma procedures are developed and optimized to perform perpendicular and angled etching processes.

i) Controlled diamond etching with nanometric precision is demanding, especially towards further applications based on shallow NVCs. Importantly, plasma etching process should avoid any degrading effect on the spin and optical properties of shallow NVCs. To that aim, a two-step plasma procedure is developed which includes: 1) ignition of the plasma only with RIE power (no ICP) for few seconds which is continued by employing 2) only ICP (no RIE) process to perform the etching process. Step 1 is run with 10 mTorr of pressure and 30 W of RIE power using 30 sccm of oxygen flow rate. This step results in diamond etching rate ≈ 4 nm/min, revealed by AFM measurements. As soon as the plasma is ignited by means of the mentioned process, and it is sustained (which takes few seconds), the RIE source is shut down and the ICP source is activated. Step 2 is activated by setting 30 sccm of oxygen flow rate and 10 mTorr of chamber pressure, and by adjusting ICP power to 180 W. This process yields in ≈ 1.5 nm/min of diamond etching rate, measured by AFM. Hereby, this recipe is named as soft oxygen ICP process. By means of this plasma procedure no residual of amorphous RIE-damaged diamond layers could be indicated, monitored by AFM and X-ray photoelectron spectroscopy (XPS) measurements. Importantly, the XPS measurements additionally proves the full coverage of the diamond surface with oxygen species. By applying this technique to the NVC created by 5 keV of nitrogen implantation, no degradation of their fluorescence could be seen. However, importantly, an average threefold increase in the coherence times of the shallow NVCs could be registered. This enhancement is attributed to the modification of the electric configuration of the diamond surface, i.e. removal of the surface charges.

ii) In contrast to the previous application, in this category, higher etching rates resulting in a geometry as close as possible to the etching mask is desired. Another critical criterion to consider is however, the compatibility of the employed etching procedure with the embedded NVCs in the diamond substrate. In particular, the utilized etching procedure should not bring any degradation to the spin and optical properties of the remaining NVCs, notwithstanding the etching depth and the etched geometry. To fulfill this, mostly etching procedures based on oxygen are used to realize diamond-NVC hybrid systems. To name some examples of the developed RIE-ICP processes in diamond structuring through this thesis, besides the ones which will be discussed in detail in chapters 3 and 4, a) anisotropic and b) angled etching procedures will be described in following.

a) To perform anisotropic etching of diamond, the combination of both of the RIE and ICP procedures is simultaneously utilized. In this way, 100 W of RIE, 600 W of ICP, 10 mTorr of pressure, and 30 sccm of oxygen flow rate is applied to the sample. The sample is positioned on top of the RIE plate, which is kept at temperature of $\sim 20^\circ$ C. The explained etching recipe results in approximate etching rate of 170 nm/min for (100)-oriented diamond substrate. The choice of the appropriate etching mask depends on the geometry of the targeted structure as well as the etching depth, etc. For example, to realize the diamond nanopillar structures, FOX 25 is chosen as the etching mask. As described in the last section, it is a negative electron resist which is shown to be an excellent etching mask against oxygen plasma. As can be seen in Figure 2.4-(a), this resist is deposited on top of the diamond surface. The presented FOX pillar mask has an approximately uniform diameter of 200 nm and a height of 420 nm. Afterward, the substrate is etched by means of the given plasma recipe for about 1.2 μm. As can be seen, the geometry of the FOX pillar is transferred to the diamond substrate, while only $\sim$ 150 nm of FOX 25 mask is remained after etching (see Figure 2.4-(b)). This residual FOX 25 resist can be removed e.g. by immersing the sample in buffered HF solution for few minutes (see Figure 2.4-(c)). Given the mentioned etched depth of diamond and FOX, etch selectivity of ≈ 4.5 is achieved. It is seen that this etch selectivity is dependent on the temperature of the sample during the etching process. For instance, by setting the RIE plate temperature to -30° C, the same amount of FOX 25 mask could stand against ≈ 1.8 μm of diamond etching, thus giving etch selectivity of ≈ 6.5. In both cases, the obtained etching selectivity is seen to be independent of the crystallographic orientation of the diamond substrate. For instance, for both of the (100)- and (111)- oriented diamond substrates, the same dimensions of the diamond nanopillar structure is measured after the etching process. It should be mentioned that, the size of the FOX 25 mask affects the associated etch selectivity a lot. For instance while the mask of $\sim$ 100 nm shows etch selectivities less than 10 (discussed earlier), microscale FOX 25 masks show minimum etch selectivity of 30.

b) The vertical etching, as described above, is capable of transforming the geometry of the

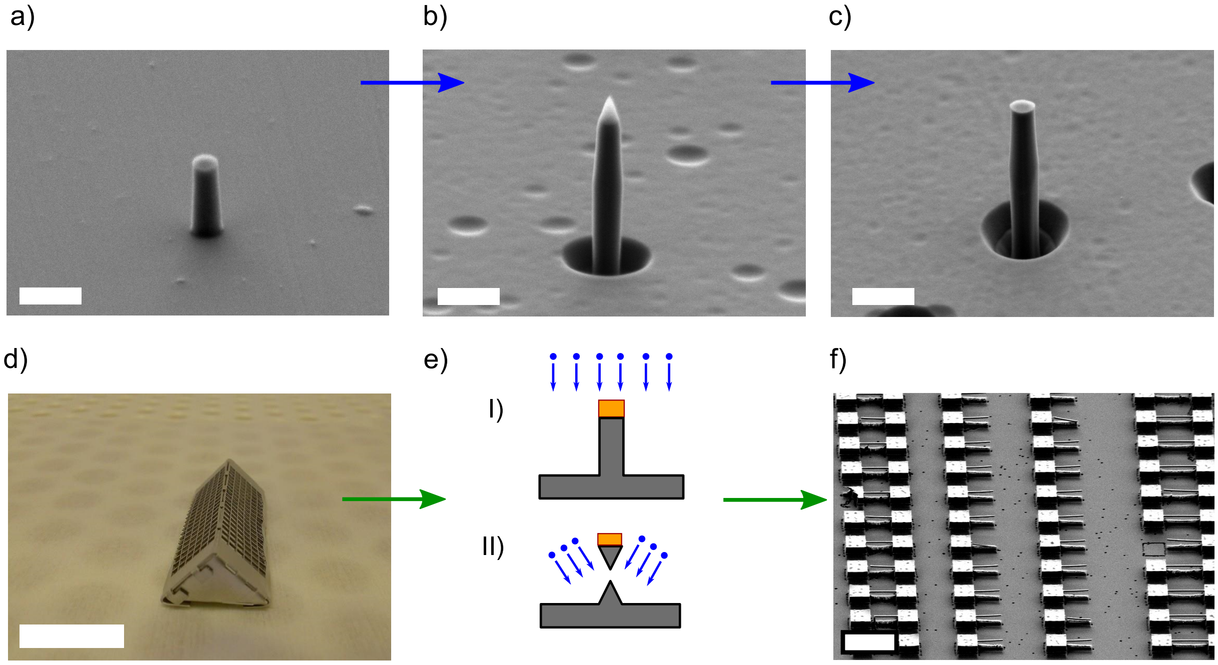

Figure 2.4.: Transverse (a, b, c) and angled (d ,e, f) etching of diamond substrate is demonstrated. a) Shows the FOX 25 etching mask on top of the diamond substrate. Scale bar shows 400 nm. b) Diamond substrate is etched by means of oxygen RIE-ICP procedure using the mask shown in (a). As can be seen, the diamond nanopillar geometry is realized, while $\sim$ 150 nm of the FOX 25 remains. Scale bar shows 400 nm. (c) Residual of the etching mask is removed by leaving the sample for few minutes in buffered HF solution. Scale bar shows 400 nm. (d) Shows the constructed Faraday cage to perform the angled etching process of diamond substrate. The cage is an aluminum prism with triangular cross-section of $\sim$ 2 cm. Scale bar shows 2 cm. To perform such a way of etching, first transverse etching of diamond is accomplished. Then, angled way of diamond etching is pursued by introducing the Faraday cage shown in (d) to the etching chamber. f) An example of angled etching process is shown. Single-side and double-side clamped nanobeams with lateral dimensions of $\sim$ 200 nm and length of $\sim$ 5 μm are fabricated. The white color of the structures is due to presence of the residual of Cr etching mask. Scale bar shows 10 μm.

etching mask to the substrate in a vertical way. Therefore, realization of suspended structures by means of this method is not feasible. Although alternative methods like FIB milling can be instead employed, the etching procedure is still preferable. This preference roots in key characteristics of plasma etching such as the required etching time independence on the number of desired structures within a chip, and absence of the secondary material depositions (like Ga) in the case of FIB milling [61, 50]. In this part of applications of the plasma etching procedure, directional (angled) etching of diamond is discussed. In this method, perpendicular (to the sample) etching still exists, however, directional etching is added by employing a Faraday cage inside the RIE-ICP chamber around the sample. The mentioned Faraday cage is a triangular cross-section aluminum prism that is positioned on top of the RIE plate under which the diamond sample is located (see Figure 2.4-(d)). This Faraday cage shields the substrate from electromagnetic fields. Thus, the plasma ions inside it accelerate along a path perpendicular to the cage surface. Once the ions are inside the cage, they are no longer accelerated and hence, directed to the sample surface with an angle which is dictated by the given geometry of the Faraday cage [61, 50]. To utilize this method to realize free-standing diamond nanobeams, a bulk diamond substrate from Element Six is chosen as the starting chip substrate. A Cr etching mask is patterned on top of it by means of the previously-described e-beam lithography and lift-off processes. Then, the vertical etching process is performed by applying RIE-ICP process based on oxygen plasma. Afterward, the Faraday cage is placed on top of the sample, inside the plasma chamber, and the etching process is pursued. It is seen that by introducing the Faraday cage, the etching rate is decreased. Nevertheless, high quality directional etching performance can be achieved (see Figure 2.4-(e)). As presented in Figure 2.4-(f), single-side and double-side clamped free-standing diamond nanobeams with width of $\sim$ 200 nm and length of $\sim$ 5 μm are fabricated. A visible distance (clearance) between the diamond nanobeam and the diamond substrate ($\approx$ 2 μm) truly proves the angled etching procedure. These diamond nanobeam structures can be used as nanophotonic [62, 63] and nanomechanical architectures. In chapter 4, hybrid mechanical diamond-NVC structures will be discussed in detail.

2.4. Summary and outlook

In this chapter, two main parts of semiconductor fabrication technology, i.e. electron beam lithography and plasma etching are reviewed. Their utilization under the frame of this thesis to fabricate hybrid diamond-NVC structures are discussed. The main challenge to utilize these techniques can be rooted in properties of diamond and, the special care which should be considered to preserve the properties of the embedded NVCs during the structuring process. Successfully, fabrication procedures using the mentioned techniques are developed to provide hybrid high quality diamond-NVC structures. In this chapter, production of an array of coupled NVCs, optimized surface treatment of diamond substrate with shallow NVCs and, nanophotonic and nanomechanical diamond nanostructures are demonstrated. Given the knowledge presented in this chapter, the reader can follow the fabrication parts of chapters 3 and 4 in a better way.

3. Hybrid Diamond-NVC Photonic Structure

The demonstrated results in this
chapter are mainly presented
and published in [64], S. Ali
Momenzadeh *et al.* Nano Lett.,
2015, 15 (1), pp 165-169.

Detecting external magnetic fields is one of the key applications of NVCs in diamond (see chapter 1). As discussed, for using NVCs as magnetic field sensors (magnetometers), their proximity to the magnetic material under investigation is of vital importance. The magnetic field sensitivity of such a magnetometer is limited additionally by the spin coherence times (T_2 and T_2^*) of the NVC probe and the number of collected fluorescence photons. Therefore, to deliver a sensitive magnetometer ($\delta\mathrm{B} \sim \mathrm{nT}/\sqrt{\mathrm{Hz}}$) based on the NVC probe, one should aim for an augmented collection of the fluorescence photons of the NVC probe, while this probe should be positioned few nanometers below the diamond surface and still possess long coherence times. This sounds challenging since e.g., as of today, there is a trade-off between the depth of NVCs and their coherence properties due to surface spin noise. Nevertheless, one can consider NVCs inside diamond nanocrystals [42, 65, 66] as the fundamental system to utilize for NVC magnetometry. The suitability of these systems as magnetometers can be however ventured by some key issues such as poor coherence times [67] and photostability, large and not controllable distance from the diamond surface, and random orientation of the symmetry axis and hence spin component of the NVC probe with respect to the external magnetic field. Although most of these issues have been addressed and solved in recent years, employing NVCs embedded into the bulk diamond is still more controllable and preferable in magnetometry applications [68]. In this chapter, a hybrid quantum structure consisting of a diamond photonic nanostructure and embedded NVC quantum probe is presented. An engineered conically-tapered nanopillar as the waveguide for efficient optical excitation and fluorescence photon collection of a single shallow NVC located at its extremity forms this hybrid architecture. An order of magnitude enhancement in the photon collection efficiency, in comparison to the NVC under the nonstructured diamond surface, followed by conservation of the spin coherence times, sets this architecture as a robust bright platform for NVC-based magnetometry as well as scanning probe applications.

In this chapter, required theoretical backgrounds for the development and characterization of the mentioned hybrid structure will be reviewed. In this regard, photophysics of NVCs followed by introductory information about electric dipoles inside optical fibers will be presented. Then, theoretical and numerical simulations to achieve the optimized geometry towards enhanced photon collection efficiency will be given which will be followed by demonstration of the fabrication process. Next, experimental results of the benchmark experiments on the optical and spin interfaces of the NVCs inside the mentioned structure will be shown. At the end, few perspectives, as the next-generation applications of this hybrid geometry, will be discussed.

3.1. Theoretical backgrounds

Assuming an NVC inside a photonic waveguide structure, the number of the collected photons per unit time is given by $\Gamma(\lambda)\cdot\eta(\lambda)$, where Γ and η are the wavelength (λ)-dependent emission rate of the NVC and the photon collection efficiency of the photonic structure, respectively [34]. The former is reciprocal to the optical lifetime of the NVC, while the latter is given by the coupling efficiency of the NVCs to different modes of the waveguide and the extraction efficiency of the photons from those waveguide modes. In this section, photophysical properties of the NVCs will be discussed. In this manner, NVCs will be mainly studied as classical electric dipoles inside the diamond lattice.

Based on Fermi's golden rule, the spontaneous emission rate of this dipole at a position $\vec{r}$ is determined by [69]:

$$\Gamma = \frac{\pi\omega}{\hbar}\sum_{\vec{k},\sigma}\left|\vec{\mu}\cdot\vec{E}_{\vec{k},\sigma}(\vec{r})\right|^2 \delta(\omega-\omega_{\vec{k},\sigma}), \tag{3.1}$$

where ω is the optical transition frequency of the NVC, and $\vec{\mu}$ is its dipole moment. $(\vec{k},\sigma)$ are the wavevector and polarization of all the possible modes of the photons, where these modes have the local electric field shown as $\vec{E}$. As can be seen, for the emission rate of NVCs, their dielectric environment i.e. geometry and effective refractive index of the host material, their position and orientation inside the host material, and the electric fields of each optical modes at the their location must be taken into account. This dependence, which was given in Eq. (3.1), is known as electromagnetic linear density of states (LDOS), expressed as [69]:

$$\frac{1}{|\vec{\mu}|^2}\sum_{\vec{k},\sigma}\left|\vec{\mu}\cdot\vec{E}_{\vec{k},\sigma}(\vec{r})\right|^2 \delta(\omega-\omega_{\vec{k},\sigma}). \tag{3.2}$$

In the nonstructured diamond host, the optical emission and excitation of the NVC is combined of many different optical modes which imposes difficulties on the analytical calculation of Eqs. (3.1) and (3.2). Therefore, in a more general way as an alternative approach, the photophysics

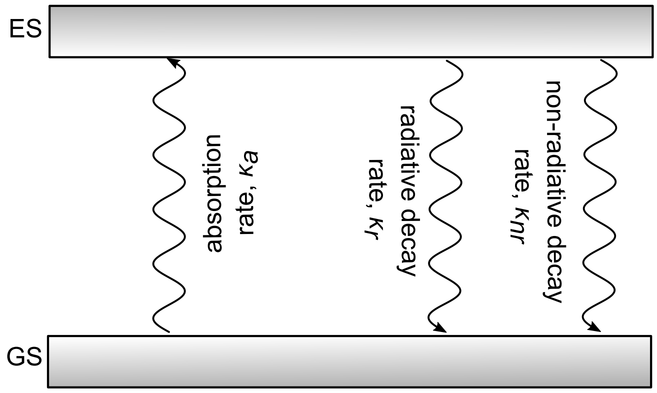
ES
GS
absorption rate, κ_a
radiative decay rate, κ_r
non-radiative decay rate, κ_{nr}

Figure 3.1.: Optical absorption and excitation are shown in an optical two-level system. The absorption, radiative, and non-radiative decay rates are noted with κ_a, κ_r, and κ_{nr}, respectively.

of the NVC will be discussed in following using the optical two-level system model.

3.1.1. Optical two-level system

The optical two-level model represents an emitter system composed of ground state (GS) and excited state (ES) separated by transition energy of $\hbar\omega$ (see Figure 3.1) [70]. In this scheme, given the absorption cross-section σ of the emitter under the illumination intensity of I_i (photons/m^2·s), the absorption rate (κ_a) of the emitter from GS to the ES is expressed by $\sigma \cdot I_i$. Then, a return to the GS will happen either through radiative (fluorescence), or non-radiative decays associated with the radiative and non-radiative decay rates of κ_r and κ_{nr}, respectively. In this case, the average lifetime of the ES is defined as $\tau_e = 1/\kappa_e$ assuming $\kappa_e = (\kappa_r + \kappa_{nr})$ as the decay rate of the ES. Increasing the illumination intensity, there will be a saturation point at which the absorption rate is equal to the decay rate of the ES. The corresponding saturation illumination intensity (I_s) can be shown as κ_e/σ. When the emitter is in the ES after the absorption of a photon, it cannot absorb another one. Nevertheless, it relaxes to its GS, and after a time average of τ_p = $1/\kappa_a$ can absorb another photon. Therefore, the probability of a photon to excite the emitter in an arbitrary time is smaller than unity and can be given by:

$$P_a = \frac{\tau_p}{\tau_e + \tau_p} = \frac{I_s}{I_i + I_s}. \tag{3.3}$$

The amount of the absorbed light by the emitter in this case can be seen as $I_i \cdot P_a$. Therefore, the fluorescence intensity (I_f) of the emitter will be equal to the fraction of the excited-state and radiative-decay (fluorescent) lifetimes multiplied by the above-calculated absorbed light intensity. By performing the following calculation:

$$I_\mathrm{f} = \left(\frac{k_r}{k_r + k_{nr}}\right) \cdot \left(\frac{I_i \cdot I_s}{I_i + I_s}\right) = \underbrace{\left(\frac{k_r}{k_r + k_{nr}} \cdot I_s\right)}_{I_\mathrm{f,sat}} \frac{1}{1 + \frac{I_s}{I_i}} \Rightarrow \frac{I_\mathrm{f}}{I_\mathrm{f,sat}} = \frac{1}{1 + \frac{I_s}{I_i}}, \tag{3.4}$$

and by converting the illumination intensity to the illumination power and also the fluorescence intensity to the fluorescence rate, the fluorescence rate of the emitter (F in photons/s) within the two-level system frame as a function of the illumination laser power (P) can be written as:

$$F = \frac{F_\mathrm{s}}{1 + \frac{P_\mathrm{s}}{P}}, \tag{3.5}$$

where F_s and P_s are the saturation fluorescence rate and saturation power, respectively.

In case of NVCs, experimental observations such as second-order time-intensity photon correlation measurements [71, 72] promote the existence of a third level, namely a shelving metastable state (MS), and therefore deviation from the two-level picture. In the coming subsection, the phenomenological study of the three-level system will be carried out, where the fluorescence intensity correlation function and its relation to the net and background fluorescence intensities of the NVC will be derived.

3.1.2. Optical three-level system

To study the NVC optical behavior in a more precise way, considering the presence of the metastable state (MS) is inevitable. This state resembles a trap in which the system is kept for hundreds of nano-seconds [71]. As shown in Figure 3.2, the population is pumped from the GS to the ES, where it decays with the decay rate of Γ_1 from the ES to the GS. In contrast to the two-level system, another decay channel is also possible featuring decay rates of Γ_2 and Γ_3 from the ES to the MS and from the MS to the GS, respectively. The other non-shown transitions will be neglected hereinafter. To get the right quantitative image of the optical three-level system describing the photodynamics behavior of the NVC, the relevant rate equation (Eq. 3.6) for the population of the GS, ES, and the MS should be solved, while the assumption of $P_\mathrm{GS} + P_\mathrm{ES} + P_\mathrm{MS}$=1 and $P_\mathrm{GS}(\tau = 0)$ =1 and $P_\mathrm{ES}(\tau = 0) = P_\mathrm{MS}(\tau = 0) = 0$ should be taken into account as the initial conditions of the system [71, 72].

$$\frac{d}{dt}\begin{pmatrix} P_\mathrm{GS} \\ P_\mathrm{ES} \\ P_\mathrm{MS} \end{pmatrix} = \begin{pmatrix} -k & \Gamma_1 & \Gamma_3 \\ k & -\Gamma_1 - \Gamma_2 & 0 \\ 0 & \Gamma_2 & -\Gamma_3 \end{pmatrix} \begin{pmatrix} P_\mathrm{GS} \\ P_\mathrm{ES} \\ P_\mathrm{MS} \end{pmatrix} \tag{3.6}$$

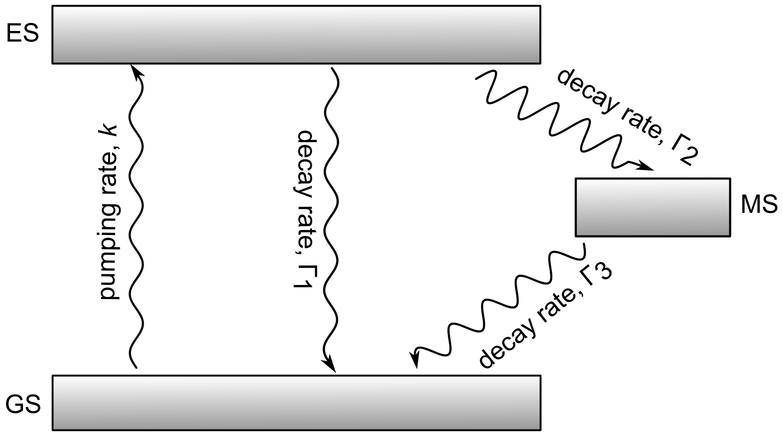

Figure 3.2.: The scheme of an optical three-level system including the GS, ES, and the MS states is shown. The pumping and decay rates of k, Γ_1, Γ_2, and Γ_3, respectively, are depicted.

Solving the rate equation shown in Eq. (3.6) considering the above-mentioned conditions yields in the second-order correlation function $g^{(2)}(\tau) = \frac{P_{\mathrm{ES}(\tau)}}{P_{\mathrm{ES}(\infty)}}$ to be read as [72]:

$$g^{(2)}(\tau) = 1 - \beta e^{-\gamma_1 \tau} + (\beta - 1)e^{-\gamma_2 \tau}, \tag{3.7}$$

where the employed constants are written as:

$$\gamma_1 \approx k + \Gamma_1, \tag{3.8}$$

$$\gamma_2 \approx \Gamma_3 + \frac{k\Gamma_2}{k+\Gamma_1}, \tag{3.9}$$

$$\beta \approx 1 + \frac{k\Gamma_2}{\Gamma_3(k+\Gamma_1)}. \tag{3.10}$$

As can be seen in Eq. (3.7), the $g^{(2)}$ at the delay time $\tau = 0$, is equal to zero since there is zero probability to detect a photon from a single-photon emitter, if one has just been detected. In the case of N emitters, the $g^{(2)}(\tau = 0)$ is equal to 1-$\frac{1}{N}$ [72]. In the case of NVCs, even with the presence of only a single emitter, $g^{(2)}(\tau = 0) \neq 0$ is usually detected, which can be due to the noise sources like the background signal originating from the hosting diamond structure, or the fluorescence background from other emitters close to the one under investigation. To study this case, the total measured intensity of a single NVC consisting of $\langle i \rangle$ as the pure (net) intensity of a single NVC and $b \cdot \langle i \rangle$ as the Poissonian background intensity [72, 35] is assumed. Therefore, one can write the $g^{(2)}$ function for the total intensity in the general case of N emitters as follows:

$$g^2_{\text{total}}(\tau) = \frac{\left\langle \left(\sum_{j=1}^{N} i_j(t) + b\left\langle i\right\rangle\right)\left(\sum_{k=1}^{N} i_k(t+\tau) + b\left\langle i\right\rangle\right)\right\rangle}{\left\langle \left(\sum_{j=1}^{N} i_j(t) + b\left\langle i\right\rangle\right)\right\rangle^2}. \tag{3.11}$$

By assuming $N = 1$ for the single emitter case and $g^{(2)}(\tau = 0) = 0$ for a net NVC intensity signal, Eq. (3.11) at delay time of $\tau = 0$ is given by:

$$g^2_{\text{total}}(\tau = 0) = 1 - \frac{1}{(b+1)^2}. \tag{3.12}$$

By multiplying $\langle i\rangle$ to the nominator and denominator of Eq. (3.12), it can be rewritten as:

$$g^2_{\text{total}}(\tau = 0) = 1 - \left(\frac{\langle i\rangle}{\langle i\rangle + B}\right)^2, \tag{3.13}$$

where $B = b \cdot \langle i\rangle$ is the background signal intensity.

So far, the photodynamics of the NVCs independent of their host diamond structure are reviewed. However, as already mentioned, number of the collected photons per second is also dependent upon the host structure of the NVC, the optical modes and the interaction of the NVC with these modes. In this section, accordingly, an introductory information about the cylindrical dielectric waveguides (fiber) and the emitter dipoles inside those structures will be given.

3.1.3. Optical fibers

Here, cylindrical dielectric waveguides, i.e. optical fibers will be shortly reviewed. Among them, the step-index fibers (hereinafter will be shortly mentioned as fiber) will be focused upon [73, 74]. In fibers, the refractive index of the core (n_c) is higher than that of the cladding (n_{cl}). An optical ray inside such a fiber is guided via the TIR effect when its angle of incidence with respect to the fiber axis is smaller than $\sin^{-1}(n_{cl}/n_c)$. With respect to the refractive indexes of the core and the cladding of the fiber, and also the radii r_a and r_b (Figure 3.3), the fiber can guide different optical modes. In this way, it is convenient to define the V parameter which governs the number of the modes and their corresponding propagation constants. This fiber V parameter is written as:

$$V = \frac{2\pi}{\lambda} \cdot r_a \cdot NA, \tag{3.14}$$

where NA of the fiber in Eq. (3.14) is given by:

$$NA = \sqrt{n_c^2 - n_{cl}^2}. \tag{3.15}$$

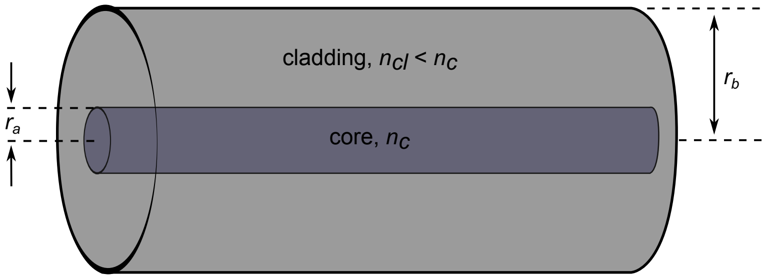

Figure 3.3.: The scheme of a step-index fiber with the radii of r_a and r_b of the core and cladding, respectively, is shown. As mentioned, the refractive index of the cladding is smaller than that of the core ($n_{cl} < n_c$).

In principle, two distinct sets of optical modes can be attributed to a fiber; "guided" and "radiation" modes. For guided modes, the radial part of the modal field is oscillatory only in the core of the fiber and decays in the cladding, while for the radiation modes, the fields are oscillatory even in the cladding. Each mode in a fiber is associated with its propagation constant β that can be written as $n_{eff} \cdot k$ dependent on the effective refractive index of its mode in the fiber n_{eff} and its wavenumber k. For guided modes, $n_{cl}^2 < n_{eff}^2 < n_c^2$ satisfies, where for the case of radiation modes $0 < n_{eff}^2 < n_c^2$ is true. The propagation constant β can take continuous values for the radiation modes, while it can only assume discrete values for the case of guided ones [74]. For a given geometry of a fiber with the associated V parameter, the number of the guided modes is $\approx \frac{1}{2}V^2$ at the limit of large V parameter [74].

For each mode, there is a value of the V parameter below which it cannot be guided. For instance, in a fiber with $V < 2.405$ only one guided mode exists. This fiber is called single-mode, and is of a remarkable importance in optical communication systems. The guided mode of such a fiber, i.e. the fundamental mode, resembles the Gaussian mode [75], for which the highest confinement of the light occurs within the fiber core. Given a specific wavelength of the optical beam, and refractive indexes of the core and cladding, the fiber core radius can be chosen in a way such that the fiber only guides the fundamental mode and cuts the higher modes. In this case, the radius of the fiber core, based on the above-mentioned information can be written as:

$$r_a = \frac{\lambda}{2.61\sqrt{n_c^2 - n_{cl}^2}}. \tag{3.16}$$

Based on the geometry and refractive indexes of the fiber, or equivalently its V parameter, the normalized propagation constant of the fiber can be introduced by $b(V) = \frac{n_{eff}^2 - n_{cl}^2}{n_c^2 - n_{cl}^2}$, which

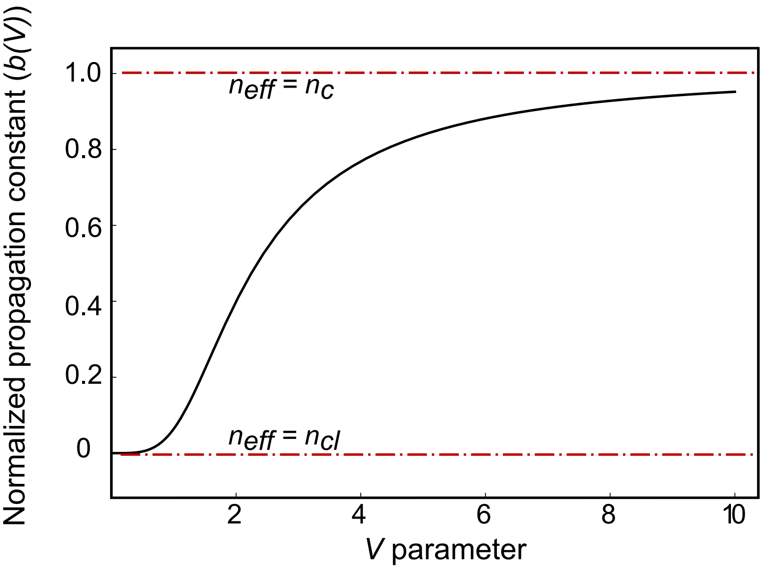

Figure 3.4.: The variation of the normalized propagation constant and accordingly the effective refractive index of the fundamental mode of the fiber is shown vs. its V parameter. As depicted, the effective refractive index of the fiber for the fundamental mode is bound between the refractive index of the cladding and that of the core.

satisfies $0 < b(V) < 1$ for the guided modes. For the fundamental mode, $b(V)$ is read as [74]:

$$b(V) = 1 - \frac{\left(\frac{(1+\sqrt{2})}{1+(4+V^4)^{1/4}}\right)^2}{V^2}. \tag{3.17}$$

This size-dependent variation of the effective refractive index of the fundamental mode inside a fiber (Eq. (3.17)) is shown in Figure 3.4.

3.1.4. NVC as an electric dipole inside a fiber

In this part, the emission of an electric dipole associated with an NVC inside an optical fiber with core radius a will be qualitatively investigated [76]. Given a dipole moment $\vec{P}_0$ of the dipole with the frequency of ω at the position of $\vec{r}_0$ (see Figure 3.5-(a)), the polarization density will be given by $\vec{P}(\vec{r})=\vec{P}_0 \exp(i\omega t)\delta(\vec{r} - \vec{r}_0)$. The total emission power of this dipole is given by summing the power emitted to each discrete guided mode (j) and also continuous radiation ones, i.e.:

$$P_{total} = \sum_j P_j + \sum_V \int P_V(Q)dQ, \tag{3.18}$$

where Q is defined as $a \cdot \sqrt{k^2 n_{cl}^2 - \beta^2}$. Assuming an NVC dipole radially oriented at the center of the fiber core and emitting at the wavelength of 700 nm (the cladding of the fiber is set as air), one can calculate Eq. (3.18) for the fiber with different core materials, i.e. refractive indexes. As depicted in Figure 3.5-(b) and Figure 3.5-(c), the core diameter and also the refractive index of the fiber core strongly manipulate the emitted power. It should be expressed that in Figures 3.5-(a) to -(c), the normalized power, i.e. the emitted power expressed in Eq. (3.18) divided by the emitted power into the bulk diamond host structure is shown. As shown in Figure 3.5-(c), as the core diameter is increasing, the normalized power reaches the maximum value at a certain diameter, after which it will show fluctuation behavior. Equivalently, as the fiber core diameter increases more guided modes appear, which cause the mentioned fluctuation behavior. In addition to the core diameter, radial position of the dipole also affects the captured power of the dipole by the optical modes of the fiber. As illustrated in Figure 3.5-(d), inside the fiber core, the normalized power decreases as the dipole gets far from the fiber core axis.

3.2. FEM simulations of diamond photonic structures

In chapter 1, nanopillar photonic structures directly made onto the diamond thin film (thickness $\sim \mu$m) were introduced as a way to overcome the poor photon collection efficiency of embedded NVCs [36, 77]. In this approach, the nanopillar structure works as a waveguide in which emission of the embedded shallow NVC is coupled to its fundamental mode. Then, guided photons propagate through the back diamond film substrate and finally get collected by the microscope objective lens below the diamond film. Parallel to this importance, they were also presented to be integrated into all-diamond scanning probes in NVC-based magnetometry experiments. To optimize the magnetic field sensitivity of this structure in the magnetometry applications, increasing the photon collection efficiency of the shallow NVCs, while importantly preserving their spin coherence properties, is targeted here. It should be noted that due to the aimed application, only the monolithic diamond structure is considered here and non-monolithic solutions are excluded (see chapter 1). The general scheme of such a nanopillar platform is presented in Figure 3.6. This nanopillar structure can be assumed as a waveguide, i.e. a step-index fiber with air cladding, containing a dipole emitter. Therefore, with respect to the given information in the last section, the total number of collected photons emitted by the shallow NVC emitter located at the extremity of the nanopillar structure depends on the spontaneous emission rate of the emitter, furthermore is dependent upon the i) position and orientation of the NVC inside the structure, ii) the geometry of the nanopillar structure, e.g. its radius, iii) the propagation of the emitted photons through the interface of the nanopillar

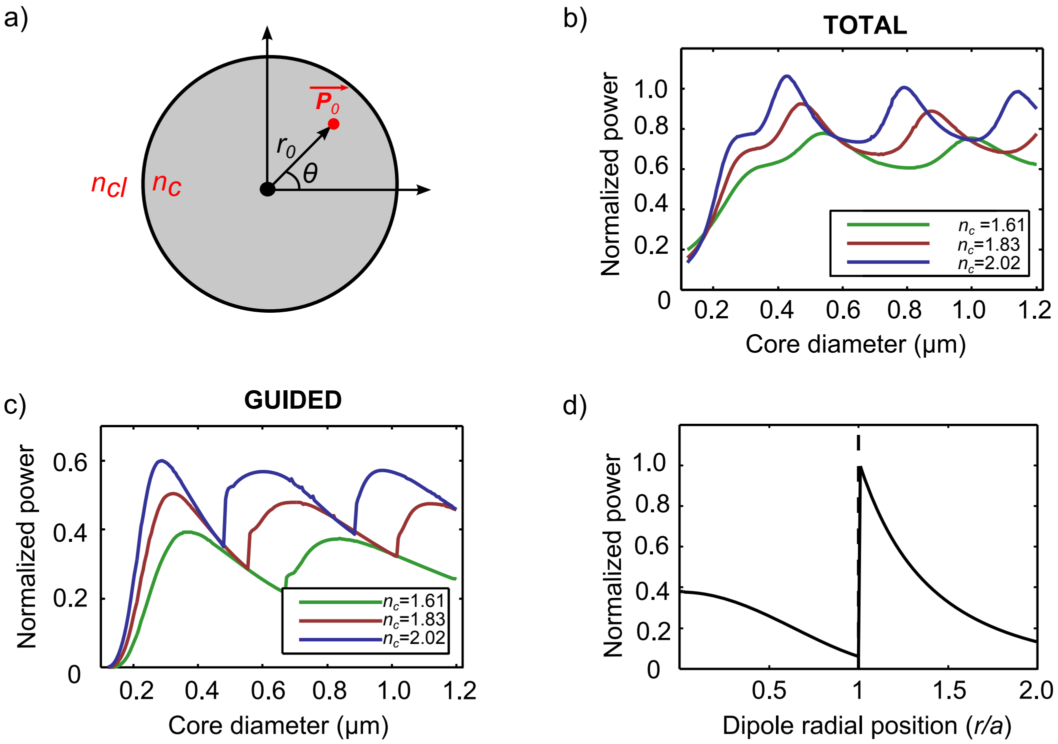

Figure 3.5.: a) Schematic cross-sectional view of an NVC dipole inside a step-index fiber is shown. b) and c) The normalized power of an NVC dipole oriented radially at the center of the fiber core emitting at λ = 700 nm captured by the total modes (b) and only guided modes (c) of the fiber is plotted vs. the fiber core diameter. Insets in (b) and (c) give different refractive indexes associated with different core material. Fluctuation behavior in the normalized power due to the presence of new modes inside the fiber is observed. d) The normalized power of a radially-oriented NVC emitting at λ = 700 nm inside a fiber core with n_c = 2.02 and diameter of 220 nm is plotted vs. its radial position (a is the radius of the fiber core). At $r/a = 1$, the sharp change is due to the discontinuity of the radial field at the core-cladding interface. Figures (b), (c), and (d) are taken from [76].

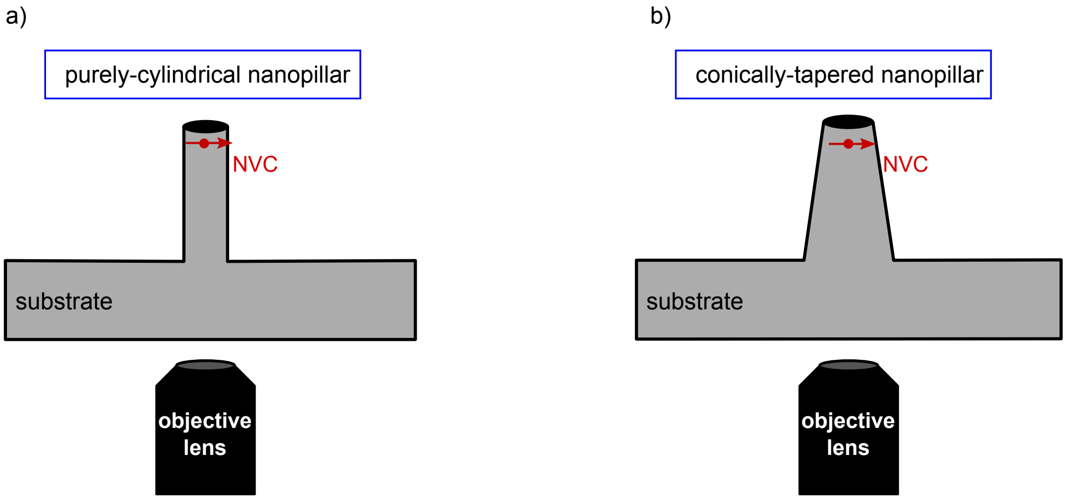

Figure 3.6.: The general sketch of the purely-cylindrical (a) and conically-tapered (b) nanopillar geometries hosting a single shallow NVC is depicted.

structure and the diamond substrate, iv) propagation of the emitted photons inside the bulk substrate and their transmission through the bulk diamond - air interface and eventually v) collection of the photons by the objective lens.

To simulate the nanopillar hybrid architecture to achieve the optimized collected number of photons emitted by the shallow NVCs at its extremity, no change in the spontaneous emission rate (Purcell effect) of the NVC is assumed which will be experimentally verified later. In contrast, improving the number of collected photons is targeted. In this regard, 3D finite element method (FEM) simulation technique is used in which electric field pattern of the NVC dipole with the emission wavelength of $\lambda = 637$ nm is studied. Importantly, depth of 5 nm for NVCs under the apex of diamond nanopillars is selected throughout the whole simulations. As previously discussed, depth and coherence time of shallow NVCs feature a trade-off behavior. Some challenges such as the vicinity to the imperfect diamond lattice quality at the surface [25] and the possible defects surrounding the implanted shallow NVCs can truncate their coherence times. Nevertheless, NVCs with approximate T_2 coherence time of 50 μs are reported [78, 26] for single NVCs with depth of $\approx$ 5 nm in a bulk diamond substrate.

The orientation of the NVC dipole inside the nanopillar waveguide also changes the performance of the presented hybrid structure. This orientation depends on the crystallographic orientation of the host diamond material. In the following simulation, the NVC dipole is always considered to be radially aligned inside the nanopillar (assuming a cylindrical coordinate system). Furthermore, the total number of the collected photons is also affected by the objective lens utilized in the confocal microscope. In the presented simulations identical to the experiment, an air objective lens with the numerical aperture of $NA = 0.95$ is utilized. By this objective lens, photons from the focused NVC within the maximum angle of $\approx 144^\circ$ can be collected. It should be additionally noted that, in all the following FEM simulations, thickness of the diamond substrate is set to 2 μm to avoid unnecessary computational effort.

3.2.1. Geometry of the nanopillar

Nanopillar geometry, as the waveguide for the photons emitted by the shallow NVC, obviously plays the crucial role on the collected number of the photons via the NVC-nanopillar hybrid system. In a simplified sketch, the nanopillar structure with the purely cylindrical geometry (see Figure 3.6-(a)) can be resembled as a step-index fiber with the $n_c = 2.4$ and $n_{cl} = 1$ refractive indexes for the diamond core and the air cladding, respectively. The height of this geometry in the following simulation is set to be 1.2 μm, which is the maximum reliable height achievable by the employed fabrication process (will be explained in detail in section 3.3). The radius of this structure manipulates the number of the modes inside it and hence the total performance of the hybrid structure. Based on Eq. (3.16), this geometry with the diameter of $\approx$ 224 nm performs as a single-mode cylindrical waveguide for the emission of the NVC ($\lambda = 637$ nm). The collected electric field intensity vs. the purely-cylindrical nanopillar (Figure 3.6-(a)) diameter and equivalently the number of guided modes is simulated via a FEM software and is demonstrated in Figure 3.7.

As shown, by increasing the nanopillar diameter, the collected electric field intensity also increases which reaches its maximum at the diameter of $\approx$ 250 nm. As calculated, this diameter is approximately the transition from single-mode to multimode waveguide. For larger diameters, the collected electric field intensity exhibits a slight modulation which corresponds to the resonances of the guided modes with respect to the diameter of the waveguide [76]. It should be emphasized that only the total number of the collected photons is aimed to be optimized here and other optical parameters such as number of the modes etc, are not of direct interest.

In addition to affecting the photon collection efficiency of the hybrid structure, the diameter of the nanopillar and accordingly the required fabrication procedure might affect the coherence times of the probe NVC. This can be due to e.g. side effects of the involved deposition or etching steps (see the next section for more details). To minimize the negative effects imposed by the fabrication process, the top diameter of the nanopillar geometry is set to be $\approx$ 400 nm. As can be seen in Figure 3.7, no major difference in the collected electric field intensity exists between purely-cylindrical nanopillar diameters of 250 nm and 400 nm.

The propagation of the photons emitted by the NVC located at the extremity of the nanopillar structure to the objective lens occurs through three different media: 1) nanopillar geometry

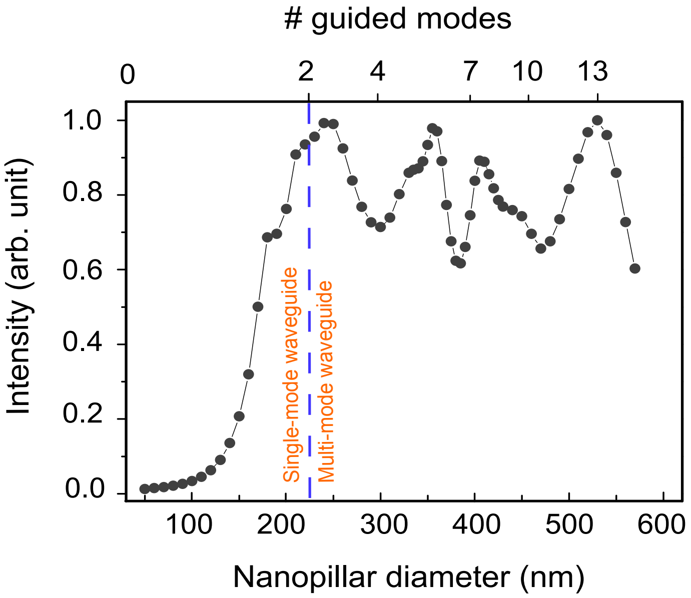

Figure 3.7.: FEM simulations towards optimization of the collected photon intensity of an NVC located on the axis of the purely-cylindrical nanopillar geometry, 5 nm below the diamond surface is shown. This plot shows the intensity of the collected electric field vs. the diameter of the purely-cylindrical nanopillar geometry (and equivalently, number of the guided modes).

which acts as a nanowaveguide and 2) the thin diamond film substrate under the nanopillar structure, and 3) the air between diamond and the objective lens. In this way, the emitted photons couple with different modes of the nanopillar geometry. Each of these modes are associated with their characteristic propagation constant which depends on the diameter of the nanopillar geometry (see the last section). These photons should propagate through the interface between these two media (1 and 2) that are of different sizes (in comparison to the emission wavelength of the NVC) and then travel to the objective lens. Therefore this interface can affect the collection efficiency of the photons, emitted by the NVC. This aspect is optimized by considering a conically-tapered nanopillar geometry (see Figure 3.6-(b)) in which the bottom diameter is varied independently from the top one. This variation modifies the effective refractive index and as a result, the propagation constant for each mode of the nanopillar. This can also be seen as propagation of a wave from a medium to another one with different refractive indexes. In this way, as shown e.g. in [79], matching the impedance between these two media can yield to the improved transmission efficiency. Having the transmission optimized, the higher collection efficiency of the NVC emitted photons through the structure can be achieved. As shown in Figure 3.8, the collected electric field intensity generally increases vs. the bottom diameter of the nanopillar geometry, reaching the maximum value around bottom diameter of 1.3 μm, and decays afterward. This decay can be due to

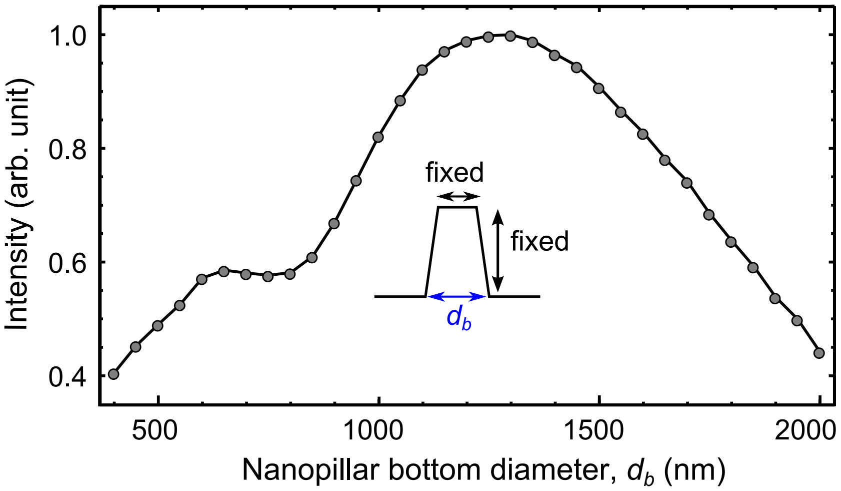

Figure 3.8.: Optimization of the collected photon intensity of an NVC located 5 nm below the diamond surface at the axis of the conically-tapered nanopillar geometry with the top diameter of 400 nm, via FEM simulation is shown. The intensity of the collected electric field intensity is studied vs. the bottom diameter of the nanopillar (d_b) while the height and top diameter are fixed (see the inset) at 1.2 μm and 400 nm, respectively.

the loss of the collected photons caused by the poor guiding performance of the waveguide. As depicted, the collected electric field intensity for a conically-tapered nanopillar with the bottom and top diameters of 400 nm and 1.3 μm, respectively, is $\sim$ 250% higher than that for a purely-cylindrical nanopillar with the diameter of 400 nm. By means of the applied fabrication process (see section 3.3), conically-tapered nanopillar structures possessing height of $\approx$ 1.2 μm with the top diameter of 400 nm and bottom diameters only up to 900 nm could be realized. Therefore, in the following simulations, exclusively this structure will be investigated. For such a nanopillar geometry, the emitted electric field intensity pattern of the NVC dipole is demonstrated in Figure 3.9.

3.2.2. Position of the NVC inside the nanopillar geometry

Due to the non-deterministic structuring of the nanopillar geometry with respect to the implanted NVCs in the fabrication process (see the next section), the radial position of the NVCs with respect to the nanopillar axis is randomly distributed. As mentioned before, e.g. in the discussion of Eq. (3.18), the maximum emitted power comes from an emitter dipole radially at the center of the nanopillar geometry. The more the emitting dipole inside the nanopillar recedes from its axis, the more the emitting power decreases (see Figure 3.5-(d)). In this part of the FEM simulations, the radial position of an NVC dipole 5 nm below the diamond surface inside a conically-tapered nanopillar with bottom and top diameters and height of 900 nm, 400 nm, and 1.2 μm, respectively, is varied (see Figure 3.10). It should be noted that common to

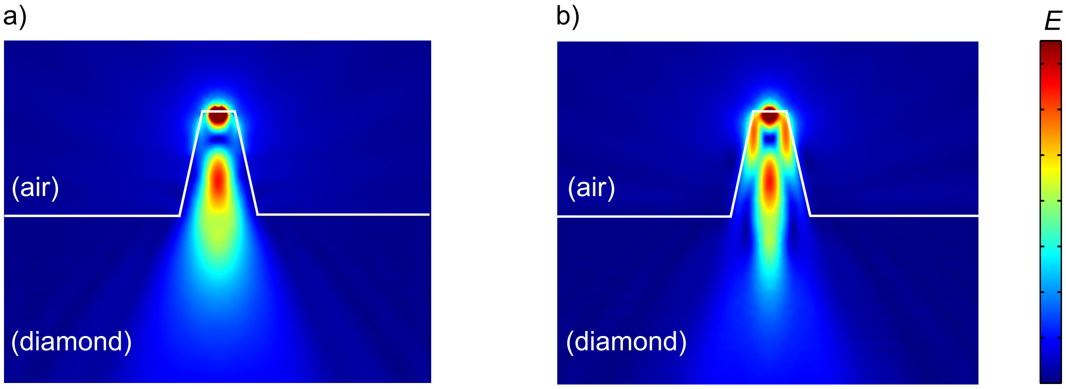

Figure 3.9.: The electric field intensity pattern emitted by an NVC 5 nm below the diamond surface radially at the center of a conically-tapered nanopillar with bottom and top diameters and height of 900 nm, 400 nm, and 1.2 μm, respectively, obtained from FEM simulations, is shown. (a) and (b) show the in-plane and out-of-plane emission intensity patterns, respectively.

all the cases, the NVC dipole is radially oriented in-plane through this simulation.

3.2.3. Emission wavelength dependency

NVC in diamond has a broad emission spectrum [71] which consists of zero-phonon line (ZPL) at $\lambda \approx 637$ nm and phonon sideband (PSB) from $\lambda \approx 650$ nm to $\lambda \approx 800$ nm. In order to limit the FEM computational effort, all the above-mentioned simulations are executed only for the ZPL wavelength. As discussed at the beginning of this chapter, different emission wavelength for the emitter changes both the emitted power and also the behavior of the waveguide. Here, to check the effect of broad emission spectrum on the presented simulations, the amount of the collected electric field intensity of a single NVC radially aligned at the center of a conically-tapered nanopillar (see Figure 3.9) as a function of the wavelength in the spectral range of the NVC emission is evaluated. By weighting the obtained result with the NVC emission spectrum, it is concluded that by performing the FEM simulations only at the ZPL, the overall collected electric field intensity is overestimated by about 20%. Still, as will be shown later, the FEM simulation results and experimental data consistently show similar behavior.

3.3. Realization of the Nanopillar-NVC hybrid system

To experimentally realize the conically-tapered nanopillar geometry with the bottom and top diameter and height of 900 nm, 400 nm, and 1.2 μm, respectively, first, nitrogen ions ($^{15}N^{+}$) are implanted into a thin diamond film (thickness ~ 30 μm) machined from an initial (100)-

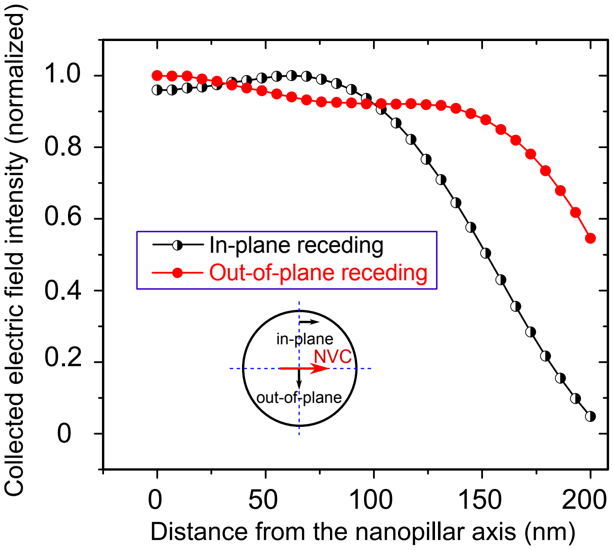

Figure 3.10.: Dependency of the collected electric field intensity of an NVC with the depth of 5 nm inside a conically-tapered nanopillar (height: 1.2 μm, bottom diameter: 900 nm, top diameter: 400 nm) on its distance from the nanopillar axis using the FEM simulation is presented. In this plot the effect of receding both in-plane (black curve) and out-of-plane (red curve) of the electric dipole with respect to the nanopillar axis (see the inset) is shown.

oriented ultrapure electronic grade (^{13}C natural abundance) CVD diamond substrate (see chapter 2). The implantation dose is 100-200 ions/μm^2, where the implantation energy varies at energies of 2.5, 5, and 10 keV. After the ion implantation, the substrate is annealed at the temperature of $\sim$ 900° C for two hours under the vacuum pressure less than 10^{-6} mbar. Next, to remove the non-diamond (graphite) layer at the surface of the diamond, the substrate is boiled in the triacid mixture (H_2SO_4:HNO_3:$HClO_4$; 1:1:1 ratio) for approximately two hours [25]. The generated NVCs are distributed in depth of $\approx$ 3-30 nm, based on the stopping and range of ions in matter software (SRIM [80]).

After generation of NVCs, fabrication of the conically-tapered nanopillar geometry out of the diamond substrate hosting implanted NVCs is accomplished by means of electron-beam lithography technique to make the etching mask, followed by the etching process using RIE-ICP method (see chapter 2 for more details). To that aim, the diamond thin film substrate is glued by PMMA on top of a silicon wafer for structural support. Then, a Cr layer of 5 nm thickness is thermally evaporated on top of the diamond substrate as an adhesion layer. FOX 25 is employed as the electron-beam resist which also acts as the etching mask. After spin coating for 45 seconds at the revolution rate of 6000 rev/min and soft baking of FOX 25 at 90° C for 1 minute (the resulting thickness $\sim$ 450 nm), another 5 nm layer of Cr is deposited as an anti-charging layer. The exposure to the electron beam is done in Raith Eline

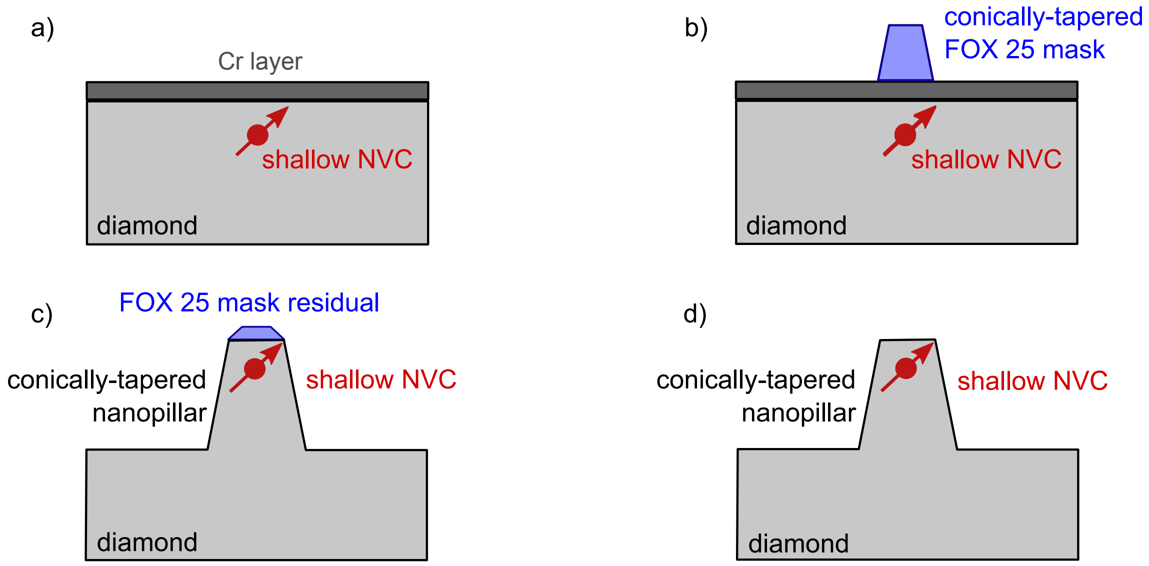

Figure 3.11.: Realization scheme of the conically-tapered nanopillar geometry is shown. The thin diamond film substrate hosting shallow-implanted NVCs and the adhesion Cr layer (a) will be addressed in the next steps for the generation of the FOX 25 mask (b) by means of e-beam lithography technique. The RIE-ICP etching method is applied (c) to transfer the shape of the mask to the diamond substrate. After the etching step, the diamond sample is cleaned (d) in buffered HF, Cr etching, and triacid mixture solutions.

apparatus with 20 kV of acceleration voltage and 10 μm aperture (current $\sim$ 40 pA) where the exposure dose is 3000-4000 μC/cm^2. It should be highlighted that the shape of the FOX 25 mask plays the key role in forming the final conically-tapered geometry of the nanopillar. In fact by overexposing the FOX 25 resist, the amount of backward-scattered electrons from the diamond substrate to the resist increases. Therefore, by increasing the exposure of the lower part of the resist to electrons in comparison to the upper layers, the bottom diameter of the resist (etching mask) becomes larger than its top one after the developing process. It should be mentioned that bottom diameters larger than 900 nm do not deliver good etching resistance performance. After the electron exposure and in prior to developing the exposed resist, the anti-charging Cr layer is removed in Cr etching solution. The developing process is performed for 8 minutes in MF-322 developer solution. As the next step of the fabrication, RIE-ICP process is performed in Oxford PlasmaPro NGP80 machine to etch the area of the diamond substrate which is not covered by the FOX 25 mask. Oxygen plasma (30 sccm of flow rate) divided in three steps with duration of each 2 minutes using constant RIE power of 100 W under 10 mTorr chamber pressure is applied. The ICP power is adjusted at 600 W - 400 W - 600 W values for the consequent etching steps to control the corrosion rate of the mask and thus the final nanopillar shape. Between each consequent oxygen etching step, 7 seconds of O_2/CF_4 (30 sccm O_2 / 2 sccm CF_4) with the RIE and ICP powers of 30 W and

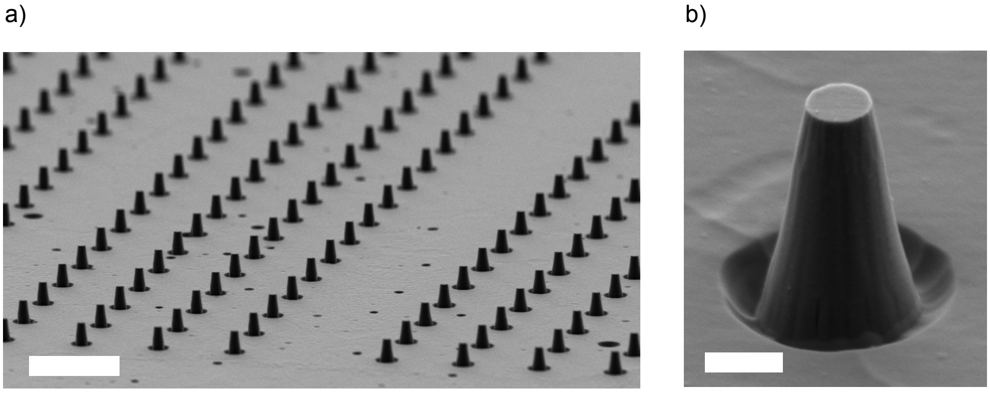

Figure 3.12.: SEM image of the conically-tapered nanopillar geometry is shown. a) An array of tapered nanopillars (scale bar = 5 μm) is depicted. (b) SEM image of a conically-tapered diamond nanopillar with the approximate bottom and top diameter of 900 nm and 400 nm, respectively, is shown where its height is $\approx$ 1.2 μm (scale bar = 500 nm).

150 W, respectively, is used to remove the residual FOX 25 particles located on the etched surface of diamond, which act as the secondary etch mask against the oxygen plasma and thus lead to the roughness of the etched surface [81]. This short step is observed to be enough to avoid formation of diamond nanograss. After the whole etching process, approximately 200 nm of the FOX 25 resist is still remained. However, to avoid any harmful effect of the plasma to the shallow-implanted NVCs, e.g. to deteriorate their coherence times (see the next section), the etching process is stopped after $\sim$ 6-7 minutes. The whole etching process results in an etching rate of $\approx$ 180 nm/min, thus etching selectivity of $\sim$ 6. Next, the residual of the etching mask is removed by immersing the substrate into buffered HF solution for 10 minutes. Afterward, the sample is cleaned in Cr etching solution and finally triacid solution. The latter is applied to guarantee the oxygen termination of the surface and to remove any residual of the fluorine which possibly got introduced to the surface via the HF solution. The explained fabrication process is schematically presented in Figure 3.11. As this fabrication is based on statistics, multiple (thousands) of those nanopillar geometries are made onto the diamond thin film substrate. An SEM image of those structures can be seen in Figure 3.12-(a), where a single conically-tapered nanopillar geometry with approximate bottom and top diameter of 900 nm and 400 nm, respectively, and height of $\approx$ 1.2 μm is depicted in Figure 3.12-(b).

3.4. Experimental characterization

3.4.1. Optical benchmark measurements

In this section, the optical and spin interface of the developed nanopillar-NVC hybrid system, is characterized. As the first step, the optical properties of these waveguides are investigated by a home-built confocal microscope running under ambient conditions using excitation light of 532 nm wavelength employing longpass fluorescence filter (650 nm - LP) and an air objective lens with $NA = 0.95$ located on the nonstructured side of the thin diamond film substrate. Figure 3.13-(a) shows the confocal image of the NVCs generated by the ion implantation energy of 2.5 keV, located on the apex of the conically-tapered nanopillars with 400 nm of top and 900 nm of bottom diameter. This image illustrates the relatively low optical background of the achieved geometry. For instance, even at $\sim$ 700 μW of incident laser power (measured before the objective lens), an empty tapered nanopillar has only $\sim$ 15% of the photon count rate of a tapered nanopillar hosting a single NVC.

To assure the number of NVCs in each nanopillar and also acquire information about the signal-to-noise ratio of the collected photons from each nanopillar (information about count rate originated from pure NVC and background), second-order autocorrelation measurements ($\mathrm{g}^{(2)}$) are performed. These measurements are carried out via detecting the fluorescence photons emitted by the NVCs in such waveguides by means of two avalanche photodiodes (APDs) in the Hanbury Brown and Twiss (HBT) configuration (Figure 3.13-(b)). As illustrated in Eq. (3.12) and Eq. (3.13), using the $\mathrm{g}^{(2)}$ function value at the delay time τ equal to zero, one can estimate the number of emitters, in addition to checking the signal-to-noise ratio associated with the fluorescence signal. For instance, for the inspected nanopillar-NVC hybrid system in Figure 3.13-(c), based on Eq. (3.13), background signal of only $\approx$ 15% of the pure NVC fluorescence signal is monitored. In the investigated sample, approximately 30% of the conically-tapered nanopillars show a second-order autocorrelation signal ($g^{(2)}(\tau = 0) < 0.5$) indicating single photon emission (Figure 3.13-(c) and -(d)) with excellent photostability. Further optimization in the dose of the nitrogen implantation can improve this yield.

Based on the discussion at the beginning of this chapter, the amount of photons emitted by the NVC inside the nanopillar geometry depends also on the spontaneous emission rate of the NVC itself. To check this, the excited-state lifetime measurements are performed using 10 ps pulses of 532 nm wavelength laser together with time-correlated single photon counting electronics probing several single NVCs (confirmed by the $\mathrm{g}^{(2)}$ measurements) inside the nanopillar geometry. For comparison, measurements are taken for shallow NVCs inside the presented hybrid platform as well as under the nonstructured (bare) diamond surface. Common to most of the cases, a double exponential decay behavior is observed. By integration, the

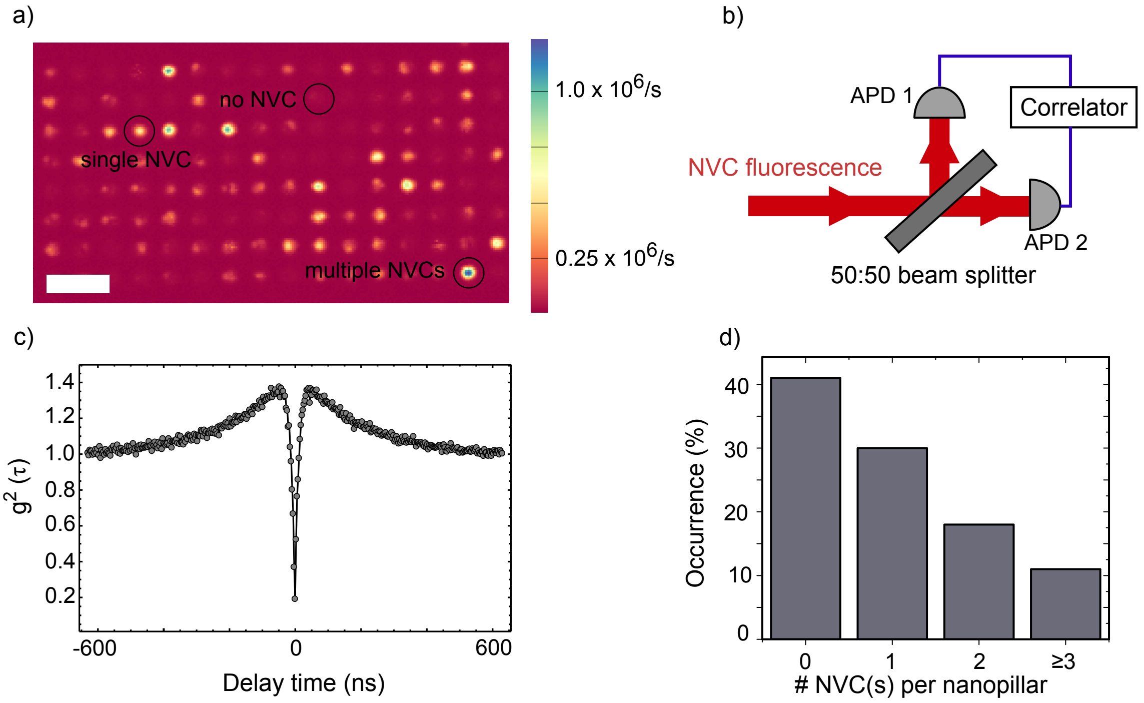

Figure 3.13.: (a) Confocal image of an array of the hybrid nanopillar-NVC photonic structure is shown. The relatively low background signal in the etched area and also the tapered nanopillars lacking NVCs is clear. For the sake of clarity, example of nanopillars with no, single, and multiple NVCs are marked. Scale bar represents 10 μm. Sketch of the HBT setup (b) to perform the second-order fluorescence autocorrelation ($g^{(2)}$) measurements (c) is depicted. As can be seen in (c), the $g^{(2)}(\tau=0) \approx 0.18$ indicates a clean (see the main text) fluorescence signal proving a single-photon emission behavior. (d) Number of NVCs inside the nanopillar geometry can be estimated using the output of autocorrelation measurements. As demonstrated, almost 30% of the hybrid systems possess single NVC.

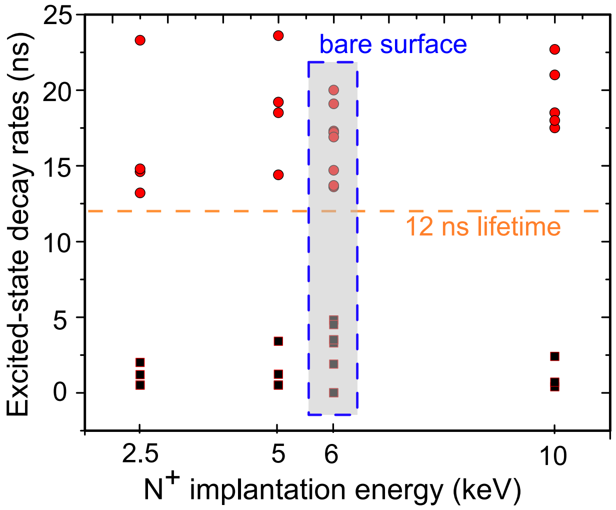

Figure 3.14.: Decay rates of the excited state emission of NVCs located few nanometers below the diamond surface inside and outside of the nanopillar geometry vs. the implantation energy are shown. As can be seen in most of the cases, the decay shows two-component exponential decay (nonzero fast decay shown in black squares) while the slow-decay (shown in red circles) mostly has values longer than the well-known bulk value of 12 ns (shown with a dashed orange line). To compare the effect of the presence of the nanopillar geometry and NVCs' depth (equivalently their implantation energy), NVCs resulting from different implantation energies inside and outside of the nanopillar geometry (inside the gray-filled rectangle) are investigated. The plotted results in this figure do not conclude any systematic effect of the nanopillar waveguide on the excited-state lifetime of the embedded shallow NVCs.

faster decay component shows less than 5% of signal contribution in comparison to the slower decay component. As depicted in Figure 3.14, the fast decay rate is observed to be ≤ 5 ns consistently. Since these decay rates are close to the time resolution of the setup, they might be in fact even shorter. This contribution can be attributed to an unbleachable background signal or partially quenched NVCs in the vicinity of the NVC under investigation. In contrast, the longer decay rate which resamples the excited-state lifetime, is revealed to always exceed 12 ns, as the well-known value for the excited-state lifetime of NVCs located few microns below the diamond surface [71] (shown with dashed line). In the case of NVCs located $\sim$ 1 μm under the apex of the diamond nanopillar [34], approximately 30% of change in their excited-state lifetime was expected in comparison to those under the diamond nonstructured surface. This change was reported to be due to interference which occurs between downward emitted photons by the NVC and the photons which are reflected from the top facet of the nanopillar. In the case of shallow NVCs under the conically-tapered nanopillar surface, the monitored increase on the excited-state lifetime occurs mostly because of a reduction of the electric LDOS (see Eqs. (3.1) and (3.2)) due to the close vicinity to the diamond-air interface

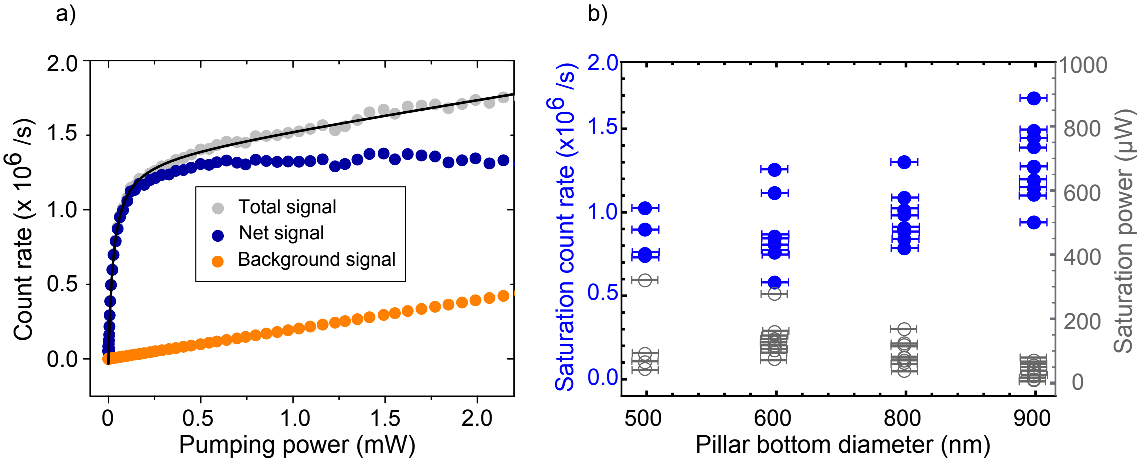

Figure 3.15.: (a) Saturation plot of an NVC few nanometers below the facet of the presented conically-tapered nanopillar geometry is shown. The total, net, and background signals are shown by gray-dotted, blue-dotted, and orange-dotted curves, where the black line shows the fit based on the model given in Eq. (3.5). (b) Saturation fluorescence rate and power of NVCs inside the conically-tapered nanopillar geometry with the height of 1.2 μm and top diameter of 400 nm, where the bottom diameter is varied. As can be seen, the larger the bottom diameter the higher (lower) will be the saturation count rate (power). This indeed proves that the presented structure is a broadband waveguide for both the excitation and emission of the embedded NVCs. The horizontal error bars of 20 nm show the tolerance in the bottom diameter due to the precision of the fabrication process and also the SEM imaging accuracy.

[82]. This statement is confirmed since the same observation is also registered for the shallow NVCs under the nonstructured surface of diamond (see Figure 3.14). Therefore, it can be concluded that no systematic change in the spontaneous emission rate of the NVCs is made by positioning them inside the conically-tapered nanopillar geometry.

After preselecting the hybrid systems possessing a single NVC inside, and also checking their lifetimes, the optical characterization of these nanostructures is continued by checking their fluorescence saturation behavior. These measurements are done again by a home-built confocal microscope running under ambient conditions (see Appendix). The collected phonon sideband is spatially filtered by a 50 μm pinhole. To decide on the right size of the pinhole employed in the confocal setup, the beam collected back from the conically-tapered nanopillars by the microscope objective lens is focused onto the chip of a cooled-CCD camera (Cascade 512B). The FWHM of the Airy curve is observed to be ≈ 2 pixels large, where each pixel is 16 μm. Therefore, a 50 μm pinhole is seen to be suitable since it collects all the signal photons while it rejects the major part of the background contribution. To investigate the saturation behavior of these structures, the number of detected photons as a function of the incident laser power (measured behind the objective lens) is measured. To obtain the net NVC fluorescence and background count rates from the total detected signal of an NVC inside a nanostructure, three methods can be used:

i) to measure the background signal from a nanopillar containing no NVC, which can be found in the confocal scan (Figure 3.13-(a)). This method is not generally valid, however applies truly to those nanostructures which show a low background signal in comparison to the net NVC fluorescence signal.

ii) the background signal can be fitted from the total detected count rate using the Eq. (3.5) by considering an additional term in which the background signal is linear to the pumping power.

iii) the $g^{(2)}(\tau = 0)$ function (see Eq. (3.13)) at different pumping powers can be measured which gives the ratio between the net and background signal.

An example of the saturation curve can be seen in Figure 3.15-(a), where a single NVC resulted from 2.5 keV of N^+ implantation energy in a nanopillar with approximate height, bottom diameter, and top diameter of 1.2 μm, 900 nm, and 400 nm, respectively, is inspected. In this figure, the gray-dotted curve shows the total detected counts, where by fitting (black line) the data using the above-mentioned ii) method, the background signal (orange-dotted) can be subtracted which yields in the net NVC fluorescence signal (blue-dotted plot). The obtained NVC saturation fluorescence count rate and power are $1.36 \pm 0.01 \times 10^6$ /s and 27 ± 1 μW, respectively. In comparison to the shallow NVCs under the bare diamond surface, an enhancement (reduction) in the saturation count rate (power) of the NVCs inside the presented hybrid system by more than 1 order of magnitude is achieved.

Another important point regarding the superiority of this hybrid system is the low background signal. The above-mentioned signal-to-noise ratio recorded from the demonstrated structure can be rephrased now based on the normalized photon shot noise defined by $\sqrt{F_{\text{total}}}/F_{\text{net}}$ where F_{total} and F_{net} are the total and net NVC detected fluorescence count rates, respectively. For instance, for the same NVC-nanopillar hybrid system, at the incident power of 1 mW, this quantity is $\approx 9 \times 10^{-4}$ $\text{Hz}^{-1/2}$. This achieved value is at least one order of magnitude smaller than the case of shallow NVCs under the nonstructured diamond surface.

To verify the FEM simulations leading to the optimized geometry of the conically-tapered nanopillar, the saturation power and count rate of several single NVCs generated from 2.5 keV of N^+ implantation energy in the mentioned geometry with the top diameter fixed at $\approx$ 400 nm and different bottom diameters are measured. As shown in Figure 3.15-(b), the geometry with larger bottom diameter ($\approx$ 900 nm) delivers higher (lower) saturation count rate (power) indicating a more efficient waveguide for the excitation and emission of the NVCs in comparison to the ones with smaller bottom diameters. As depicted in this figure, the nanopillar geometry with 900 nm of bottom diameter gives mean saturation photon count rates of about 1.5×10^6 /s with the maximum up to $\approx 1.7 \times 10^6$ /s. As this hybrid system shows

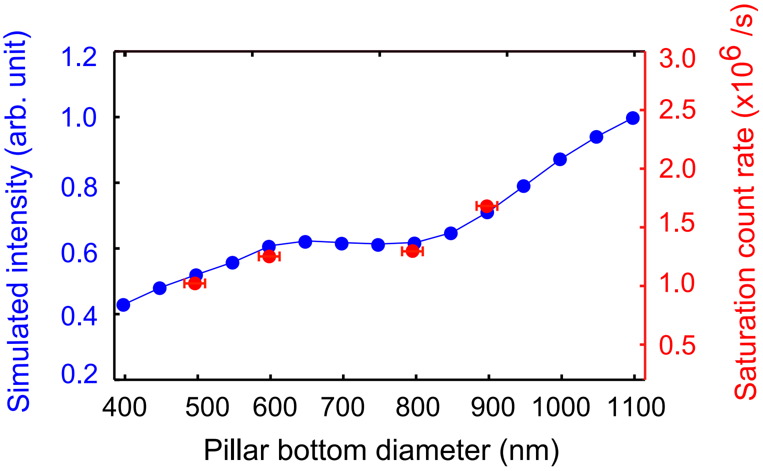

Figure 3.16.: Simulated and measured detected saturation intensities of the NVCs embedded in the conically-tapered nanopillar geometry are compared. The red dots show the measured data (error bar of 20 nm in bottom radius) for four different bottom diameters of the nanopillar structure, where the blue curve shows the simulated collected electric field intensity. As can be seen, consistent match exists between these two curves, proving the validity of the FEM simulations with respect to the experimental achievements.

no effective influence on the excited-state lifetime of the embedded NVCs, while it features a huge enhancement in the number of the collected photons, it is concluded that the photon collection efficiency of the NVCs due to the presented hybrid engineered nanostructure is augmented more than one order of magnitude in comparison to the nonstructured diamond host.

The maximum value of the fluorescence saturation count rate vs. bottom diameter of the tapered nanopillar structure (Figure 3.15-(b)) is mostly attributed to the case in which the NVC is located close to the axis of the nanopillar. Given these maximum values of the fluorescence saturation count rate for the given bottom diameters, one can compare the experimental and FEM simulation results. As illustrated in Figure 3.16, their behavior manifests a consistent match for four different geometries of the conically-tapered nanopillar. This is of great importance, since it supports the reliability of all the assumptions made through the FEM simulations.

3.4.2. Spin-dephasing times measurements

It is already discussed that the magnetic field sensitivity of an NVC is limited by its spin-dephasing times. For the NVC - conically-tapered nanopillar hybrid geometry, an order of magnitude enhancement in the photon collection efficiency is achieved. In this subsection, the dephasing time of the embedded NVCs is probed (see chapter 1). T_2 dephasing times are

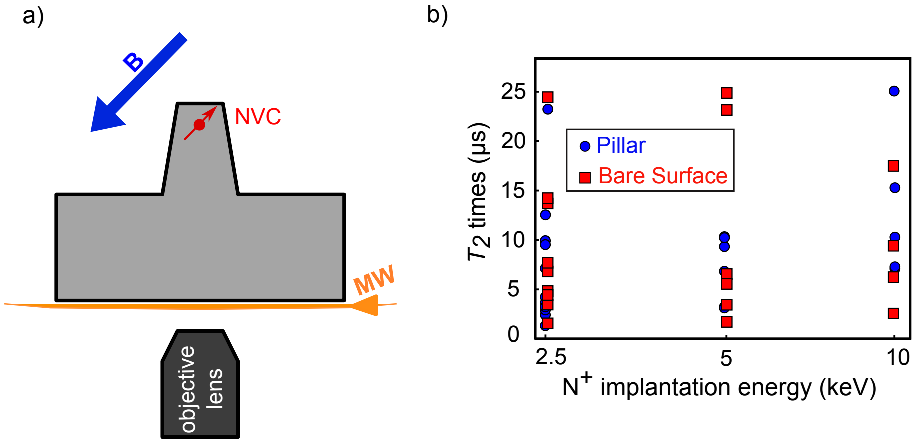

Figure 3.17.: (a) Scheme of the NVC-tapered nanopillar hybrid system in spin-dephasing time measurements; magnetic field of 100-150 G is aligned to the NVC axis, where MW pulses are applied to the NVC via a copper wire spanned over the nonstructured side of the diamond substrate. (b) Plot of T_2 times of NVCs inside the hybrid system and also under the bare (nonstructured) diamond surface vs. different N$^+$ implantation energies is given. As can be seen, similar values from two different cases are obtained. This notes the preservation of the spin properties of shallow NVCs inside the nanopillars due to the designed geometry and applied fabrication process.

measured by means of optically detected Hahn echo scheme [24] probing the coherence of the ground state $m_s = |0\rangle$ to $m_s = |-1\rangle$ of the NVC electronic spin under ambient conditions. By means of a permanent magnet, magnetic field of 100-150 G is aligned parallel to the NVC axis under investigation. In this configuration, the microwave pulses are applied through a 20 μm-diameter copper wire spanned over the nonstructured surface of the diamond substrate. In this way (Figure 3.17-(a)), while neither undesired optical effect (background), nor mechanical force is applied to the nanopillars, the power of the applied microwave pulses seems to be sufficient (π pulse $\sim$ 50 ns).

The T_2 times of the NVCs resulted from 2.5, 5, and 10 keV energies of ion implantation within the nanopillar structure are obtained close to the values of those under the nonstructured diamond surface (Figure 3.17-(b)). This preservation of the shallow NVCs' dephasing times, even for those generated by 2.5 keV implantation energy which should yield to the shallowest NVCs in comparison to others (based on simulation, [80]), can be due to the relatively large top diameter of the tapered nanopillars ($\approx$ 400 nm). This relatively large area prevents the negative effects of the fabrication process, e.g. the etching steps, on the coherence times of the NVC probes.

As a step further, dynamical decoupling scheme to enhance the T_2 time of the NVCs inside the nanopillar structures is performed. As an example, Carr Purcell Meiboom Gill (CPMG)-N pulse sequence [83, 84, 85] (N is the number of π pulses, see Figure 3.18-(a)) is applied to an

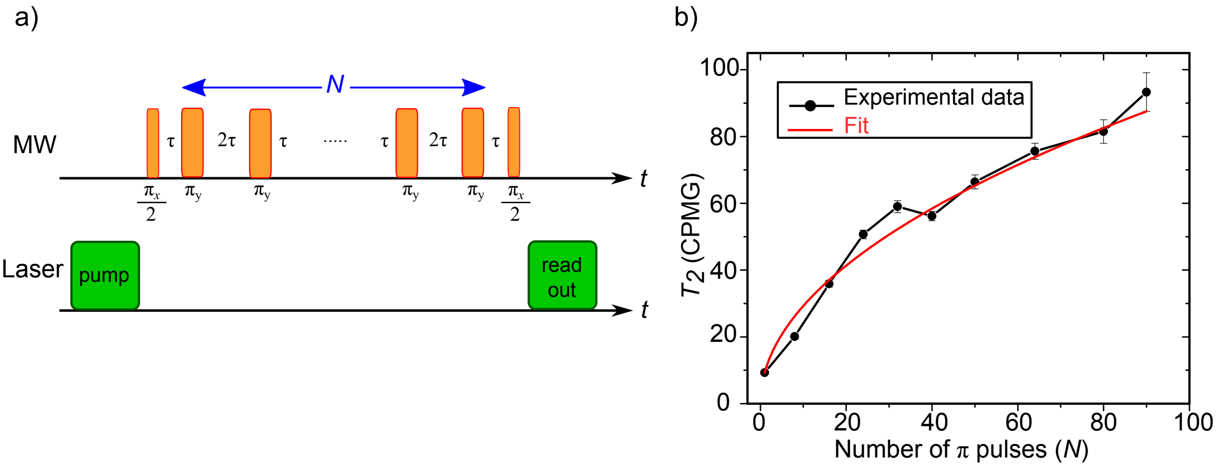

Figure 3.18.: a) Scheme of the CPMG pulse sequence is depicted. b) The measured T_2 (CPMG-N) vs. N for an NVC generated from 2.5 keV of implantation energy is depicted (applied magnetic field of 117 G). By fitting this data to T_2 (CPMG) = $N^\gamma \cdot T_2$ (Hahn echo), γ exponent of ≈ 0.50 is derived.

NVC generated by 2.5 keV of implantation energy, under 117 G of applied magnetic field. It is observed that, by applying $N = 90$ π pulses, the T_2 time of this single NVC can be prolonged from ≈ 9.3 μs to ≈ 94 μs. It is known that the relation between the measured T_2 (Hahn echo) (or equivalently $N = 1$) and T_2 (CPMG-N) is given by T_2 (CPMG) = $N^\gamma \cdot T_2$ (Hahn echo), where for an NVC with a simple Lorentzian spin bath $\gamma = 2/3$ [83, 84]. For this NVC, $\gamma = 0.50 \pm 0.01$ is obtained. This change in the exponent can be due to different frequency and origin of the noise bath at the vicinity of the NVC, mostly due to its vicinity to the diamond surface [84].

In summary, based on the presented statistical study, it can be concluded that the developed conically-tapered nanopillar geometry preserves the spin properties of the embedded shallow NVCs. By further improvements of the diamond surface to reduce the surface magnetic and electric noises [86, 25], the T_2 dephasing times of the NVCs embedded into the nanopillar geometry might be even further augmented. In addition, by employing alternative methods to generate the shallow NVCs such as using δ-doped diamond surface and helium irradiation technique [26], the spin dephasing times can be approximately five-fold enhanced.

In recent years, magnetometry at low temperatures (LT) has emerged as a new field in NVC-based metrology techniques [86, 87, 88]. As in room temperature NVC-based magnetometry, in addition to the T_2 spin-dephasing time, T_1 spin-lattice relaxation time [89, 90] also plays an important role. At LT, the T_2 coherence time of ensemble of NVCs was shown to be enhanced using dynamical decoupling schemes approaching $T_1/2$ [90]. Importantly, T_1 relaxation times of ensemble of NVCs at LT were reported to exceed 1 min [91]. It should be mentioned that measuring the long ($\geq$ ms) T_1 times at the single NVC level under the nonstructured diamond

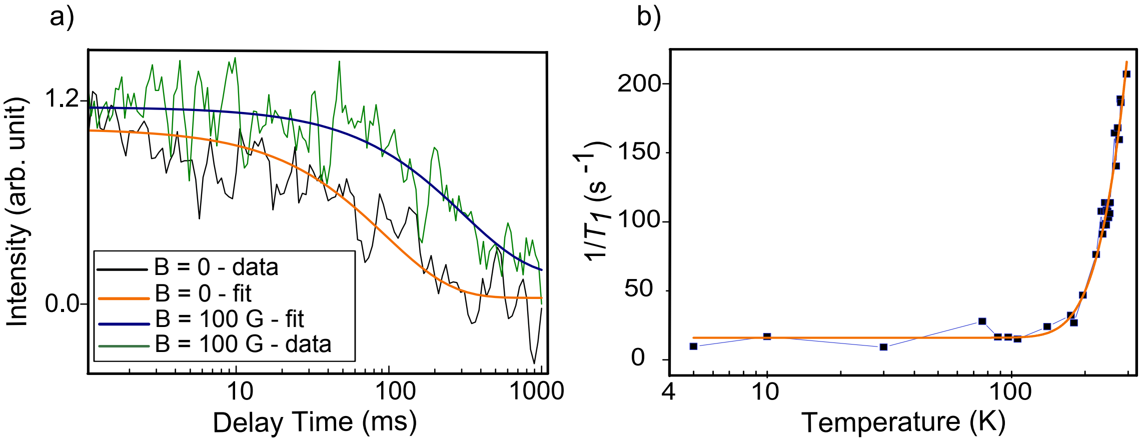

Figure 3.19.: (a) T_1 dephasing curves of a single shallow NVC at the extremity of the conically-tapered nanopillar at $T \approx 5$K in the presence (green color) and absence (black color) of 100 G aligned magnetic field are depicted. The blue and orange exponential fits give approximate T_1 values of 300 ms and 100 ms, respectively. (b) The inverse T_1 values of the investigated NVC in the absence of applied magnetic field is shown vs. temperature. As it is demonstrated, going from room temperature down to $\approx$ 5 K, the T_1 relaxation time increases from $\sim$ 5 ms to $\sim$ 100 ms. This dependency is fitted by the model given in Eq. (3.19).

surface can take relatively long. At LT due to technical challenges such as degradation of the collection tools, e.g. the microscope objective lens, this takes even longer in comparison to room temperature. Here as a remedy, by benefiting from high collection efficiency of the presented nanopillar structure, T_1 time of a shallow NVC embedded in the presented hybrid structure, at different temperatures and magnetic fields is feasible to measure. Applying the same pulse scheme used in [91] to a single NVC within the presented hybrid platform at $\approx$ 5 K, T_1 value of 95.3±9.94 ms in the absence of the applied magnetic field is measured. In comparison to the previously-reported values from ensembles of NVCs [91], this investigated NVC shows a shorter T_1 time. This can be caused by magnetic noises and other defects at the diamond surface. By applying magnetic field of $\approx$ 100 G aligned to the axis of the NVC, the T_1 time is extended by more than three times approaching 306.8±49.8 ms, which can be caused by decoupling from S = 1/2 spin defects such as P1 centers (see Figure 3.19-(a)) [91].

Tracing the T_1 spin-lattice relaxation times of shallow NVCs vs. temperature can give information about the phononic environment of the NVCs [91]. To this aim, the T_1 relaxation time of the previously-investigated NVC versus different temperatures within the range of room temperature to LT in the absence of applied magnetic field is measured. As shown in Figure 3.19-(b), as the temperature is decreased from room temperature down to $\approx$ 5 K, the T_1 relaxation time increases from $\sim$ 5 ms to $\sim$ 100 ms. The temperature- (T) dependency of the T_1 times can be fitted to a model which consists of a sample-dependent term (A) and a two-phonon Orbach process term [91]:

$$\frac{1}{T_1} = A + \frac{B}{exp(\frac{\Delta}{k_B T}) - 1}. \tag{3.19}$$

In this equation, A and B are fitting parameters, where Δ and k_B are vibrational energy and the Boltzmann's constant. Two visible differences can be seen between the results about ensemble of NVCs [91] and the given results about the probed single shallow NVC. (i) In comparison to the ensemble results, the Orbach process is observed to be the only temperature-dependent term, while the two-phonon Raman process could be negligible [91, 92]. (ii) By fitting the data presented in Figure 3.19-(b) to Eq. (3.19), the vibration energy of Δ = 92.92±6.40 meV is obtained, whereas for the case of NVC ensemble, Δ is $\sim$ 70 meV. This deviation can be related to the modified phonon density of states for this shallow NVC at the extremity of the tapered nanopillar [93], or the presence of paramagnetic noises at its surrounding. Both effects are nevertheless originated from the surrounding environment of the shallowly-implanted NVC and its close vicinity to the diamond surface.

3.5. Summary and outlook

In conclusion, a novel hybrid photonic nanostructure for hosting shallow NVCs is developed. This hybrid arrangement consists of conically-tapered diamond nanopillar structure with the embedded NVCs which are located few nanometers under its apex. A prominent photon count rate of $\approx 1.7 \times 10^6$ /s is achieved from a single shallow NVC which brings a new area for NVCs in monolithic bulk diamond structures. This structure gains approximately 13-fold enhancement in the collected number of photons emitted by the single NVC, in comparison to those under the nonstructured diamond surface. This enhancement is achieved while no change is observed in the excited-state lifetime of the NVCs inside the nanopillar structure, compared to those under the nonstructured diamond surface. Consequently, it is concluded that the achieved augmentation is attributed to the enhancement in the photon collection efficiency and not any Purcell enhancement. With respect to the FEM simulations, only $\sim$ 50 % of the emitted electric field intensity is collected by the objective lens. This points to the possibility of further enhancement of the achieved photon count rate, e.g. by steering more emitted photons to the objective lens via applying coating material on the pillar geometry, etc.

In addition, no degradation of the NVCs' T_2 dephasing times is observed due to the nanopillar geometry and also the utilized fabrication process. Furthermore, as an enabling platform for LT magnetometry-based measurements, the T_1 relaxation time of a single NVC inside this nanopillar structure at LT is measured, revealed to exceed 300 ms. Benefiting from its un-

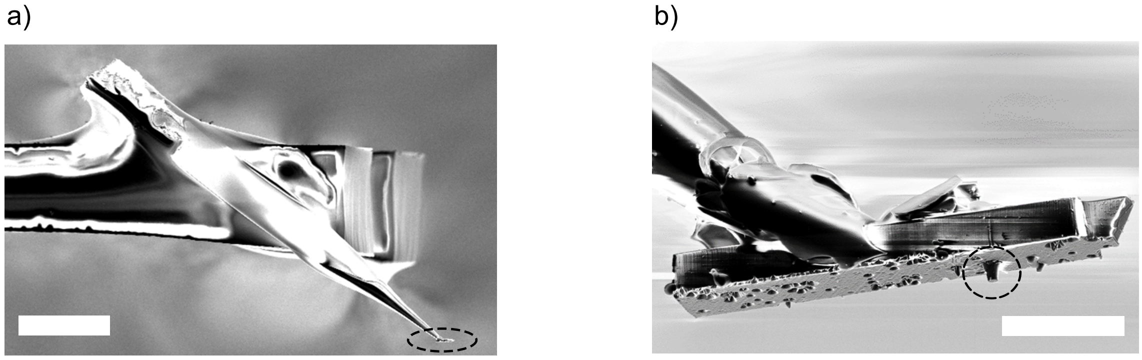

Figure 3.20.: Diamond scanning probe including a tapered nanopillar geometry is shown. (a) A tapered nanopillar directly fabricated onto a diamond cantilever (marked with the black oval) is attached to a quartz fiber which is then glued into an AFM tuning fork. (b) The marked area in image (a) is magnified here. As shown in the black circle, the nanopillar geometry is a key element of this diamond scanning probe. Scale bars in figures (a) and (b) depicts 100 μm and 5 μm, respectively. The demonstrated figures (a) and (b) are courtesy of Anurag Kanase and Amit Finkler.

precedented number of collected photons, further investigations on the phononic environment of the shallow NVCs in comparison to the bulk ones is also accomplished.

This hybrid architecture can be lent into several improvements and further applications in NVC-based magnetometry field thanks to its one-order-of-magnitude enhanced photon collection efficiency. Among those, one can point to enhanced signal-to-noise ratio of magnetic field sensing, and some perspective applications such as all-diamond scanning probes and biological studies involving cells, accordingly:

• As discussed before, magnetic field sensitivity by means of NVCs is scaled as $\frac{1}{\sqrt{F}}$ with their photon count rate F. Therefore, the one order of magnitude enhancement in the count rate of NVCs by means of the nanopillar structure introduces an approximate three-fold enhancement in the sensitivity. By engaging single-shot readout technique to reduce the measurements' acquisition time, in addition to using the nanopillar structure, a tremendous enhancement in the signal-to-noise ratio is achieved [94]. Combining these two benefits, it is shown that e.g. an enhancement factor of ≈ 20 in the signal-to-noise ratio of T_1 measurement is acquired, in comparison to the non-pillar sample with standard readout.

• In addition to the notable sensitivity of the NVCs as magnetometers, they can be further integrated into all-diamond scanning probes which yields simultaneously in high sensitivity and nanoscale spatial resolution [77]. To that aim, the tapered nanopillar structure with incorporated shallow NVCs can be made monolithically onto the diamond cantilevers, which enables the controlled scanning of the NVC probe over the sample area under investigation. As can be seen in Figure 3.20, the developed conically-tapered nanopillar structure is made onto a diamond cantilever with the thickness of ~ 2 μm, which is glued to a quartz tube and then onto an AFM tuning fork. This complete scanning probe tool can be used in high-spatial-resolution magnetic imaging [95].

- The presented platform can be utilized in biological applications in which NVCs are used as nanosensors for the physical/chemical properties of cells that are directly cultured on top of the diamond nanopillar arrays [96]. In this way, the achieved one order of magnitude decrease in the saturation power of the NVCs inside the nanopillar geometry (in comparison to those under the diamond nonstructured surface) can induce much less side effects such as heating inside the cells, then render more reliable measurements output.

4. Hybrid Diamond-NVC Mechanical Structures

The demonstrated results in this chapter are mainly presented and published in [97], S. Ali Momenzadeh *et al.* Phys. Rev. Applied, **6**, 024026 (2016).

Coupling mechanical degrees of freedom to various quantum systems has attracted huge interest recently [98, 99, 45]. In this regard, hybrid architectures based on mechanical structures and well-controlled quantum objects have been developed. The quantum objects utilized in these devices range from ultracold atoms [100] to superconducting circuits [101], quantum dots [102], and solid-state spin defects [45], whereas the mechanical systems are mostly free-standing beams or thin membranes, in different sizes and geometries [98, 99]. In this chapter, hybrid mechanical diamond-NVC structures will be discussed, which in particular thin circular diamond membranes and diamond microcantilevers will be presented. In the first section, theoretical backgrounds consisting of a brief review about mechanical degrees of freedom such as stress and strain, classical and quantum harmonic mechanical oscillators, mechanical properties of diamond, and interaction of the NVCs with different mechanical degrees of freedom such as vibration and stress, will be given. In the next section, thin circular diamond membranes with embedded NVCs will be presented. Design and fabrication of this hybrid architecture will be shown, which will be continued by characterizing the system by employing NVCs as nanoscale sensors for the mechanical degrees of freedom of the membrane, e.g. its deflection, radial stress, residual stress, etc. This is accomplished via the readout of the optical and spin interfaces of NVCs as embedded nanosensors inside the membrane. So far, interaction of NVC with its local mechanical environment is studied. In the next section, an array of diamond microcantilevers, and specifically, double mechanically-coupled diamond microcantilevers will be discussed. In this line, mechanically-coupled microcantilevers will be proposed as quantum bus to couple two distant NVCs. The relevant realization and characterization of this platform will be given afterward.

4.1. Theoretical background

4.1.1. Mechanical degrees of freedom

At the first step, one can consider a rigid bar with length l and cross-section A. Given an applied uniform external force $\mathbf{F}$ acting perpendicular to the cross-section of this bar, an equivalent stress given by $\sigma = F/A$ is applied to it. This stress yields to a relative length difference Δl of this bar. The relative change in the length of this bar is explained by strain given by ε=$\Delta l/l$. The relation between the stress applied to the bar and the resulting strain is given by Hooke's law [60, 103]:

$$\sigma = E \cdot \varepsilon, \tag{4.1}$$

where E is the material-dependent Young's modulus of the bar.

In 3D material it is more intricate than the described formula. For the sake of simplification, hereinafter only isotropic elastic material will be considered. Isotropic materials possess mechanical properties which are independent of any direction in space. In matrix form within the Cartesian coordinate frame, assuming a constant temperature of the rigid body, the relation between stress and strain components are given by [60, 103]:

$$\begin{pmatrix} \sigma_{xx} \\ \sigma_{yy} \\ \sigma_{zz} \\ \sigma_{yz} \\ \sigma_{xz} \\ \sigma_{xy} \end{pmatrix} = \frac{E}{(1+\nu)(1-2\nu)} \begin{pmatrix} 1-\nu & \nu & \nu & 0 & 0 & 0 \\ \nu & 1-\nu & \nu & 0 & 0 & 0 \\ \nu & \nu & 1-\nu & 0 & 0 & 0 \\ 0 & 0 & 0 & (1-2\nu) & 0 & 0 \\ 0 & 0 & 0 & 0 & (1-2\nu) & 0 \\ 0 & 0 & 0 & 0 & 0 & (1-2\nu) \end{pmatrix} \begin{pmatrix} \varepsilon_{xx} \\ \varepsilon_{yy} \\ \varepsilon_{zz} \\ \varepsilon_{yz} \\ \varepsilon_{xz} \\ \varepsilon_{xy} \end{pmatrix}, \tag{4.2}$$

where ν is the Poisson's ratio of the material. To make the double index notation clear, for instance, the strain components as function of displacement $\mathbf{u}$ are thus defined as [60]:

$$\varepsilon_{xx} = \frac{\partial u_x}{\partial x}, \varepsilon_{yy} = \frac{\partial u_y}{\partial y}, \varepsilon_{zz} = \frac{\partial u_z}{\partial z}, \varepsilon_{xy} = \frac{\partial u_x}{\partial y} + \frac{\partial u_y}{\partial x}, \varepsilon_{xz} = \frac{\partial u_x}{\partial z} + \frac{\partial u_z}{\partial x}, \varepsilon_{yz} = \frac{\partial u_y}{\partial z} + \frac{\partial u_z}{\partial y} \tag{4.3}$$

4.1.2. Classical and quantum mechanical oscillators

In classical mechanics, following Newton's second law, a damped harmonic oscillator in the absence of any external force with undamped angular frequency of ω is explained by the following equation of motion [60]:

$$\ddot{x} + 2\zeta\omega\dot{x} + \omega^2 x = 0, \tag{4.4}$$

where x is the position of the oscillator. ζ is a dimensionless measure called damping ratio, which determines the damping behavior of the system. For such a system, an important factor is the dimensionless quality factor (Q-factor) that is defined as the ratio of the energy stored in the oscillator and the energy which is lost per each cycle of oscillation. Clearly, a system with higher Q-factor can relatively save the mechanical energy for a longer time. The Q-factor of the oscillator is written equal to $1/2\xi$. On the other hand, this factor describes how narrow the oscillator's resonance, i.e. its bandwidth is, relative to its resonance frequency. Given a mechanical oscillator with angular resonance frequency ω and corresponding bandwidth $\Delta\omega$, the Q-factor is equal to $\omega/\Delta\omega$. The product of the resonance frequency and the Q-factor, i.e. $\omega \cdot Q$, of a mechanical oscillator is an important figure of merit. For instance, the minimum detectable force by a mechanical oscillator is scaled with $(\omega \cdot Q)^{-\frac{1}{2}}$ [104]. The maximum reported value of $\omega \cdot Q$ is 10^{14} Hz to date [105].

Within quantum mechanics, a harmonic oscillator with mass m and the corresponding potential of $\frac{m\omega^2}{2}x^2$, follows the Hamiltonian $H = \hbar\omega(N + 1/2)$, where the occupation number operator is given by $N = a^\dagger a$. The two given operators a and $a^\dagger$ are the bosonic annihilation and creation operators, respectively, which are given by:

$$a := \frac{1}{\sqrt{2m\omega\hbar}}\left(m\omega x + ip\right),\; a^\dagger := \frac{1}{\sqrt{2m\omega\hbar}}\left(m\omega x - ip\right), \tag{4.5}$$

where p is the momentum operator of the oscillator and $\hbar$ is the Planck's constant divided by 2π. The energy eigenvalues for such a system follow $\hbar\omega(n + \frac{1}{2})$, in which n can be seen as the number of phonons. The average number of phonons obeying Bose-Einstein distribution at a given temperature T can be written as:

$$\langle n \rangle = \frac{1}{exp\left(\frac{\hbar\omega}{k_B T}\right) - 1}, \tag{4.6}$$

where k_B is the Boltzmann's constant [106]. For example, a mechanical oscillator with resonance frequency of $\omega = 1$ MHz has $\sim 10^7$ phonons at room temperature ($T \approx 300$ K).

A mechanical resonator system in quantum mechanics possesses a zero-point energy, i.e. a non-zero ground-state energy, equal to $\frac{\hbar\omega}{2}$, which is in contrast to its analogous in classical mechanics. Equivalent to the concept of zero-point energy another important parameter can be derived, named as zero-point fluctuation (ZPF). For a quantum harmonic oscillator, by considering the lower limit of the Heisenberg's uncertainty principle, the zero-point fluctuation parameter is given as [107, 108]:

$$x_{\text{ZPF}} = \sqrt{\langle x^2 \rangle} = \sqrt{\frac{\hbar}{2m_{eff}\omega}}, \tag{4.7}$$

in which m_{eff} is the effective mass of the oscillator [109]. Detecting the zero-point fluctuation of a mechanical oscillator, named also as standard quantum limit (SQL), has been under major research focus within the QED field. To that aim, measurement imprecision equal to SQL [110] or even below the SQL [111] is reported.

4.1.3. Diamond mechanical properties

Diamond is historically known as a hard material, for instance via its high Young's modulus. This property yields to various applications of diamond in drilling and pressing instruments. In addition, diamond has other remarkable properties which represent it as an interesting material to be used in nanomechanics and QED. Young's modulus of diamond depends on its crystalline type and quality, i.e. if it is polycrystalline or single-crystalline [112]. In addition, it depends on the orientation of the crystal. Single-crystal diamond substrates possess isotropic Young's modulus in the (111) plane, equal to 1164 GPa, as well as Poisson's ratio equal to 0.0791 [112]. These values vary for other crystal and strain orientations (planes) by $\sim 10\%$. On average, Young's modulus and Poisson's ratio of bulk CVD diamond can be mentioned as 1143 GPa and 0.0691, respectively [112]. This large value of Young's modulus does not only manifest in hardness of diamond, but also delivers relatively high resonance frequency values of diamond mechanical oscillators.

Numerous attempts have been recently reported on fabrication of diamond microcantilevers performing as mechanical oscillators [113, 50, 114]. Since diamond is chemically inert, it promotes further applications of those structures in different fluids rather than air [115].

Diamond is reported to have low intrinsic dissipation [115]. This causes a low energy loss in diamond mechanical resonators. Based on this fact and advanced fabrication techniques in addition to different possibilities of diamond surface treatment, diamond mechanical resonators in the geometry of microcantilevers with Q-factors exceeding 10^6 are reported [104]. They even could overtake the quality factors of silicon cantilevers with comparable dimensions [104].

4.1.4. Interaction of NVC with mechanical degrees of freedom

In this section, interaction of different mechanical degrees of freedom such as vibration and stress (strain) with the ground-state spin levels of the NVC is reviewed. Three pertinent contexts such as i) magnetic-mediated, ii) strain-mediated and iii) surface acoustic wave (SAW)-mediated spin-phonon coupling will be accordingly discussed. The interaction of the mentioned mechanical components with the orbital states of the NVC has also been studied before [116], however will not be mentioned here. It should be mentioned that within this thesis, spin-phonon interactions based on i) and ii) are mainly focused.

Common to all the following scenarios, is a hybrid system consisting of two main components; a) ground-state spin of the NVC and b) a mechanical resonator system with angular resonance frequency of ω which generates timely-periodic phonons. In such a hybrid system, the spin-phonon coupling strength, g, plays a crucial role. In the same way, an important figure of merit is called the cooperativity parameter, which is written as:

$$C = \frac{g^2}{\gamma\Gamma}, \tag{4.8}$$

where Γ and $\gamma = \omega/Q$ are the decoherence rate of the NVC and the dissipation rate of the mechanical resonator, respectively (Q represents the quality factor of the mechanical resonator). It is mentioned that for hybrid systems having $C > 1$, a single phonon induced by the mechanical resonator can strongly influence the coherence of the NVC probe [117]. Therefore, within such a system the interaction of the NVC and the mechanical resonator is coherent [45].

Spin-phonon interaction based on magnetic coupling

As mentioned in the first chapter, an applied magnetic field **B** to the NVC breaks the degeneracy of ground-state m_s=$|\pm 1\rangle$ spin levels via Zeeman interaction. When the NVC and the applied magnetic field oscillates spatially with respect to each other, the relevant Hamiltonian term for this interaction can be written as $\gamma_{\mathrm{NV}}(\nabla \cdot \mathbf{r})\mathbf{B}{\cdot}\mathbf{S}$ which explains the spatially-modulated Zeeman shift [45]. This is experimentally realized via installing a nanocrystal diamond hosting an NVC on a nanowire as a harmonic oscillator within a magnetic field gradient [118], or an NVC inside a bulk diamond substrate under the modulated magnetic field applied via a magnetized AFM tip [119] (see Figure 4.1-(a)). Theoretically, the Hamiltonian of the whole system is composed of three main terms dependent upon the NVC, mechanical oscillator, and the interaction between the NVC and the oscillator. The interaction of the NVC and the phonons of the vibration of the mechanical oscillator can be described by $H_{\mathrm{int}} = g\left(a + a^{\dagger}\right)S_z$ where g is the coupling strength of a single phonon to the spin of NVC given by $\gamma_{\mathrm{NV}} G_m z_{\mathrm{ZPF}}$ (γ_{NV} = 2.8 MHz/G, and z is the symmetry axis of the NVC). In the given formula, G_m is the magnetic field gradient described by $\frac{\partial B}{\partial z}$, a is the annihilation operator of the oscillator mode of the mechanical oscillator with the zero-point fluctuation shown by z_{ZPF}. These terms are previously introduced in Eq. (4.5) and Eq. (4.7). In Ref [119], spin interface of NVC via Hahn echo sequence is used to sense the mechanical motion of a magnetized AFM tip. During the delay time between the $\pi/2$ and π pulses of the Hahn echo sequence, the oscillating magnetic field caused by the AFM displacement is imprinted in the spin evolution as a coherent phase (see Figure 4.1-(b)). Therefore timely-periodic collapses and revivals occur

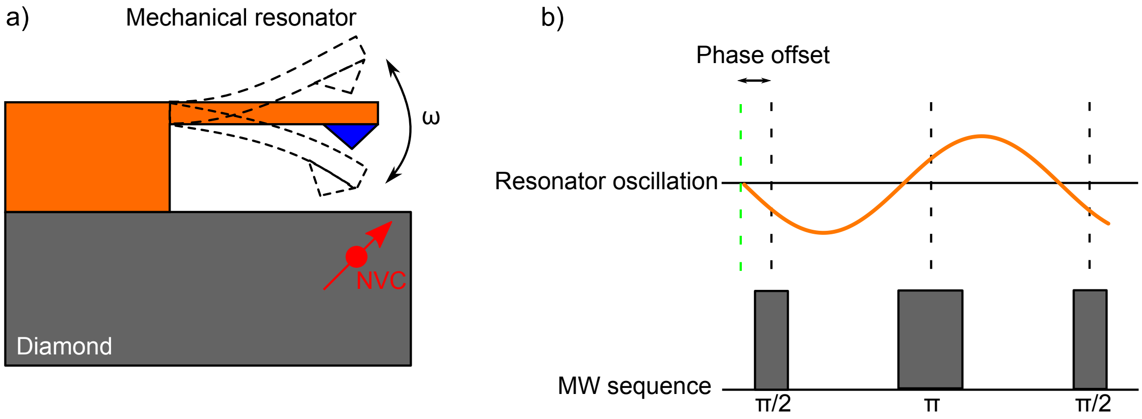

Figure 4.1.: Scheme of the spin-phonon interaction via magnetic coupling is demonstrated. (a) Shows the scheme of a mechanical resonator with resonance frequency of ω with an attached magnetized AFM tip (blue triangle) to generate a spatially-modulated magnetic field. In this case, an NVC is located inside the diamond bulk substrate. (b) Mechanical resonator oscillation with respect to the MW pulses of the Hahn echo sequence is depicted. In such a manner, the Hahn echo signal of the NVC probe can be used to describe the oscillation of the mechanical system. Figures are adapted from Ref [45].

in the fluorescence signal accumulated from the NVC as a function of the delay time (Hahn echo signal) at integer multiples of the mechanical oscillation period, $2\pi/\omega$. They reflect the spin evolution of the NVC probe due to the driven motion of the mechanical resonator. Considering the system under the explained classical mechanical drive, the fluctuations due to the thermal motion are negligible. Therefore, the resulting Hahn echo signal resembles a zeroth order Bessel function [117]. Via this context, the achieved spin-phonon coupling strength $\sim$ 10 Hz is reported [45] whereas the reported cooperativity parameters are $\ll 1$ [118, 119]. This way of spin-phonon coupling by means of classical driving of the mechanical oscillator under magnetic field gradient will be employed and described further in the next sections regarding NVCs embedded in thin circular diamond membranes and diamond microcantilevers.

Similar to the driven classical motion of the mechanical oscillator via the spin-phonon interaction, its quantum motion, i.e. its zero-point fluctuation can be also detected. Given the oscillator near its ground state, the quantum fluctuation of the oscillator can be observed via readout of the spin state of the NVC e.g. by means of Carr Purcell Meiboom Gill (CPMG) pulse sequence. To that aim, the sensitivity of the NVC probe can be enhanced by synchronizing the spin evolution with the vibration period of the mechanical oscillator, i.e. by adjusting $\tau = \pi/\omega$, where τ is the delay time between π pulses of the CPMG sequence, and ω is the angular resonance frequency of the mechanical oscillator. Therefore, a dip at the mentioned delay time in the spin coherence signal of the NVC can occur, where its dip is dependent on the number of π pulses employed in the CPMG sequence, and its width is related to the spin coherence times of the NVC, spin-phonon coupling, and the resonance frequency and quality factor of the mechanical oscillator [117].

Spin-phonon interaction based on strain-mediated coupling

In the spin-phonon coupling concept via magnetic coupling, the procedure by which the magnetic field gradient is applied to the NVC is of crucial importance. For instance, as schematically illustrated in Figure 4.1, a magnetic structure (e.g. a tip) should be placed in the nanoscale vicinity of the NVC. Here, some limiting problems such as drift effects, or degrading effects e.g. on the quality factor of the mechanical resonator might arise which can be restrictive [45]. Instead, there is an alternative way to realize spin-phonon coupling, namely the strain-mediated coupling. In this context, a monolithic diamond system is employed in which NVCs are embedded into the diamond host which is of a geometry of a well-controlled mechanical resonator e.g. microcantilevers [114, 120, 121] (this mechanical structure will be discussed in detail in the next sections). It is of a particular advantage that the strain coupling method is intrinsic to the device which in turn eliminates the mentioned limiting factors such as thermal drifts and noisy stray fields. In this platform, the vibration (periodic deflection) of the diamond mechanical resonator generates strain in the diamond crystal (see Figure 4.2-(a) and (b)), which acts similar to an effective electric field [122] at the location of the embedded NVC. Considering this effect on the ground-state of the NVC, the according Hamiltonian can be written as [45, 114]:

$$H = DS_z^2 + \gamma_{NV}\mathbf{S}\cdot\mathbf{B} + d_{||}\varepsilon_{zz}S_z^2 - \frac{d_\perp}{2}\left[\varepsilon_+ S_+^2 + \varepsilon_- S_-^2\right]. \tag{4.9}$$

In this Hamiltonian, S=1 is the Pauli spin operator, and $d_{||}$ and $d_\perp$ are the axial and transverse strain susceptibilities, respectively. The orientations are defined with respect to the NVC axis. The axial strain component is written as ε_{zz}, where $\varepsilon_\pm = \varepsilon_{xx} \pm \mathrm{i}\varepsilon_{yy}$. The raising and lowering spin-1 operators are written as $S_\pm = S_x \pm iS_y$. As given in the Hamiltonian, the axial and transverse strain play a perturbative role which leads to frequency shifts in the $m_s = \pm1$ levels, given by [45, 114]:

$$\Delta\omega_\pm = d_{||}\varepsilon_{||} \pm \sqrt{(\gamma_{NV}B_z)^2 + (d_\perp\varepsilon_\perp)^2}, \tag{4.10}$$

where the total transverse strain is denoted by $\varepsilon_\perp$ given as $\sqrt{\varepsilon_{xx}^2 + \varepsilon_{yy}^2}$ [45, 114]. As mentioned in Eq. (4.10), the axial strain induces a linear modification of the zero-field splitting (D), where the transverse one mixes the $m_s = \pm1$ states which causes a quadratic splitting between them (see Figure 4.2-(c)) [114]. The axial and transverse susceptibility constants are obtained to be $d_{||}$ = 13.4±0.8 GHz and $d_\perp$ = 21.5±1.2 GHz, respectively, using the spin readout of single NVCs inside diamond microcantilevers [121]. The strain-mediated spin-phonon coupling pa-

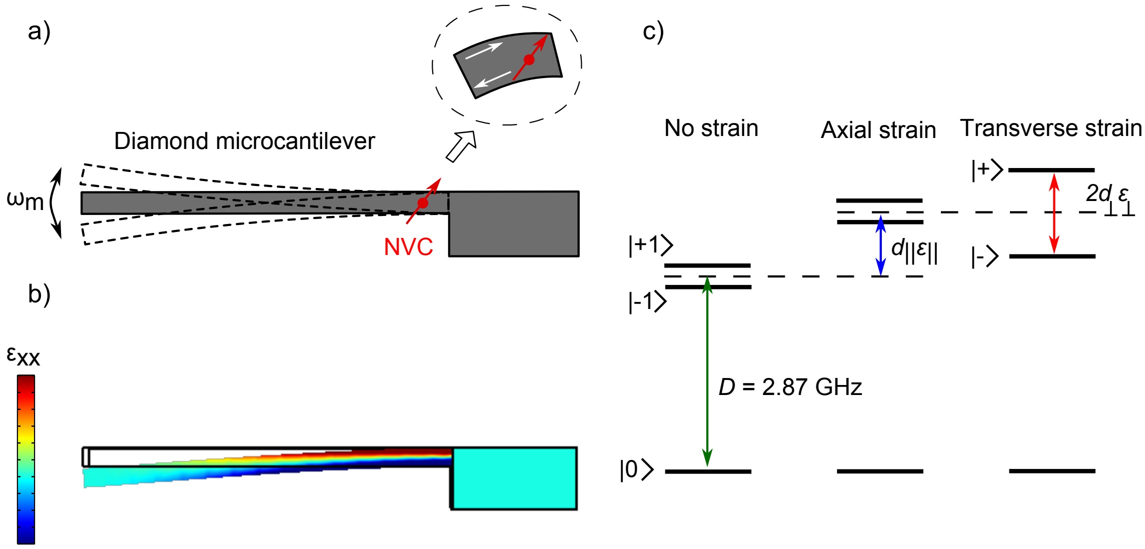

Figure 4.2.: Scheme of the strain-mediated spin-phonon coupling is demonstrated. (a) Shows the scheme of a diamond mechanical resonator (microcantilever) with an embedded NVC. The deflection of the cantilever induces strain. With respect to the FEM simulations (b) the maximum strain (ε_{xx}) is found to occur at the vicinity of the clamping point of the cantilever. (c) The effect of axial and transverse strain on the m_s=$|\pm1\rangle$ spin levels is depicted. The axial strain causes a linear shift added to the zero-field splitting, while the transverse strain mixes these states. Figures (a) and (c) are adapted from [45].

rameters are reported to be $\sim$ 0.01 Hz [120, 121], where recently a higher coupling parameter is achieved to be $\approx$ 2 Hz, by shrinking the dimensions of the diamond cantilever [114].

Spin-phonon interaction based on surface acoustic waves (SAWs)

In this part, the spin-phonon coupling based on surface acoustic waves (SAWs) will be reviewed. SAWs are phononlike excitations which are known to be bond to the surface of a solid, e.g. a piezoelectric (or piezomagnetic) material. Since the bulk and surface of the solids are different in terms of the propagation of sound waves (it behaves less rigidly at the surface), these waves are usually not matched to the bulk. They are therefore Rayleigh wave solutions which decay exponentially to the medium, showing a characteristic penetration depth of approximately one wavelength [123]. From the semiclassical point of view, these acoustic phonons create a time-dependent strain field. Similar to the previously-discussed harmonic oscillations, the zero-point fluctuation for SAWs in piezoelectric material is given by $U_0 = \sqrt{\frac{\hbar}{2\rho v_s A}}$ where ρ is the density of the solid, v_s is the sound velocity in the solid, and A is the effective mode area on the surface.

SAW resonators with Q-factor of $\approx$ 12500 at $\omega_c \geq$ 10 GHz are experimentally demonstrated in diamond heterostructures (AlN/diamond) [124]. This architecture can be used as a

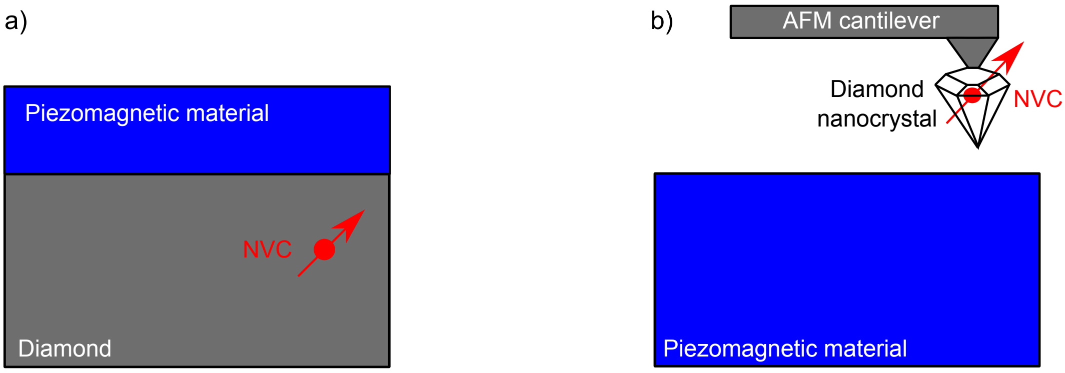

Figure 4.3.: Schematic geometry of the spin-phonon coupling of NVC via the piezomagnetic material is shown. (a) Shows a piezomagnetic material deposited on top of a diamond substrate hosting an NVC close to its surface. (b) Depicts an NVC inside a diamond nanocrystal which is positioned to the nanoscale proximity of the piezomagnetic material with the aid of an AFM tip.

platform for spin-phonon coupling with the embedded NVCs. This device can be imagined as a single NVC embedded into a diamond substrate with a distance of $\sim$ 10 nm from its surface, where a piezomagnetic layer is deposited on top of the diamond substrate. Another equivalent geometry can be formed of a diamond nanocrystal hosting an NVC that is attached to an AFM cantilever positioned in the nanoscale proximity of the piezomagnetic material (see Figure 4.3). The Hamiltonian of such a system in the presence of an external magnetic field (**B**) is given by [123]:

$$H_{\text{NV-SAW}} = DS_z^2 + \gamma_{NV}\mathbf{B}\cdot\mathbf{S} + \omega_c a^\dagger a + g_{NV}\sum_{\alpha=x,y,z}\eta_{NV}^{\alpha}S^{\alpha}\left(a+a^\dagger\right). \tag{4.11}$$

In Eq. (4.11) η_{NV}^{α} is a dimensionless factor dependent on the orientation of the NVC with respect to the magnetic field generated by the SAWs, and a is the bosonic operator for the localized SAW mode with the associated resonance frequency of ω_c. The spin-phonon coupling strength in the presence of the piezomagnetic material is estimated to be 3 orders of magnitude larger than that in the case of direct strain coupling [123]. So far, the effect of decoherence on this system has been neglected. Nevertheless, even by considering the decoherence of the NVC and the SAW mode, the cooperativity parameter exceeding 1 looks to be feasible [123].

4.2. Thin circular diamond membrane and the embedded NVCs

Recently, several breakthroughs have been achieved by coupling the fundamental vibrational mode of diamond cantilevers [125, 104, 114] to the ground-state spin of NVCs [120, 121, 126]. Besides cantilevers, thin membranes are also well-known mechanical geometries. They have been utilized in a wide range of applications from classical high-precision pressure sensing [127] to observation of quantum effects such as cavity quantum electrodynamics (QED) [99]. For instance, silicon nitride (Si_3N_4) thin membranes have been reported to be used in QED experiments [128]; such as membranes possessing lateral dimensions of few millimeters and sub-micron thickness being used in membrane-in-the-middle geometry [129]. In contrast to numerous reports on application of semiconductor membranes, realization of such a prevalent structure from diamond remains still a significant challenge to overcome. In addition to the mentioned applications, developing a diamond membrane-NVC hybrid system can open a new avenue towards further applications. For instance, based on the striking characteristics of this hybrid system like low cytotoxicity and long term stability [130], diamond mechanical structures with embedded NVCs can be found attractive for mechanobiological applications [131]. For example, they could pave the way for next-generation non-invasive, three-dimensional, and real-time observation of extracellular forces, e.g. in traction force microscopy [132].

In this section, a thin circular single-crystal diamond membrane hosting shallow-implanted NVCs will be presented. This membrane has a diameter of ≈ 1.1 mm, a thickness of $\approx 1.2\ \mu$m and surface roughness of ≈ 0.4 nm. To examine the mechanical properties of this membrane, the embedded NVCs are employed as nanosensors coupled to different mechanical degrees of freedom of the membrane. In this regard, the fluorescence point spread function (PSF) [75] measured for individual embedded NVCs is utilized to detect the deflection of the membrane under a static (DC) applied pressure. Further, by means of coupling of the ground-state spin levels of the NVCs to the mechanics of the membrane, the membrane is monitored under applied DC pressure and in-resonance vibration (AC), as well as its residual stress. Moreover, Hahn echo sequence is applied on the spin interface of the nanosensor NVCs to acquire more detailed information about the spin-phonon coupling regime. At the end, this spin-phonon coupling regime is discussed in more details featuring numerical and analytical calculations.

4.2.1. Continuum mechanics and spin-stress model

In continuum mechanics theory (CMT), circular membranes are categorized into three main classes of thin, thick, and flexible ones (see Figure 4.4). The behavior (e.g. deflection) of the flexible membrane cannot be analytically defined, and hence, it is out of study here. However,

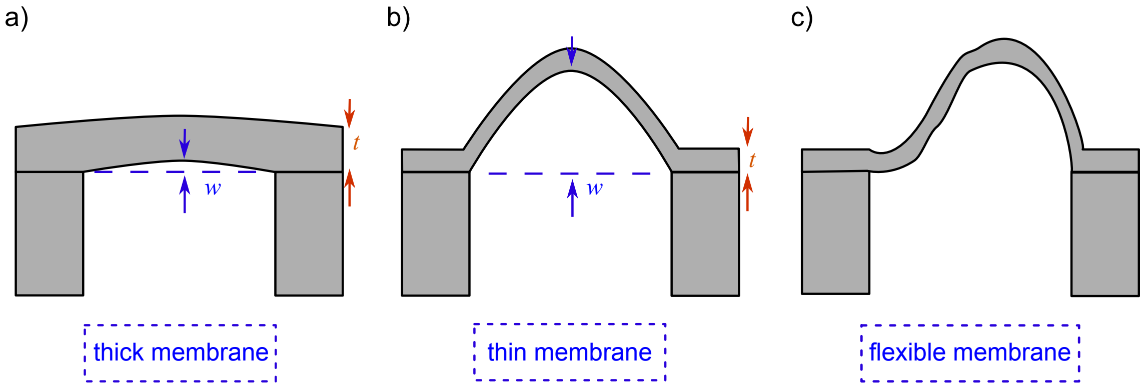

Figure 4.4.: The scheme of thick (a), thin (b), and flexible (c) circular membranes is depicted. The flexible membranes do not show well-defined behavior and hence, are out of the current study. The comparison of the thickness (t) and central deflection (w) under an applied pressure, divides the circular membranes into two main categories of thick and thin ones. Figure is adapted from [127].

based on the thickness (t) and central deflection (w) under a given applied pressure (P), circular membranes fall into two main types of thick and thin ones [127]. For thick (thin) circular membranes, w is smaller (larger) than t. For thick membranes under an applied pressure, its deflection is dominantly determined by bending moments at its rim, whereas for the thin ones, straining of its neutral fiber plays a dominant role. In reality, circular membranes are reported to have radii between $\sim 10\ \mu$m to ~ 1 mm, while for the thin membranes the thickness varies from ~ 100 nm to $\sim 1\ \mu$m and for the thick ones from $\sim 10\ \mu$m to $\sim 100\ \mu$m. The smaller membranes are challenging to fabricate, and the larger ones are usually addressed as plates. It should be noted that given a certain geometry of the circular membrane, it can show both the thick and thin membrane behaviors, while applied pressure and the resulting deflection play active roles on this classification.

Since thin circular membranes show higher sensitivity to the applied pressure in comparison to the thick ones [127], throughout this work, thin circular diamond membranes are focused. This geometry will be hereinafter shortly named as "membrane". Given a diamond membrane, the relation between the applied pressure and deflection at the center (P-w), neglecting bending moments, is given by [127]:

$$P = \frac{4tw}{R^2}\left(\sigma_0 + \frac{2}{3}\frac{w^2E}{R^2(1-\nu^2)}\right), \tag{4.12}$$

in which σ_0 and R are the radial residual stress and radius of the membrane, and $E \approx 1.2 \times 10^{12}$ Pa and ν=0.069 are the Young's modulus and Poisson's ratio of diamond, respectively [112]. Hereinafter, 1-ν^2 phrase is approximated to 1. As can be seen in Eq. (4.12), a thin membrane is expected to exhibit a nonlinear response to the applied pressure (thick membrane shows a linear response). In addition, for a given applied pressure, membranes with larger radii will deflect more. Therefore, notwithstanding a nonlinear dependence on the applied pressure, maximum pressure sensitivity will be achieved for the maximum possible radius and minimum possible thickness. Fabrication of this geometry will be addressed in detail in the next subsection.

As mentioned before, deflection of the diamond membrane under the applied pressure creates crystal stress in the diamond lattice which alters the ground-state spin resonance frequencies of the embedded NVCs (longitudinal and transverse shifts) [120, 121, 122, 133, 134]. In this part of this thesis, only the longitudinal frequency shift and thus the stress along the axis of the NVCs is studied. Assuming a cylindrical coordinate system (r,θ), the radial and tangential strain vs. the central deflection for a diamond membrane can be written as [127]:

$$\varepsilon_{RR} = \frac{2}{3}\frac{w^2}{R^2}, \ \varepsilon_{TT} = \frac{2}{3}\frac{w^2}{R^2}\left(1-\frac{r^2}{R^2}\right), \tag{4.13}$$

respectively. To convert the central deflection of the membrane to the longitudinal shift in the NVC ground-state spin resonance levels, the spin-stress model [135] is applied. For a (100) diamond surface, the matrix form of the stress tensors of each NVC orientation (given by A-D) is given by:

$$\begin{aligned} S_{\mathrm{A}} &= \begin{pmatrix} \sigma_{xx} & \sigma_{xy} & 0 \\ \sigma_{xy} & \sigma_{yy} & 0 \\ 0 & 0 & 0 \end{pmatrix} S_{\mathrm{B}} = \begin{pmatrix} \sigma_{xx} & 0 & -\sigma_{xy} \\ 0 & 0 & 0 \\ -\sigma_{xy} & 0 & \sigma_{yy} \end{pmatrix} \\ S_{\mathrm{C}} &= \begin{pmatrix} 0 & 0 & 0 \\ 0 & \sigma_{yy} & \sigma_{xy} \\ 0 & \sigma_{xy} & \sigma_{xx} \end{pmatrix} S_{\mathrm{D}} = \begin{pmatrix} \sigma_{yy} & -\sigma_{xy} & 0 \\ -\sigma_{xy} & \sigma_{xx} & 0 \\ 0 & 0 & 0 \end{pmatrix}, \end{aligned} \tag{4.14}$$

where (X,Y,Z) represents Cartesian coordinate system related to the diamond unit cell (see Figure 4.5). Therefore, the longitudinal frequency shifts for each orientation (A-D) can be given as:

$$\begin{aligned} \Delta_{\mathrm{A}} = \Delta_{\mathrm{C}} &= \frac{1}{2}\left[A_1\left(\sigma_{XX}+\sigma_{YY}\right)+2A_2\left(\sigma_{XY}\right)\right] \\ \Delta_{\mathrm{B}} = \Delta_{\mathrm{D}} &= \frac{1}{2}\left[A_1\left(\sigma_{XX}+\sigma_{YY}\right)+2A_2\left(-\sigma_{XY}\right)\right], \end{aligned} \tag{4.15}$$

where A_1 and A_2 are the stress coupling constants. As can be seen in Eq. (4.15), the different NVC orientations fall into two sets of two with distinct frequency shift distributions ($\Delta_+ \equiv \Delta_{\mathrm{A,C}}$ and $\Delta_- \equiv \Delta_{\mathrm{B,D}}$). To be able to apply the spin-stress model, Eq. (4.13) should be rewritten in the Cartesian coordinate frame. This conversion is accomplished using the Mohr's circle

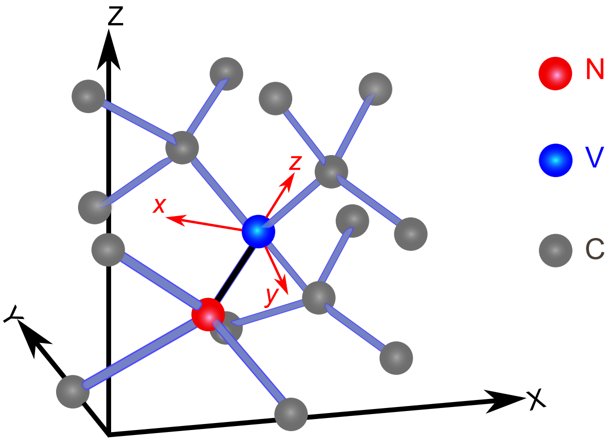

Figure 4.5.: Unit cell of the diamond with an NVC is shown to illustrate the different (x,y,z) and (X,Y,Z) notations used in the analytical study of the stress applied to the NVC spin. As depicted, (X,Y,Z) demonstrates the Cartesian coordinate system for the diamond unit cell, where (x,y,z) presents the NVC. Regarding the NVC, orientation along z is named as longitudinal, whereas x and y demonstrate transverse orientations.

concept from CMT [136], as given in this way:

$$\begin{aligned}\sigma_{XX} &= E\left(\varepsilon_{RR}\cos^2(\theta)+\varepsilon_{TT}\sin^2(\theta)\right)\\ \sigma_{YY} &= E\left(\varepsilon_{RR}\sin^2(\theta)+\varepsilon_{TT}\cos^2(\theta)\right)\\ \sigma_{XY} &= E\left(\frac{1}{2}\sin(2\theta)(\varepsilon_{RR}-\varepsilon_{TT})\right).\end{aligned} \tag{4.16}$$

Consequently, the frequency shifts obtained in Eq. (4.15) vs. the central deflection (w) for different positions of the membrane in the cylindrical coordinate system is read as:

$$\Delta_{\pm} = \frac{1}{2}E\left[A_1\left(\frac{2w^2}{3R^2}\right)\left(2-\frac{r^2}{R^2}\right)\pm A_2\sin(2\theta)\left(\frac{2w^2r^2}{3R^4}\right)\right] \tag{4.17}$$

4.2.2. Fabrication procedure

To realize the planned structure, commercially-available thin diamond films are exploited as the starting material (see chapter 2). They are CVD electronic grade ^{13}C natural abundance bulk diamond substrates commercially available by Element Six, which were machined by DDK to the dimension of ≈ 2 mm × 2 mm × 0.027 mm with the surface roughness of ≈ 2 nm (measured by AFM over several areas of 0.5 μm × 0.5 μm). After cleaning by Aqua regia and triacid mixture, nitrogen ions ($^{15}N^{+}$), with the energy and dose of 10 keV and 50 ions/μm^2, respectively, are implanted. After cleaning in Piranha solution, the sample is heated up to $\approx$ 900° C for approximately 2 hours under vacuum of $<10^{-6}$ mbar, followed by boiling in triacid

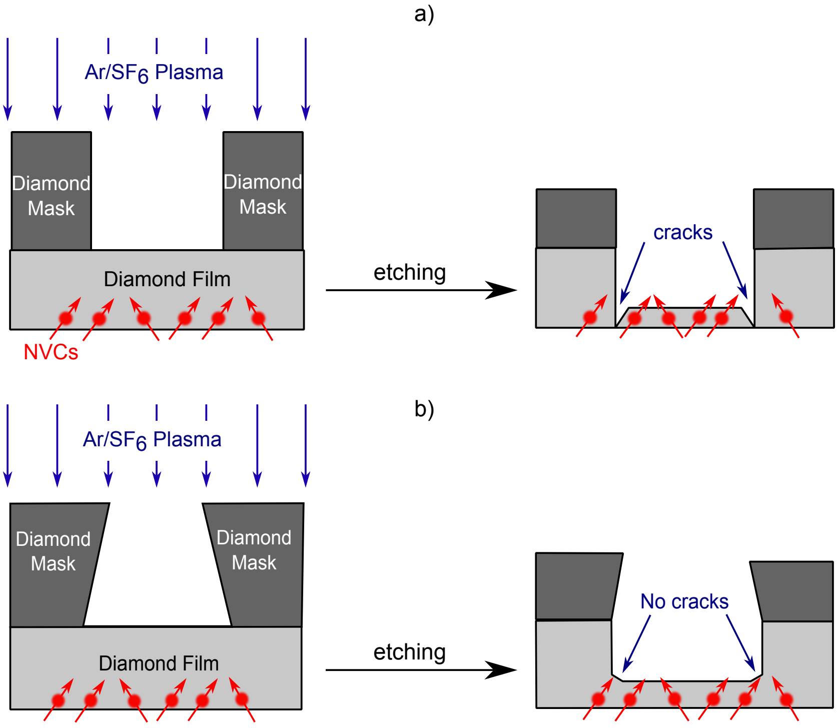

Figure 4.6.: General scheme of the exploited etching technique to transfer the circular membrane geometry to an implanted thin diamond film is depicted. The superiority of angled-wall hole in the diamond mask (b) in comparison to the vertical-wall hole (a) is shown. By using this etching mask with angled-wall hole through, no trace of trenching and cracking can be seen.

mixture [25] that finally activated NVCs. The chosen energy and dose result in single NVCs resolvable by home-built confocal microscope (see Appendix) with the average depth of ~ 20 nm [80]. Then, the sample is flipped and glued by PMMA on top of a type-I diamond substrate as structural support during the membrane geometry fabrication process. This etching process must be able to simultaneously etch the non-implanted side of the diamond thin film, with a relatively high etching rate, for > 25 μm and still leave a smooth surface. To that aim, an etching technique consisting of two crucial components; (i) the RIE-ICP etching recipe based on Ar/SF$_6$ gas mixture and ii) the auxiliary diamond etching mask, is developed.

(i) To fabricate the nanomechanical and nanophotonic structures consisting of diamond and embedded NVCs, usually etching recipes based on O$_2$ gas are utilized [64]. By using this method, relatively high etching rates ($\sim$ 150-200 nm/min) are achieved, where importantly the structure is not fluorescent in the spectral range of NVC fluorescence. However, by using this technique for more than ~ 1 μm, it is seen that the surface of the diamond becomes rough, which prevents producing high quality structures. This is due to generation of etch-induced defects at the diamond surface, which transfer more in depth as the etching process is progressing. To avoid this problem, application of plasma procedures with gas mixture of Ar and Cl_2 are repeatedly reported [50, 137]. This technique ends in smooth final surface ($\sim$ 1 nm RMS roughness), nevertheless is relatively slower ($<$ 100 nm/min) than the O_2 recipe [137]. In this work, a novel etching recipe based on gas mixture of Ar and SF_6 is developed. This recipe turns out to show the benefits of both of the mentioned etching recipes. Through this recipe, the main etching (sputtering) task is done by Ar gas, where the SF_6 gas helps to smooth the diamond surface, simultaneously.

(ii) To perform top-down fabrication technique based on deep etching of diamond, the etching mask is of great importance. Not only to show less etching rate in comparison to diamond and hence act as a mask, it should also not introduce additional roughness of the etched surface. To avoid the final rough area, it is decided to use bulk diamond substrate as the etching mask. In this way, no additional surface roughness is introduced by redeposition of the etching mask. In addition, since the thickness of the mask is one order of magnitude larger than the sample itself, it does still sufficiently act as an etch mask. This mask is a type-I diamond (see chapter 1), in which a hole is laser cut at its center by Medidia GmbH roughly with the same diameter as the final membrane, however importantly with angled wall profile (16°).

Etching rate of diamond in the vicinity of its etched wall is larger than at the other places, resulting in thinner parts close to the rim of the circular membrane, i.e. trenching effect. This is due to concentration of the ions in the vicinity of the etched wall [138], which indeed causes cracks in the final structure. To tackle this problem, an angled-wall diamond mask is applied. By using this mask, the problem is solved through faster corrosion rate of the mask close to the hole in comparison to other places. Therefore, at the rim of the membrane, diamond film is etched less than its center, which compensates the trenching effect. Schematic explanation of this process can be found in Figure 4.6.

The etching process is done in Oxford PlasmaPro NGP80 RIE-ICP machine under vacuum of $\sim 10^{-6}$ mbar, plate temperature of 20° C, RIE power of 100 W, ICP power of 600 W, and gas flow of 40 sccm and 25 sccm for SF_6 and Ar, respectively, under the chamber pressure of 20 mTorr. To minimize side effects of the heat generated by the etching process, it is divided into consequent etching/cooling steps of 5 min/2 min, respectively. After etching, to remove the fluorine termination, the surface is etched for few nanometers by means of soft ICP oxygen plasma technique [25]. To check the etching depth and profile, the resulting sample (see Figure 4.7-(a)) is inspected by Dektak profilometer (see Figure 4.7-(b)), giving the etching depth of $>$25 μm which shows etching rate of $\approx$ 170 nm/min. The comparison of the initial thickness and the etching depth denotes the thickness of the membrane at the center of the diamond film to be 1-2 μm. Further, it shows only $\approx$ 1 μm deviation of thickness over the whole diameter of 1.1 mm, denoting only 0.1% deviation. The resulting surface roughness is measured over 1 μm $\times$ 1 μm area in several positions of the membrane by means of AFM, revealed to be $\approx$ 0.4

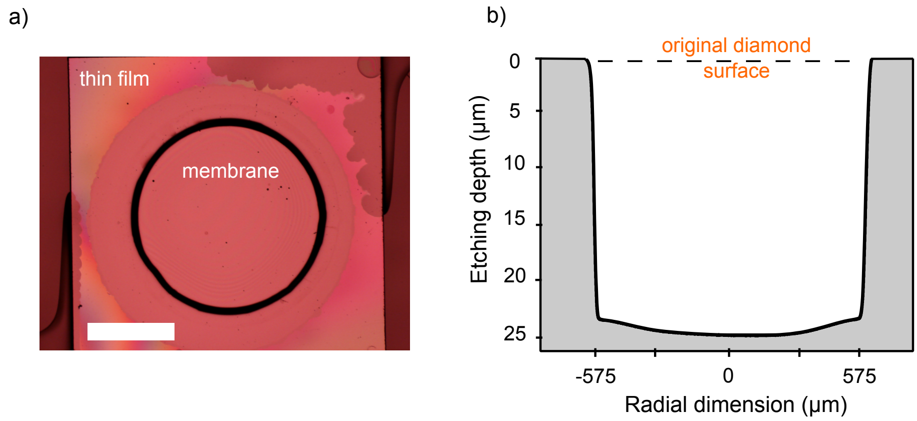

Figure 4.7.: The hybrid NVC-diamond membrane system is demonstrated. The fabrication process results in a (a) $\approx$ 2 mm $\times$ 2 mm $\times$ 0.027 mm diamond film with a 1.1 mm diameter thin membrane at its center. It is glued on a glass with a hole at its center to avoid mechanical contact to the membrane. Scale bar shows 500 μm. (b) The etching profile of the fabricated sample is shown, where the etching depth of $>$ 25 μm is revealed. By using the angled-wall hole in the diamond mask substrate, no trace of cracks and trenching can be seen in the final sample, where only a minor thickness deviation of $\sim$ 0.1% through the whole diameter is left.

nm. This shows approximately 5-fold improvement of the surface roughness in comparison to its initial value, by means of the presented novel etching recipe, even after etching $>$25 μm of diamond.

4.2.3. Experimental characterization

The fabricated hybrid device is mounted in the home-built confocal setup (see Appendix) as it is schematically shown in Figure 4.8-(a). To avoid mechanical contact with this device, it is mounted on a glass holder with a central hole. For the same reason, to apply MW pulses, a 20 μm-diameter copper wire is spanned over its thick part. The acquired confocal image of an area near the center of the membrane (Figure 4.8-(b)) proves the right applied implantation parameters, as well as the gentle deep etching process. To obtain information about the mechanical properties of the device, it is installed in a nitrogen gas pressure vessel (as depicted schematically in Figure 4.8-(a)), positioned on top of the confocal setup. The membrane deflection under a DC pressure is measured by monitoring the fluorescence PSF (along the optical z- axis) of single NVCs near the center of the membrane, as the nitrogen gas pressure is increased. The recorded applied pressure vs. deflection of the membrane at its center is shown in Figure 4.9-(a). The non-linear (cubic polynomial) behavior clearly shows that the final hybrid structure obeys the CMT of thin circular membranes. By fitting the data using the model given in Eq. (4.12), values of t = 1.2 $\pm$ 0.2 μm and σ_0 = 54 $\pm$ 6 MPa for the effective

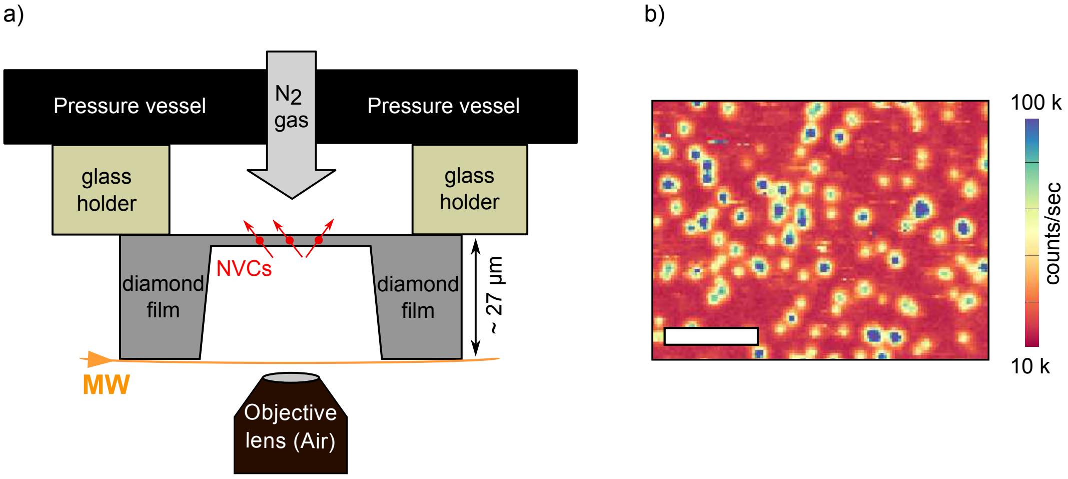

Figure 4.8.: The mounting of the hybrid diamond membrane-NVC system is schematically illustrated. (a) It shows the hybrid device mounted under a nitrogen gas vessel in a home-built confocal setup. (b) The confocal image from an area near the center of the membrane is presented. It shows no negative effect caused by the applied fabrication process. Scale bar represents 3 μm.

thickness and the radial compressive residual stress of the device, respectively, are obtained. This derived thickness is in good agreement with the value of $\sim$ 1-2 μm, estimated by optical microscopy. It should be added that even for the applied pressures up to 3 bar, no damage to the hybrid device can be monitored. Analytically, the burst pressure of the membrane device is given by [127]:

$$P_{\text{burst}} = 4\frac{t \cdot \sigma_y}{R}\sqrt{\frac{3}{2}(\sigma_y - \sigma_0)\frac{1-\nu}{E}}, \tag{4.18}$$

in which $\sigma_y \approx$ 90 GPa is the yield stress [139] of diamond. Given the values for diamond and geometry of the presented membrane, burst pressure is $\sim$ 2500 bar. This value sounds more ideal rather than realistic for the presented experiment, since breaking of the membrane in the installation points occurs likely at much lower pressures.

As a complementary attempt, to assess the sensitivity of the presented hybrid device to pressure, a small pressure is applied to the system while monitoring the fluorescence photon count rate of a single NVC located at its center. As can be seen in Figure 4.9-(b), $\approx 2 \times 10^3$ counts/sec decrease in the photon count rate is clearly observed. This change in the fluorescence rate can be attributed to the displacement in z- focus of the PSF of the NVC sensor and hence, converted into an applied DC pressure as small as $\approx$ 40 Pa. In this case, the photon shot noise limit on the pressure sensitivity is $<6\ \frac{\text{Pa}}{\sqrt{\text{Hz}}}$. This value can be improved by increasing the photon count rate of NVCs as nanoprobes through incorporating an ensemble of NVCs into this structure.

To compare the minimum detected pressure (MDP) of the presented hybrid device us-

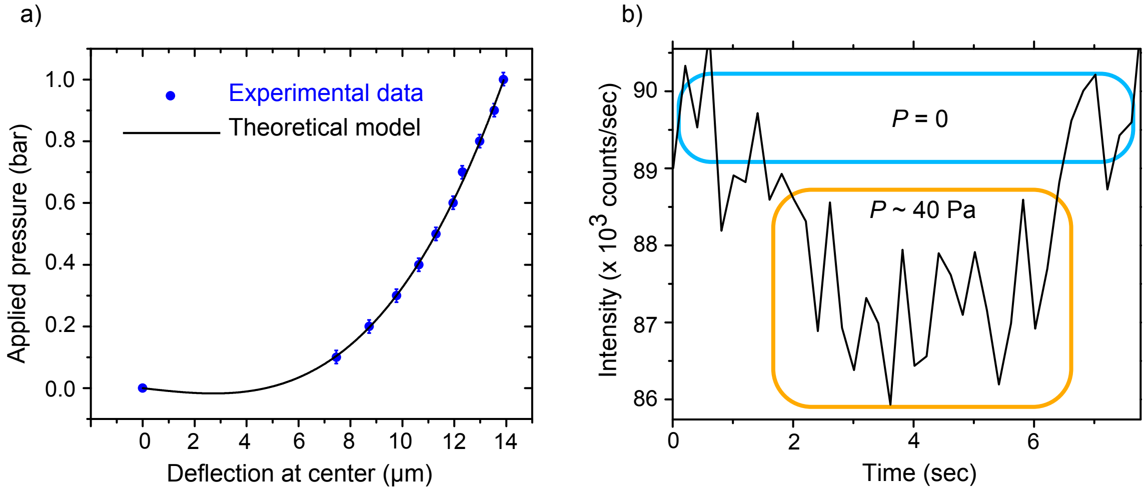

Figure 4.9.: Optical investigations of the membrane-NVC hybrid system are depicted. (a) Applied DC pressure to the system vs. deflection at its center is plotted. The cubic polynomial behavior of the curve is a clear characteristic of the mechanics of a thin circular membrane. Vertical error bars demonstrate 0.05 bar whereas the horizontal error bars are not shown. (b) Recording the fluorescence rate of a single NVC located at the center of the membrane in the absence and presence of a small applied pressure is shown. As explained in the main text, this pressure is calculated to be $\approx$ 40 Pa.

ing quantum nanosensors ($\approx$ 40 Pa) with recently presented microelectromechanical systems (MEMS)-based pressure sensors, it can be said that the developed device is comparable to the MEMS piezoelectric or capacitive pressure sensors (MDP $\sim$ 10-1000 Pa) [140, 141, 142, 143], however less sensitive in comparison to the achieved value by flexible sensors, i.e. MDP=0.1 Pa [144].

After using the optical interface of the embedded nanosensor NVCs, their ground-state spins are also utilized to monitor the DC mechanical motion of the membrane. As described in Eq. (4.17), two different frequency shifts ($\Delta_{\pm}$) are expected for two different sets of NVCs crystallographic orientations (A,C and B,D) under the (100) diamond surface (see Figure 4.10-(a)). These two shift distributions show identical maxima at the center of the membrane (r = 0). By considering the thickness and radius of the membrane equal to 1.2 μm and 575 μm, respectively, the longitudinal frequency shift in the ground-state spin resonance of a single NVC at the center of the membrane can be calculated in this way:

$$\Delta_{+,\text{center}} = \Delta_{-,\text{center}} \approx 0.012 \left[\text{MHz}/\mu\text{m}^2\right] \times w^2 \tag{4.19}$$

where w in μm is the deflection at the center of the membrane. To measure this frequency shift, ODMR measurements are performed on single NVCs located near the center of the membrane. To be confined to the longitudinal frequency shift and suppress the transverse one,

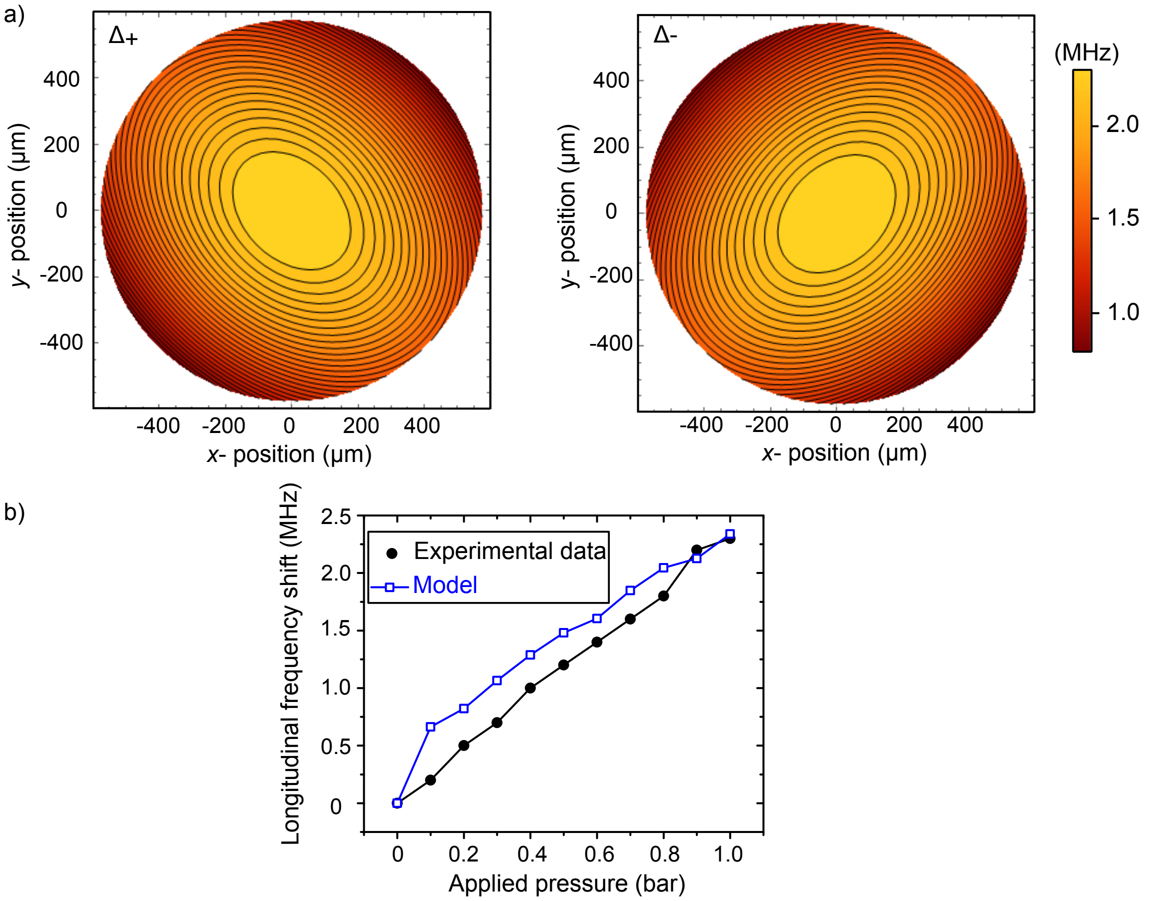

Figure 4.10.: (a) The simulation of the longitudinal frequency shift (absolute value) distribution over the membrane area is plotted (for an applied pressure of 1 bar) for two different sets of NVC crystallographic orientations. There is an azimuthal asymmetry in both of the plots, which is imposed by breaking of the symmetry due to the nonsymmetric orientation of the NVCs. (b) The absolute value of the experimental and the model data of the longitudinal frequency shift detected by a single NVC located at the center of the membrane is depicted. The developed model considering the membrane mechanics and the spin-mechanical interactions predicts similar behavior as the ODMR measurements.

approximately 90 G of magnetic field is aligned to the axis of the NVC under investigation. As plotted in Figure 4.10-(b), a linear behavior of the longitudinal frequency shift (plotted in absolute values) vs. the applied pressure is observed, showing a gradient of ≈ 2.3 MHz/bar. As shown in Figure 4.10-(b), an appropriate consistency between the experimental and theoretical curves (based on Eq. (4.19)) can be seen, which supports the developed model of the spin-mechanical coupling and mechanics of the membrane. A slight deviation between these two curves can be however attributed to the small inhomogeneity in the thickness of the membrane close to its rim as well as non-ideal clamping conditions.

Similar to the optical interface of the nanosensor NVCs, their ground-state spin could be

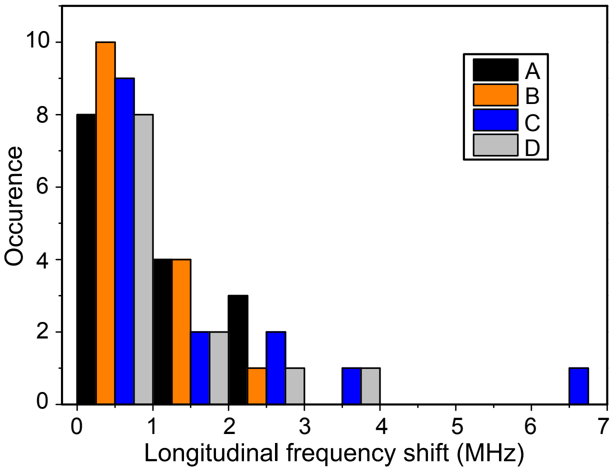

Figure 4.11.: A histogram of the longitudinal frequency shift of approximately 15 NVCs per each crystallographic orientation (A-D) from D = 2.870 GHz is measured. Common to all four different orientations, most of the NVCs show longitudinal frequency shifts lower than 1 MHz. As mentioned in the main text, this yields in average frequency shift of 0.82 MHz which is translated in approximately 52 MPa of net radial residual stress.

also used to measure small DC pressures. As an example, one can use Ramsey interferometry to detect small strain field (pressure). Ramsey signal as a function of waiting time (τ) can be written as [145]:

$$S_R(\tau) = C_1 - C_2 e^{-\left(\frac{\tau}{T_2^*}\right)} \cos(\omega\tau) \tag{4.20}$$

where C_1 and C_2 are positive fitting parameters, T_2^* is the coherence time, and ω is the detuning of the microwave frequency from the zero-field splitting (D). This detuning can be written as sum of magnetic, pressure, and temperature shifts, respectively:

$$\omega = 2\pi\left(\Delta f_B + \Delta f_P + \Delta f_T\right) \tag{4.21}$$

The above-mentioned shifts can be rewritten e.g. as Δf_T = C$_T$.δT or Δf_P = C$_P$.δP where C$_T$ $\approx$ 70 kHz/K (at room temperature) and C$_P$ $\approx$ 2.3 MHz/bar (as reported here) are the coupling constants for temperature [146] and pressure, respectively, and δT and δP are the changes in temperature and pressure, respectively.

To suppress the magnetic noise one can use alternative sequences, e.g. presented in [44] or elsewhere [53]. Still, to measure small pressures, one should certainly overcome temperature fluctuations. It means that for the spin-based technique to match the $\approx$ 40 Pa sensitivity of the photon-based technique, the temperature of the sample should be constant within 10 mK range, which is challenging under realistic circumstances. Consequently, it can be concluded that the measurement technique based on the optical interface of the embedded NVCs is superior for piezometry at low pressures.

In addition to the applied static pressure, single NVCs are also applied as local probes to sense the residual stress in the device. Residual stress is an inevitable component of micro- and nanostructures, which effectively deviates their mechanical properties from the expected values [127]. This deviation consequently complicates/limits their application. As assumed in CMT, the main residual stress in the circular membrane geometry is the radial residual stress due to clamping [127]. To measure this residual stress, ODMR signal of 15 NVCs per each four different orientations, located radially at the center of the membrane, are measured (see Figure 4.11). The measured longitudinal frequency shift from the default value of $D = 2.870$ GHz is then recorded, giving the average shift of ≈ 0.82 MHz (Figure 4.11). To exclude the residual stress due to the vicinity of the NVCs to the diamond surface, 30 implanted NVCs (in the same depth) are inspected in a reference sample. Then, by the same method, frequency shift of ≈ 0.57 MHz is obtained, which gives the net frequency shift of ≈ 0.25 MHz. Based on the spin-stress model and CMT (Eqs. (4.12), (4.17)), radial residual stress of $\sigma_0 \approx 52$ MPa is obtained, showing a good agreement with $\sigma_0 \approx 54$ MPa achieved through optical measurements. This result manifests the capability of NVCs as nanoscale probes to peruse the residual stress in diamond mechanical structures.

4.2.4. NVC-oscillator system

In this part, measurements on the NVC optical and spin interfaces, and the membrane as a mechanical oscillator are focused. Towards implementation of proposals based on spin-phonon coupling in NVC spin-oscillator systems [147, 117], the AC mechanical behavior of the NVC-membrane device is studied. In this way, the lowest order (fundamental) vibrational mode of the membrane is investigated. This mode resembles a drum-shape vibration which shows maximum amplitude at its center [127]. To excite this fundamental mode, the membrane is installed on top of a piezo chip connected to a frequency generator (see Appendix). To acquire the resonance frequency, the fluorescence photon count rate of a single NVC near the center of the membrane is monitored while the frequency of the piezo chip is swept. A dip in the fluorescence intensity at $\omega \approx 2\pi\times 63$ kHz is detected, indicating the fundamental resonance mode of the membrane (Figure 4.12-(a)). The same result is observed using photodiodes to check the reflected laser power back from the center of membrane [125, 104, 113]. To exclude the resonance behavior of the piezo chip itself through the mentioned measurements, the thick part of the diamond film lying far from the membrane is also monitored. Using both of the mentioned techniques, a 2-digit quality factor (10-80) is obtained. Since the quality factor is likely to be limited by atmospheric damping, higher quality factors are expected to be achieved in vacuum [104]. Next, the vibrational amplitude of the membrane is estimated optically via observing the vibrationally-induced broadening of the focus point width of the NVC sensor. In this way, the vibrationally-induced broadening of the focus of single NVCs near the center of the membrane is estimated vs. different piezo driving voltages (Figure 4.12-(b)) [148]. Like the displacement with DC pressure, the vibrational amplitude is non-linear in the piezo driving voltage. Nevertheless, for small voltages (<2 V) the vibration amplitude is seen to be approximately linear. In this voltage regime, a linear slope of ≈ 0.38 μm/V can be fitted. It should be noted that this non-linear behavior can be stemmed from the piezo chip itself. However, this reason is excluded with respect to the technical specifications of the piezo chip.

As the next step, coupling of the spin of NVCs to the fundamental mode of the membrane is studied. To that aim, spin-echo (Hahn echo sequence) measurements are performed on single NVCs near the center of the membrane while its fundamental mode is driven. A magnetic field of ≈ 290 G is also aligned to the axis of NVCs. As discussed before, NVCs near the center of the membrane couple dominantly to its fundamental vibration mode. This vibration induces a modulation of the applied magnetic field sensed by the NVC and thus its spin resonance frequencies [117, 121]. This vibrationally-induced interaction between the NVC spin and the membrane oscillator can be estimated in the linear regime (low piezo voltages) through a periodic detuning term $gz(\tilde{v})\cos\omega\mathrm{t}$, where g is the coupling parameter of the spin to a membrane vibration phonon, and $z(\tilde{v})$ is the voltage-dependent dimensionless amplitude of the oscillation (i.e. vibration amplitude at each piezo driving voltage divided by $z_{\mathrm{ZPF}} \sim 10^{-16}$ m) [117]. As explained in the last section about spin-phonon interaction mediated by magnetic coupling, this non-synchronized vibrationally-induced detuning results in decoherence of the NVC spin, observable e.g. in Hahn echo signal (Figure 4.13-(a)). The resulting Hahn echo signal as a function of waiting time (τ) can be given by the product of the zeroth order Bessel function and an exponential decay term based on T_2 time, as follows [117]:

$$H(\tau) = A\mathrm{J}_0\left(4\frac{g\widetilde{z(v)}}{\omega}\sin^2(\frac{\omega\tau}{4})\right)e^{-\chi(\tau)}e^{-(\frac{\tau}{T_2})^{\gamma}} + B, \qquad (4.22)$$

where ω is the eigenfrequency of the membrane oscillator ($2\pi\times63$ kHz), $\chi(\tau)$ is the dephasing due to thermal motion which is negligible in mechanical-driven regime [117], and A, γ, and B are the fitting parameters. Given the vibration amplitude vs. different piezo voltages from Figure 4.12-(b), by fitting the function in Eq. (4.22) to the Hahn echo signal at each piezo voltage, the corresponding values of T_2 and g can be obtained. For instance, the coupling parameter is estimated to be $g = 6.12\pm0.51 \times 10^{-4}$ rad/s (Figure 4.13-(b)). On the other hand, having the T_2 times at different piezo voltages, the driven decoherence rate can be calculated

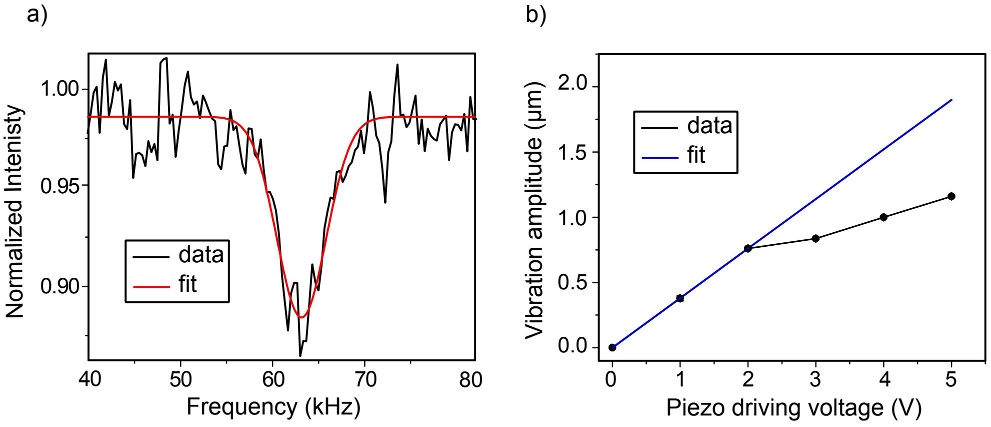

Figure 4.12.: (a) Measurement of the fundamental mode frequency of the membrane by means of embedded single NVC is shown. (b) In-resonance vibration amplitude of the membrane vs. the piezo driving voltage is estimated by means of single NVCs, revealing an overall nonlinear behavior. Nevertheless, this behavior can be approximated to a linear fit with slope of 0.38 μm/V for voltages <2 V.

accordingly [120]:

$$\Gamma(V) = 2\pi\left(\frac{1}{T_{2(V)}} - \frac{1}{T_{2(V=0)}}\right), \tag{4.23}$$

where $T_{2(V=0)}$ is the NVC spin coherence time at the absence of the membrane vibration. The corresponding decoherence rate vs. different piezo driving voltages is then demonstrated in Figure 4.14-(a). As shown, it presents an ascending behavior as piezo driving voltage increases. The precise origin of this voltage-dependent decoherence rate is not clear. However, it can be related to the non-linearity of the membrane's mechanics and related factors, such as imperfect damping and coupled excitation of multiple vibrational modes. Further investigations would be subject of future works.

With respect to the theoretical explanations before, the derived spin-phonon coupling can be originated in either stress-mediated, or magnetic field gradient-mediated processes. As the mentioned measurements are performed under $\sim$ 300 G of applied magnetic field aligned to the NVC axis, any unexpected spin transverse interaction is considered to be canceled out. The only stress-mediated frequency shift is therefore the longitudinal one, which can be estimated using Eq. (4.19) for e.g. 0.5 μm of vibration amplitude to be $\sim$ 3 kHz. On the other hand, the frequency shift induced by the magnetic field gradient generated via the same membrane vibration amplitude under the static applied magnetic field is estimated to be $\sim$ 30 kHz. Since this value is approximately one order of magnitude larger than the strain-mediated frequency shift, it is assumed that the explained spin-phonon coupling is mainly induced by the magnetic field gradient. As given in [117], the vibrationally induced magnetic field gradient can be calculated as $g/(\gamma \cdot z_{\mathrm{ZPF}}) \sim 27$ T/m (γ is the gyromagnetic ratio equal to 2.8 MHz/G for

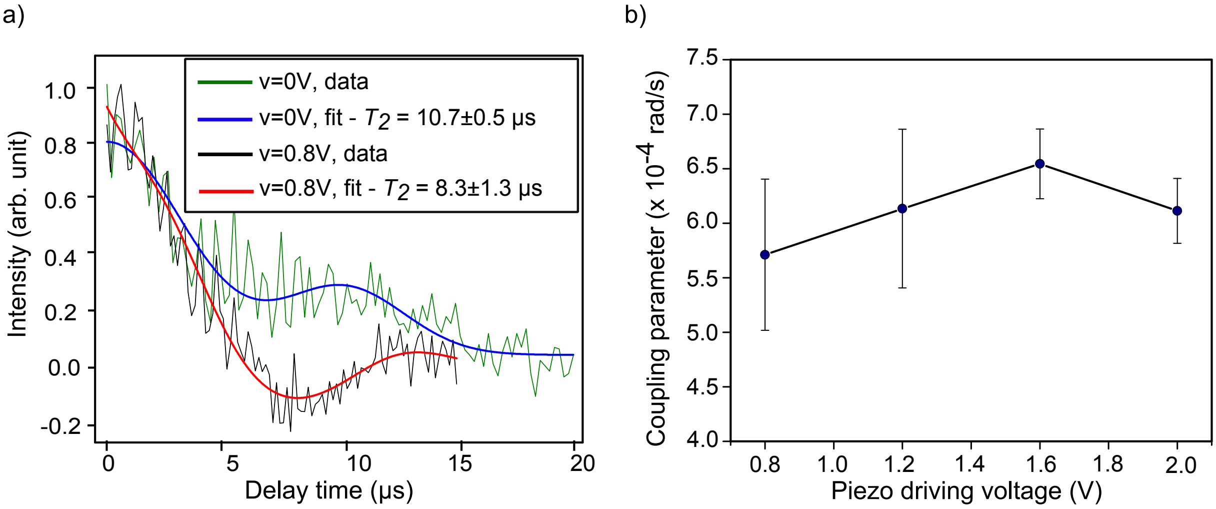

Figure 4.13.: (a) Hahn echo signal under ≈ 290 G in absence (green curve with blue fit [24]) and presence (black curve with red fit) of in-resonance mechanical driving is demonstrated. An oscillation behavior obeying Bessel function proves that the system is in driven regime, as presented theoretically before [117]. (b) Coupling parameter of the spin of a single NVC to a single phonon of membrane vibration vs. the piezo driving voltage is shown. As depicted, almost a constant value is obtained to be $g = 6.12 \pm 1.09 \times 10^{-4}$ rad/s.

g-factor of 2).

Regarding further realizations of proposals towards quantum information processing using NVC-diamond mechanical hybrid devices [147], the coupling parameter can be drastically improved by reducing the membrane dimension and applying a higher magnetic field gradient. For instance by further reducing the radius and thickness of the membrane to 100 μm and 0.3 μm, respectively, and by employing magnetic structures [149, 150] introducing magnetic field gradients of 5×10^6 T/m, the coupling parameter can be improved by 5 orders of magnitude exceeding g of 50 Hz. This term plays an important role since the cooperativity term (Eq. (4.8)) scales with g^2 [117].

4.3. Diamond microcantilevers and embedded NVCs

So far, interaction of isolated NVCs with stress (strain) and vibration of mechanical structures is presented. This interaction was first theoretically explained, which was then studied within a developed circular diamond membrane platform. In this platform, embedded NVCs were utilized e.g. as nanosensors for applied and residual stress. This NVC-membrane hybrid system was also characterized as a spin-oscillator system in which spin-phonon coupling was assessed. It was derived that by miniaturizing this system, higher spin-phonon coupling strengths are achievable. Given this, this hybrid system can be employed in further quantum-mechanical

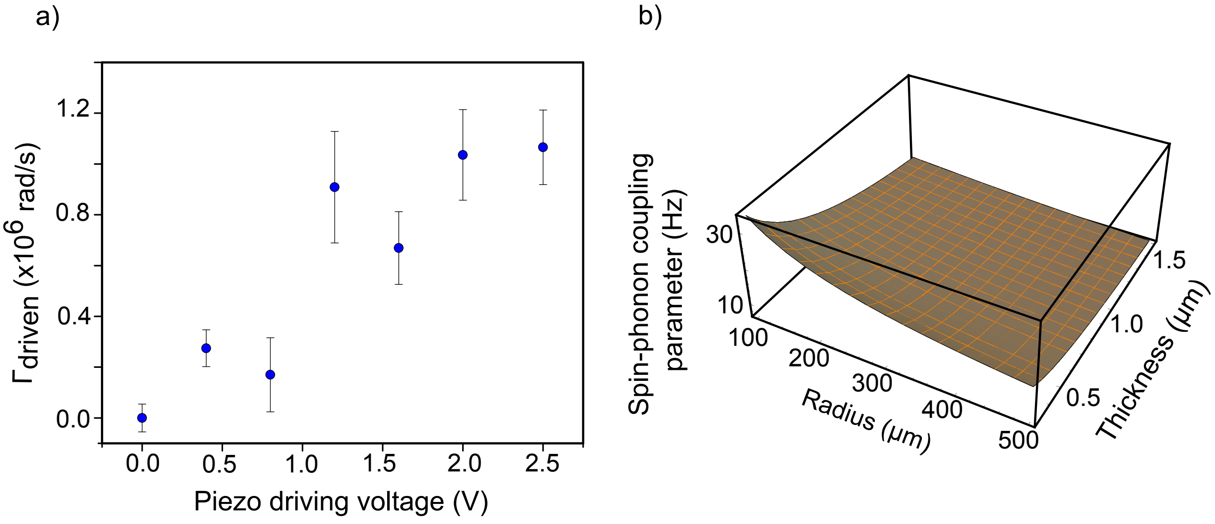

Figure 4.14.: (a) Driven decoherence rate is plotted vs. the driving voltage of the piezo chip. Nonlinear behavior of the membrane oscillator and possible heating effects can cause ascending decoherence rate. (b) Simulated spin-phonon coupling parameter (g in Hz) is shown vs. radius and thickness of the membrane. In this simulation, residual stress of the membrane and the magnetic field gradient are considered to be 100 MPa and 5×10^6 T/m, respectively.

applications (such as QED applications). To implement hybrid quantum-computing architectures, there are proposals e.g. in [151] on application of NEMS. In these proposals NEMSs play a role as quantum spin transducers which consist of an array of coupled mechanical oscillators hosting NVCs, whereas a magnetic field gradient provides an efficient spin-phonon coupling. To approach this goal, an alternative to the thin circular membrane geometry would be free standing beams, which can be fabricated in an array form with the desired geometry and dimension.

Free standing beams are well-known mechanical systems with vast magnificent applications in mechanical structural engineering to MEMS (and/or NEMS) devices [127]. For instance, in MEMS/NEMS devices they are presented to play the central important role as the sensor for detection of ultra-small masses, e.g. in molecular scales [152, 153], thanks to their ultra-small mass and high Q factors [104]. Recently, these devices (mostly cited as cantilevers) have been fabricated from single-crystal diamond substrate, both in micro- [113] and nanoscale [50, 125] dimensions, offering applications in hybrid NVC-mechanical systems [116, 120, 121].

Cantilevers were repeatedly mentioned in the theoretical section at the beginning of this chapter. However, a continuum mechanics background of these devices is still missing. In the coming subsection, a brief introductory knowledge of cantilevers based on continuum mechanics will be given. In the next subsection, double diamond cantilevers as coupled mechanical oscillators will be demonstrated. Then, fabrication of those devices employing a novel

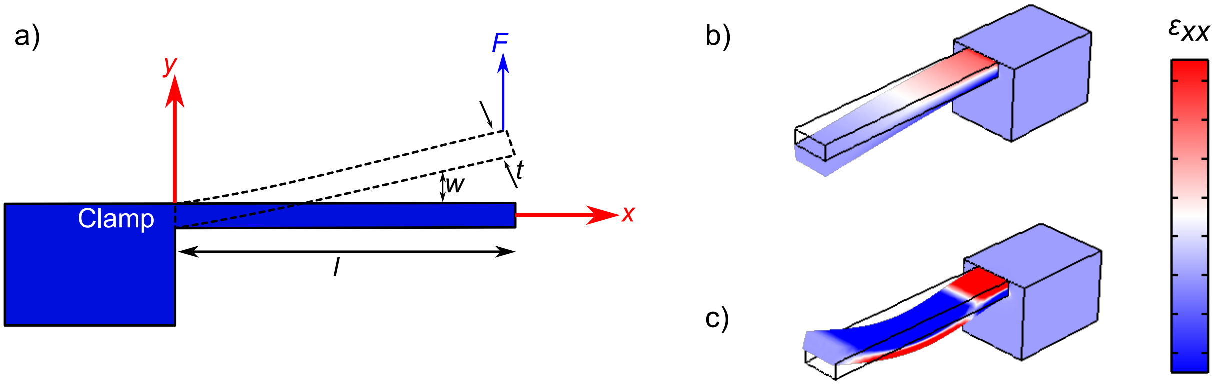

Figure 4.15.: Scheme of a single-side clamped microcantilever with rectangular cross-section is shown. (a) 2D scheme of the cantilever with the length and thickness of l and t, respectively, under a transverse (parallel to y axis) applied force F at its free end is demonstrated. This force induces a deflection (w) parallel to the cantilever thickness, which depends on the coordinate along its length (x). Figures (b) and (c) present the first two vibrational flexural modes of the cantilever. (b) Presents the 1^{st} flexural mode of the cantilever which is called as fundamental mode. (c) Shows the 2^{nd} vibrational flexural mode of the cantilever. In figures (b) to (c), the FEM-simulated spatial distribution of the strain component ε_{xx} through the cantilever geometry is shown. For instance, given the fundamental mode, strain is maximum close to the clamping point of the cantilever.

fabrication technique will be presented, followed by their optical characterization. At the end, perspective of these devices towards quantum applications such as cooling will be discussed.

4.3.1. Cantilevers in continuum mechanics

Although cantilevers with different cross-sectional geometries such as circle and trapezoid forms have been analytically studied, in this part only the ones with rectangular cross-section will be considered. In addition, since the single-side clamped cantilevers are mostly focused in the NVC-mechanical hybrid systems, only these systems [127] will be explained here.

Here, a cantilever with thickness, width, and length of t, d, and l, respectively, only clamped at one side is assumed. A constant force of F is applied to its free end which causes it to deflect (see Figure 4.15-(a)). This deflection (w) is a function of the distance from the clamping point of the cantilever, x, and is given by [127]:

$$w = \frac{2F}{Edt^3} x^2 (3l - x), \tag{4.24}$$

in which E is the Young's modulus of the cantilever. Usually the deflection at the free end of the cantilever (tip) is important (shown by w_0), which can be obtained by putting $x = l$ in Eq. (4.24). Deflecting the cantilever (as depicted in Figure 4.15-(a)) induces strain in it. This strain has its maximum magnitude at the surface of the cantilever. On the other hand, the maximum value of such a strain can be found at the clamping point of the membrane. Given an applied force F which induces a maximum deflection of w_0 at the free end of the cantilever, the strain at the surface of the cantilever and along the x axis is written as [127]:

$$\varepsilon_{XX}(x) = \left(\frac{3}{2}\right)\frac{t\,(l-x)}{l^3}w_0. \tag{4.25}$$

It should be mentioned that sign of the force and strain depends on their direction with respect to the deflection. For instance, given a certain w_0 and for a given x, the absolute value of ε_{XX} is identical for both surfaces of the cantilever, however at one side it is positive and at the other one it is negative (tensile and compressive strain). Nevertheless, for the sake of simplicity, only their absolute values are mentioned above in Eqs. (4.24) and (4.25) [127].

After considering the cantilevers in static mode, their dynamic mode i.e. their vibration will be shortly discussed here. For a cantilever which is clamped at one side and free at another side, several vibrational modes exist. Each vibrational mode associates with specific resonance eigenfrequency and possesses specific deflection behavior. The first two vibrational (flexural) modes of such a cantilever are simulated by FEM software and shown in Figures 4.15-(b) and -(c). The first resonance mode (see Figure 4.15-(b)) is usually named as the fundamental mode. With respect to Euler-Bernoulli beam theory and neglecting the residual stress of the cantilever, the resonance frequency of this mode is inversely scaled with l^2 of the cantilever and is given by [127]:

$$f_1 \approx 0.16\left(\frac{t}{l^2}\right)\sqrt{\frac{E}{\rho}}, \tag{4.26}$$

where E and ρ are the material-dependent Young's modulus and density of the cantilever, respectively [127]. As can be seen, this resonance frequency is not dependent upon the width of the cantilever (d). It is worthy to mention that Eq. (4.26) is written for ideal-shaped cantilevers, e.g. as shown in Figure 4.15. In case of deviation from the ideal geometry, the real resonance frequency will be accordingly deviated from the given value in Eq. (4.26) [154].

4.3.2. Mechanical quantum bus

One of the key issues in the context of quantum computing is the scalability of the quantum nodes (qubits) and hence the entire quantum computer itself. To that aim, coupling distant qubits has been actively pursued in recent years. Several architectures employing different quantum buses have been proposed in this regard. For instance, coupling of distant quantum dots was reported by means of MW resonators as the appropriate quantum bus [155]. Equivalently, distant quantum dot circuits were coupled by means of cavity photons [156]. Toward

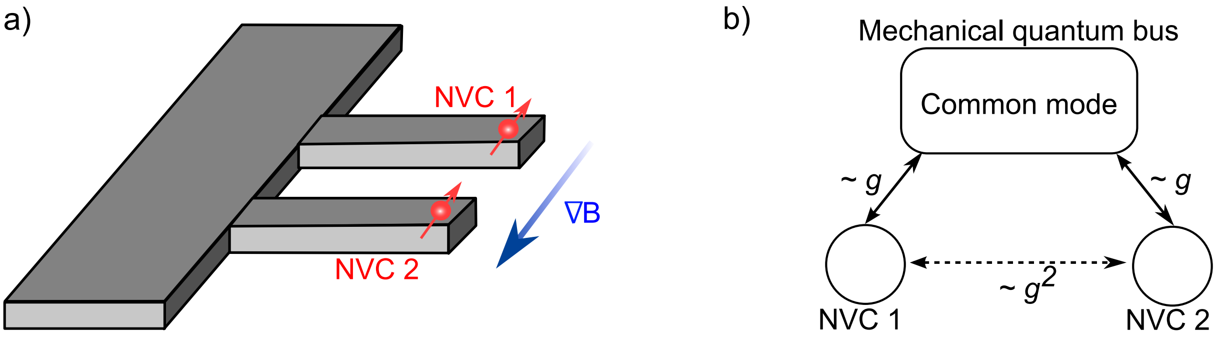

Figure 4.16.: (a) Two NVCs are located each at the extremity of two separated cantilevers which are mechanically coupled to each other. Based on the mechanical coupling of these two cantilevers, they show common mechanical modes. Applying an identical magnetic field gradient to both of these NVCs, due to their location, they feel the same vibrational behavior and hence, spin-phonon coupling strength. Thereupon, although these two cantilevers are separated from each other and can be addressed, initialized, and readout separately, they can be coupled through the common modes featuring a mechanical quantum bus. (b) As mentioned in the main text, the spin-phonon interaction (g), i.e. the coupling strength between each NVC spin and the common mechanical mode phonons (g) play a crucial role, since the indirect coupling strength of two separated NVCs through the mechanical mode as the quantum bus is dependent on g^2.

the same goal, coupling of distant NVCs has been also under notable research interest in last years. Although coupling of two NVCs within few nanometer distance has been successfully performed via magnetic dipolar interaction [39, 48], this does not seem to be feasible when the NVCs get separated from each other more than few tens of nanometer. To tackle this deficiency, several alternative proposals have been made by defining different platforms. For instance, proposals on magnetic ordering of distant NVCs [157], or coupling of distant NVCs by means of NEMS arrays [151] have been presented.

In this part, coupling of two distant NVCs (distance $\sim \mu$m) via a common mechanical mode is discussed (see Figure 4.16-(a)). This layout can be seen as two NVCs each located at the extremity of two coupled identical diamond microcantilevers, that are sharing common mechanical modes. A strong magnetic field gradient ($\nabla B \sim 10^6$ T/m), e.g. induced by a magnetized tip, is identically applied to these two NVCs. Since they are located both at the extremities of two individual cantilevers, two main advantages arise. i) They feel the same vibrational behavior with respect to the magnetized tip and hence undergo the similar spin-phonon interaction. ii) These two NVCs can be individually addressed, initialized, and readout, while they are coupled to each other via the common modes of the coupled microcantilevers. This platform based on the common modes of two coupled diamond cantilevers is then seen as a quantum bus, which can be scaled up to more than two cantilevers in a similar way. Within such a framework, Hamiltonian of the system composed of two distant NVCs as two qubits which are to be coupled via a common mechanical mode with frequency of ω can be written as [158]:

$$H = \hbar\omega a^{\dagger}a + \hbar g\left(\sigma_{1z} + \sigma_{2z}\right)\left(a^{\dagger} + a\right), \tag{4.27}$$

in which bosonic operators are shown with a and $a^{\dagger}$, σ_{iz} is the Pauli spin operator (z component) of the ith qubit, and g is the coupling constant between the oscillator and the qubit. For such a system, the indirect (mediated by the mechanical oscillator) two-qubit coupling constant is scaled with $\hbar g^2/\omega$ [158] (see Figure 4.16-(b)), which requires a strong spin-phonon coupling in comparison to the dephasing rates of the qubit and the mechanical oscillator. In the following, the spin-phonon coupling for NVC-microcantilever system will be analytically discussed, then a review of the coupled mechanical oscillators will be given, and finally initial demonstration including fabrication and characterization of the planned quantum bus structure will be presented.

As discussed at the beginning of this chapter, the spin-phonon coupling regime can be realized via strain coupling or magnetic field gradient. Assuming the fundamental mode of a cantilever hosting an NVC at its joint point, where the strain is at its maximum value, the stress-mediated spin-phonon coupling can be obtained via $g = \frac{\partial En(x=0)}{\partial z} \cdot z_{\mathrm{ZPF}}$ (En denotes the energy eigenvalue) [102]. By substituting each quantity by material- and geometry-dependent parameters and only considering the strain-induced longitudinal frequency shift, the resulting spin-phonon coupling constant (g) can be derived as:

$$g = \eta A\left(\frac{E^3}{\rho}\right)^{\frac{1}{4}}\left(\frac{1}{l^3 d}\right)^{\frac{1}{2}}, \tag{4.28}$$

in which η is a numerical constant, A is the longitudinal spin-stress coupling constant, E and ρ are the diamond Young's modulus and density, and l and d are the dimensions of the cantilever, respectively (see Figure 4.15-(a)). With respect to Eq. (4.28), to achieve a higher spin-phonon coupling constant, the miniaturization of the cantilever should be addressed. Recently by developing such cantilevers, NVC spin-phonon coupling constants up to $\sim$ 2 Hz could be obtained [114], whereas the further size shrinking is challenging and most likely degrades the NVC spin properties. Therefore, to achieve higher spin-phonon coupling strength which can pave the way toward realization of two coupled distant NVCs, one should consider alternative method e.g. spin-phonon coupling via an applied magnetic field gradient. For instance, a diamond cantilever with dimensions of (20,1,0.2) μm as the length, width, and thickness, respectively, has angular resonance frequency of $\approx$ 10 MHz and zero-point fluctuation of $\sim 10^{-14}$ m. By applying a magnetic field gradient of 20 G/nm to the NVC located at its extremity, the spin-phonon coupling strength of $\sim$ 2 kHz is consequently achievable [159].

Coupled mechanical oscillators are well-known objects in classical mechanics which have

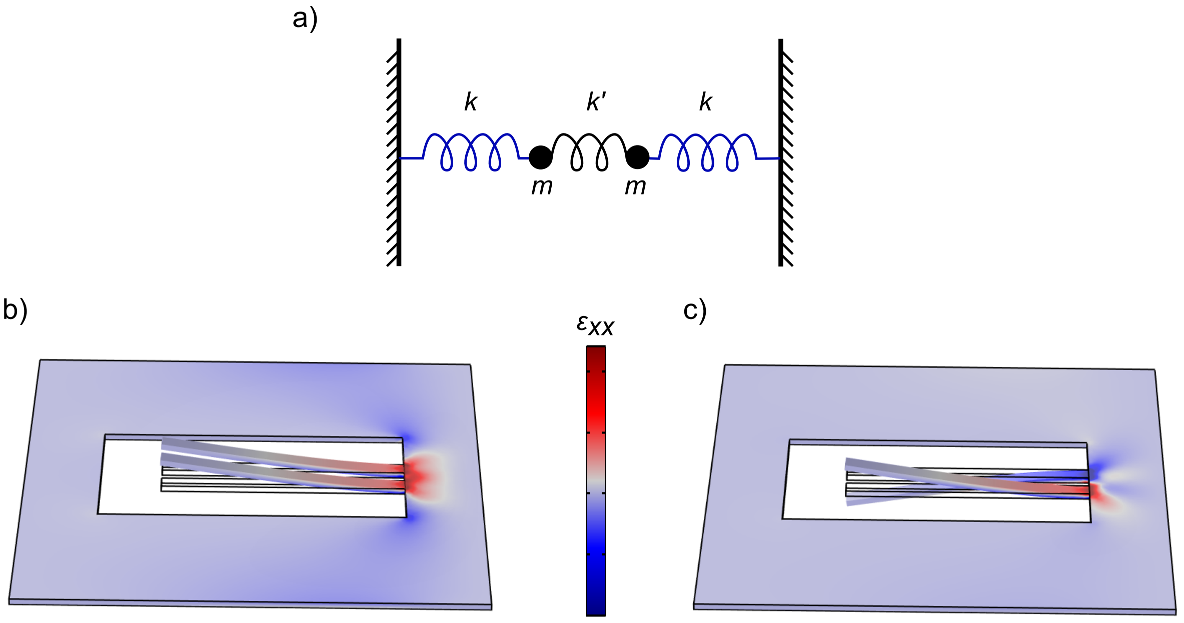

Figure 4.17.: Scheme of two coupled damped mechanical oscillators is depicted. (a) Shows two masses each connected to a spring associated with spring constant k, while these two are connected together by spring constant k'. (b) and (c) present FEM simulated strain (ε_{XX}) distribution in coupled modes for two cantilevers with length, width, and thickness, of 80, 5, and 2 μm, respectively, that are separated for 5 μm from each other. As depicted, the first coupled mode shows symmetric deflection behavior (b) whereas the second mode show asymmetric behavior (c).

been analytically discussed, and also realized [160, 161] for different applications such as ultra-sensitive mass sensing [162]. This system can be seen schematically in Figure 4.17-(a) as two identical oscillators with the identical mass of m, that are clamped with equal spring constants of k, which are additionally coupled together via another spring with the spring constant k'. Damping of these masses is assumed to be proportional to their velocity. Therefore, the valid Newton's law for the motion of these two oscillators associated with displacement variables x_1 and x_2 is given by:

$$m\ddot{x}_1 = -kx_1 - k'(x_1 - x_2) - b\dot{x}_1 + F_d\cos(\Omega t), \tag{4.29}$$

$$m\ddot{x}_2 = -kx_2 - k'(x_2 - x_1) - b\dot{x}_2, \tag{4.30}$$

where b is the damping constant. In the above-mentioned formulation, it is assumed that a time-dependent force (F_d cos (Ωt)) is applied only to one mass. The other alternatives such as forces applied on both masses is not assumed here, however it does not reject the main conclusion here. By adding and subtracting Eqs. (4.29) and (4.30), Newton's equations for

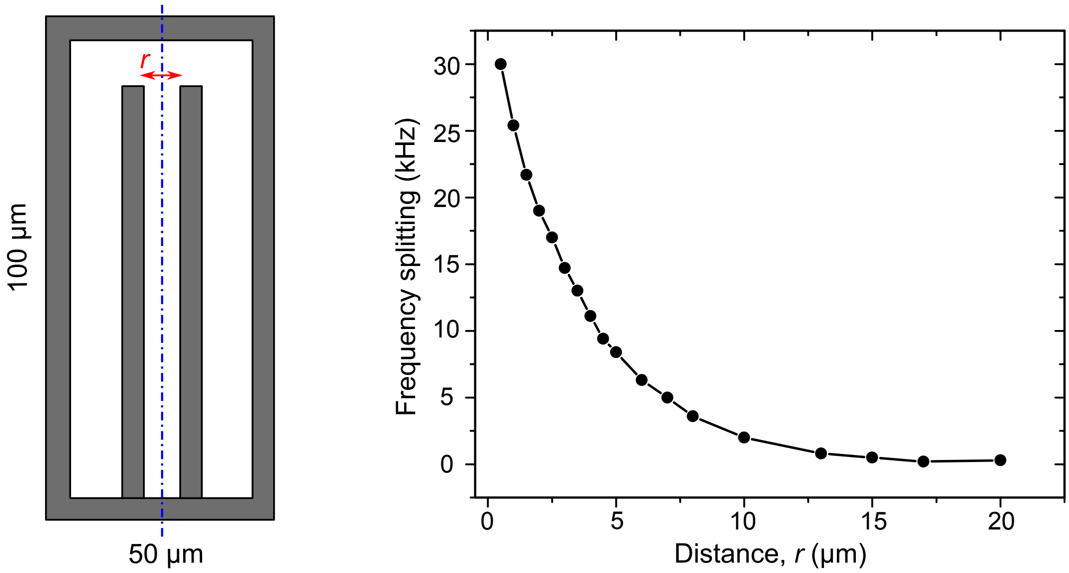

Figure 4.18.: (a) Scheme of the coupled cantilevers used in the FEM simulation is depicted, where the outer edge of the shown picture is mechanically constrained. In this simulation, the geometry is fixed, only the distance (r) between two cantilevers is swept symmetrically with respect to the whole geometry (blue dashed line). (b) The FEM simulation result on the effect of the distance between two cantilevers on the common modes frequency difference is presented. As can be seen, the splitting between these two resonance frequencies increase as the distance between the two cantilevers decrease.

two different coupled modes will be obtained:

$$\ddot{x}_s + \gamma \dot{x}_s + \omega_s^2 x_s = F\cos(\Omega t), \tag{4.31}$$

$$\ddot{x}_f + \gamma \dot{x}_f + \omega_f^2 x_f = F\cos(\Omega t), \tag{4.32}$$

in which $x_s \equiv x_1 + x_2$ and $x_f \equiv x_1 - x_2$ are the displacement of coupled slow and fast modes, respectively, and γ and F are defined as b/m and F_d/m, respectively. The corresponding resonance frequencies for these two modes are then given by $\omega_s \equiv \sqrt{\frac{k}{m}}$ (identical to the single oscillator case) and $\omega_f \equiv \sqrt{\frac{k+2k'}{m}}$, respectively.

To realize the above-mentioned mechanically-coupled harmonic oscillators, two identical microcantilevers located close to each other (distance $\sim$ μm) are aimed [163]. These cantilevers can be structured inside a window etched through the diamond thin film. These two mechanically-coupled microcantilevers are simulated by means of FEM software. As shown in Figure 4.17, two symmetric and asymmetric vibrational modes occur as the first two common modes of the mechanically-coupled cantilevers, which correspond to the slow and fast modes explained in Eqs. (4.31) and (4.32), respectively. To investigate the effect of the geometry on these two common modes, two identical diamond cantilevers with dimensions of

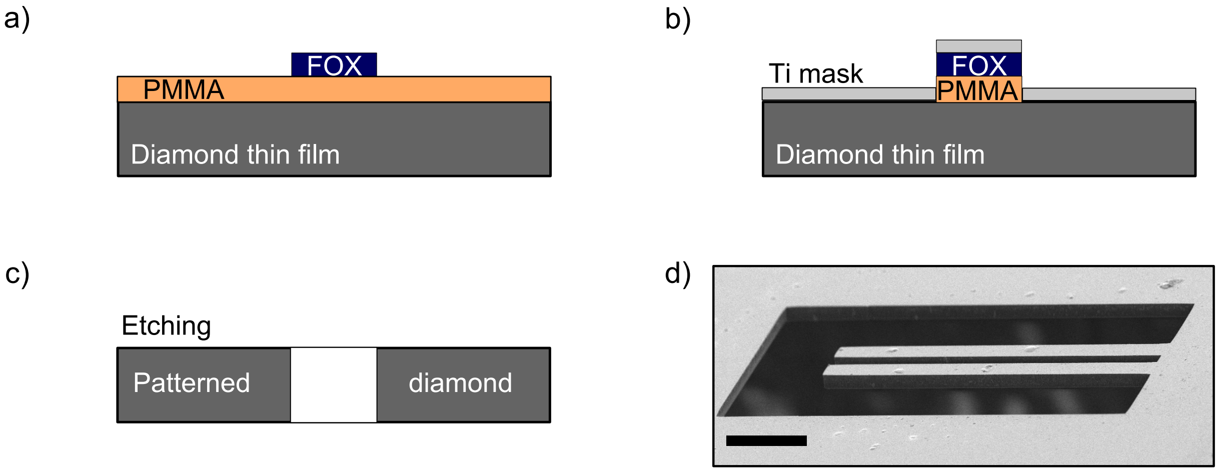

Figure 4.19.: Realization of mechanically-coupled diamond microcantilevers is schematically demonstrated. (a) A thin diamond film is produced as the starting point, then PMMA and FOX 25 resists are spin coated on it, followed by e-beam lithography process of FOX 25 resist. The designed layout to expose the FOX 25 resist is indeed not the desired structure geometry, but its inverted geometry. This makes the exposure time much shorter in comparison to the ordinary case. (b) The PMMA layer is etched through by means of O_2 etching plasma, then 150 nm of Ti is deposited via thermal evaporation technique. (c) After preparing the Ti mask, the diamond film is etched using O_2 RIE-ICP plasma recipe. At the end, SF_6-CF_4 RIE-ICP step is applied to remove the residual of the Ti mask. (d) shows an SEM image of one of the resulting mechanically-coupled microcantilevers. Scale bar denotes 20 μm.

90 μm, 5 μm, and 2.8 μm as their length, width, and thickness are considered (see Figure 4.18-(a)). These dimensions are chosen i) since it yields to an angular resonance frequency of $\sim 2\pi \times 1$ MHz and ii) for the sake of simplification in the required fabrication technique. As shown in Figure 4.18-(b), FEM simulations show that the coupling parameter of these two cantilevers and hence, the splitting between the two common mechanical modes increases as two cantilevers get closer to each other.

4.3.3. Fabrication procedure

To fabricate the targeted platform, similar to the fabrication of the thin circular diamond membrane, a thin diamond film with thickness of $\sim$ 30 μm is used. This film is glued on top of another diamond for structural support (type-I diamond, refer to chapter 1 to see different types of diamond) by means of EPO-TEK 353ND epoxy. By using the Ar/SF_6 etching recipe, it is thinned down to a thickness of 2-5 μm. Then, e-beam lithography process is performed on a FOX 25 resist on top of the spin-coated PMMA layer (double resist layer of PMMA-FOX 25). In this process, the inverted layout to the final desired structure is written on FOX 25 resist. Afterward, the PMMA layer is etched by means of anisotropic O_2

plasma; 30 W RIE with no ICP process, and 30 sccm of O_2 flow rate with 10 mTorr pressure. The main point here is etching through the PMMA layer completely while minimizing the heating side effect which can displace and degrade the FOX 25 mask. After removal of the PMMA layer, $\approx$ 150 nm of Ti is deposited via thermal evaporation technique (P$< 5\times10^{-6}$ mbar, deposition rate $\leq$ 0.5 Å). It should be noted that the vacuum condition of the deposition chamber and the employed deposition rate play vital roles, since they strongly affect the quality of the Ti layer as etching mask. Next, the lift-off process is accomplished to remove the PMMA layer underneath the FOX 25 mask by leaving the sample inside NEP solution for $\sim$ 1 hour. This consequently gives the final Ti mask which is identical to the desired coupled cantilever geometry. The explained e-beam lithography process based on double-layer resist is well-known in semiconductor technology mainly due to its very good reproducibility and high resolution [52]. However, the main purpose of its usage here is to drastically reduce the electron beam exposure time. As the last stage, the etching process is utilized to transfer the cantilever geometry by etching through the area between the neighbor ones. This etching step is similar to the one used for nanopillar fabrication. The scheme of the applied fabrication technique is illustrated in Figures 4.19-(a) to (c). The SEM image of one of the final geometry of mechanically-coupled cantilevers is given in Figure 4.19-(d).

4.3.4. Experimental characterization

One of the fabricated chips has several windows in which two identical cantilevers, with the approximate length, width, and thickness of 90 μm, 4 μm, and 2 μm, respectively, are separated from each other by 2 μm (see Figure 4.20-(a)). To characterize the developed mechanically-coupled cantilever geometry, it is installed on a glass holder with a central hole (to avoid the mechanical contact), then on top of a piezo chip. The whole device is then mounted in a confocal setup, as illustrated before. Similar to the related measurements of the circular membrane geometry, the fluorescence count rate collected from the extremity of the cantilevers is monitored while the piezo chip frequency is swept. As can be seen in Figure 4.20-(b), two dips are observed which predicate resonance frequencies $\omega_1 = 2\pi\times$ 934$\pm$0.5 kHz and $\omega_2 = 2\pi\times$ 940$\pm$0.33 kHz with FWHM of 5.3 kHz and 3.8 kHz, respectively, (see Figure 4.20-(b)) which correspond to Q factors of approximately 176 and 247, respectively. This experimentally-achieved frequency splitting is smaller in comparison to the FEM simulation results presented in Figure (4.18). This can be mainly due to different clamping condition in experiment compared to simulation. Different installation (and hence clamping) of the chip is observed to manipulate the behavior of the system.

Considering the f_1 resonance frequency, the thickness is estimated to be $\approx$ 2.5 μm, which matches the measured value by optical microscope during the fabrication process. As discussed in Eqs. (4.31) and (4.32), these two resonance frequencies present two different fast (asymmetric) and slow (symmetric) modes of the coupled cantilevers. Given these two resonance frequencies, based on Eqs. (4.31), (4.32), and Figure 4.17 and by using Taylor expansion, $\frac{k'}{k} \approx 6.5 \times 10^{-3}$ is calculated. This value can be enhanced e.g. by fabricating the cantilevers closer to each other (see Figure 4.18-(b)). The achieved Q factors are comparable to the former reported values under ambient condition [120], which can be further augmented e.g. in vacuum condition [104].

To prove the achieved data and hence the concept of mechanically-coupled cantilevers, one of the cantilevers is then broken and removed (see Figure 4.20-(c)). Afterward, the sample is characterized in a same way. This time only one dip is observed (see Figure 4.20-(d)), which is located at $\omega_1' = 2\pi \times 968 \pm 0.33$ kHz with the corresponding FWHM of $\approx$ 3 kHz, that yields in approximate Q factor of 322. Based on analytical calculations derived from Eqs. (4.31) and (4.32), this dip nominally should be located in a same frequency as the ω_1 of the double cantilevers. However, a minor displacement ($\approx$ 3 %) is observed, which can be attributed to the stress which is applied to the cantilever during the breaking process. This manifests as the residual stress of the cantilever which can affect its resonance frequency [127].

The geometry of the presented microcantilevers can be modified such, that it brings an increase in the ZPF and hence the spin-phonon coupling parameter. This can be accomplished e.g. by etching through the center of the presented microcantilevers, i.e. embedding a groove in them. In this way, their resonance frequencies do not change visibly (based on FEM simulations), whereas their masses are notably reduced. An example of this modified geometry can be seen in Figure 4.21. For instance, $\approx$ 12 % increase in the ZPF of these modified microcantilevers is calculated (using Eq. (4.7)), in comparison to those with no modification. By applying a similar fabrication procedure, modified microcantilevers with $\sim$ 20 % larger ZPF are feasible, with no further fragility.

4.4. Summary and outlook

In this chapter, first an introductory information is given on different mechanical degrees of freedom, mechanical oscillators, mechanical properties of diamond, and different ways of spin-phonon interaction based on the NVC spin interface. Then, a novel versatile hybrid system based on a thin circular single-crystal diamond membrane with diameter and thickness of $\approx$ 1.1 mm and 1.2 μm, respectively, and embedded single NVCs is demonstrated. A certain etching technique is developed which is key to producing this hybrid device. Within this architecture, NVCs are used as nanoscale probes to detect the membrane motion in DC and AC regimes, as well as the residual stress of the structure. Theoretical calculations are provided

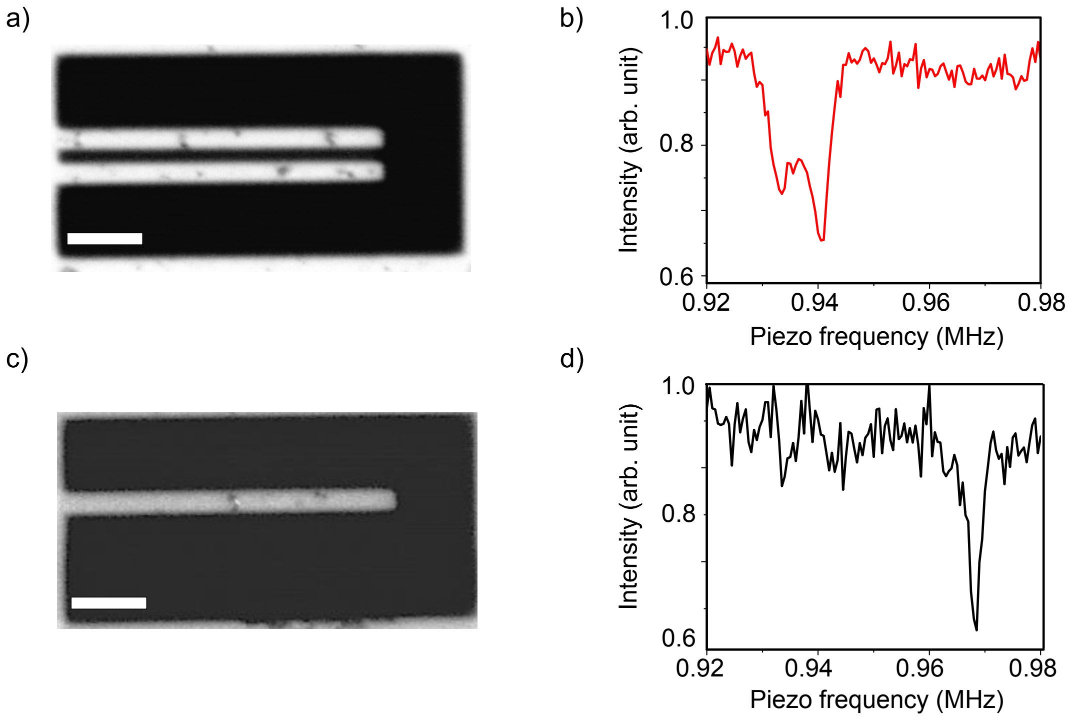

Figure 4.20.: (a) Optical image of mechanically-coupled cantilevers is shown. (b) These two dips show two different resonance frequencies of the fast and slow modes of mechanically-coupled cantilevers. To prove the validity of the statement about realization and observation of coupled cantilevers, one of these two cantilevers is broken (c). Then as shown in (d), only one resonance frequency is observable. Scale bars in (a) and (c) present 20 μm.

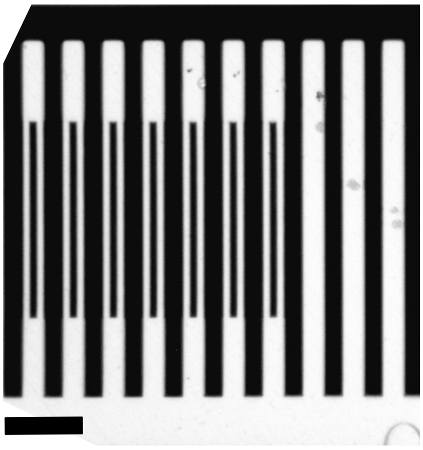

Figure 4.21.: Modified geometry of the microcantilevers is shown (left side). In this way, center of these microcantilevers is etched through. In comparison to the ordinary geometry (right side), they can yield in larger ZPF and consequently larger spin-phonon coupling parameter. Scale bar shows 20 μm.

which support the achieved experimental observations via NVC nanoprobes. Spin-phonon coupling interaction via magnetic field gradient is further explored in this system. Based on provided analytical calculations, this interaction seems to be more effective, when the dimensions of the membrane are reduced. Overall, the presented results promote the potential of diamond quantum hybrid systems to achieve high sensitivity and spatial resolution in piezometry and vibrometry applications. Similarly, such a hybrid system can be exploited further in optomechanical cavities [164]. Within the presented experiments, the ground-state of single NVCs is focused; however, one can additionally benefit from the controllable stress in the demonstrated system to manipulate [116] the excited-state fine structure of NVCs [23].

After developing a single hybrid module, in which the effect of mechanical degrees of freedom of a single mechanical object (membrane) on an embedded isolated NVC is studied, scaling up these modules is targeted. In section 4.3, an array of diamond microcantilevers is discussed. First, a brief review from continuum mechanics is given about cantilevers. Then, double mechanically-coupled microcantilevers are suggested as quantum bus to couple distant NVCs. Preliminary analytical and numerical calculations are presented to assess this structure for the mentioned purpose. Then, the fabrication procedure is introduced to realize these structures. By characterizing such a structure, the coupled and uncoupled frequency eigenmodes, corresponding quality factors, and mechanical coupling parameter are revealed.

The hybrid systems in this chapter include two main subsystems; NVC and mechanical objects. As previously described, the interaction between these two subsystems is of the dispersive form of $\hbar g(a+a^{\dagger})\sigma_z$, in which the dependency of the spin state on the state of the mechanical object is revealed.

Recently, cooling the mechanical motion of mechanical oscillators by dissipative two-level systems, e.g. NVCs, is proposed [165]. In this proposal a driving MW field in the form of $\frac{\hbar\Omega}{2}\sigma_x$ (Ω is the Rabi frequency of the two-level system) is added into the model, which enables the resonant coupling regime. To realize this regime, the coupling strength between the mechanical system and the NVC should be adequate enough to allow energy transfer between them. Considering this model, two main challenges might arise. i) First, to realize this system, strong spin-phonon coupling and low dissipation rate of the mechanical oscillator are required ($g > \omega/Q$) [166], which is still cumbersome to realize. ii) Second, to further control the state of the mechanical oscillator by this method, e.g. to perform cooling of it, this type of cooling requires many cooling cycles, i.e. many control pulses to go to much lower phonon occupation numbers. Applying large number of control pulses however might not be feasible due to the limited coherence time of the embedded NVCs.

An alternative to this case, can be again the dispersive coupling form of NVC and the mechanical oscillator, however by applying heralded control of the mechanical motion by means of the NVC spin [159]. Through this technique, successive projections of the NVC spin to a specific state allows cooling down the motional degree of freedom via filtering unwanted thermal states of the cantilever. A key advantage of this technique is that, it even works for weak spin-phonon coupling [159]. In this way, the resulting cooling rate is surprisingly dependent on the instantaneous thermal occupation number, i.e. higher temperatures even yield in higher cooling rates.

A. Measurement Setup

The developed measurement setup is demonstrated in this appendix. This setup is a home-built confocal optical arrangement equipped with optical and microwave (MW) pulses, working under ambient temperature and pressure. This setup will be explained in three steps. First, the confocal part will be shortly presented. Second, the electronic and MW part will be briefly illustrated. Third, the employed sample holder under an applied magnetic field will be shown.

i) Confocal part: To address the spatially-isolated NVCs in diamond, by performing the optical pumping and readout of them, a confocal setup is built. The sketch of this setup is depicted in Figure A.1. This setup is equipped with a diode pumped solid-state (DPSS) 532 nm laser (power $\approx$ 500 mW). Its Gaussian-profile output beam is passed through (focused by L1, L2, and L3 lenses) two cascaded acousto-optic modulators (AOMs) for generating optical pulses with very high extinction ratio. Then, this beam is focused by L4 lens to another one (in-coupler) which is guided to the out-coupler lens by means of a single-mode fiber (SMF). This fiber is used to spatially filter the non-Gaussian output beam of the AOMs to Gaussian mode again. The explained setup so far is part of the pumping unit. The power fluctuation of the output beam in this configuration is $\sim$ 3 %.

The output beam is steered to a dichroic mirror (DM) from which is reflected to the objective lens (NA = 0.95). The delivered laser power behind the objective lens can be up to 5 mW. The objective lens is positioned on top of a closed-loop XYZ piezo stage with traveling range of 100 μm $\times$ 100 μm $\times$ 20 μm. The sample is mounted on top of a sample holder which is fixed on a XYZ manual stage. This manual stage is used to align the sample roughly in the focus of the objective lens. The piezo stage positions the objective lens precisely such that the laser beam is focused on the sample. The reflected beam from the sample goes back via the same path through the objective lens, passes the DM and enters the detection unit. The DM is capable of reflecting the green beam with more than 90% reflectivity, where it transmits the emission of the NVC, instead. The reflected beam is focused by L5 lens onto a pinhole (PH) with aperture size of 50 μm. The size of this pinhole is selected based on the numerical aperture of the objective lens and also the focal length of L5 [75]. Afterward, a long-pass optical filter (LPF: 650 nm long-pass) is aligned to spectrally filter the phonon sideband of the NVC emitted photons. The pinhole is imaged by a $2f-2f$ arrangement to the photodetectors (f is the focal length of L6). To count the photons emitted by the NVC, which are collected

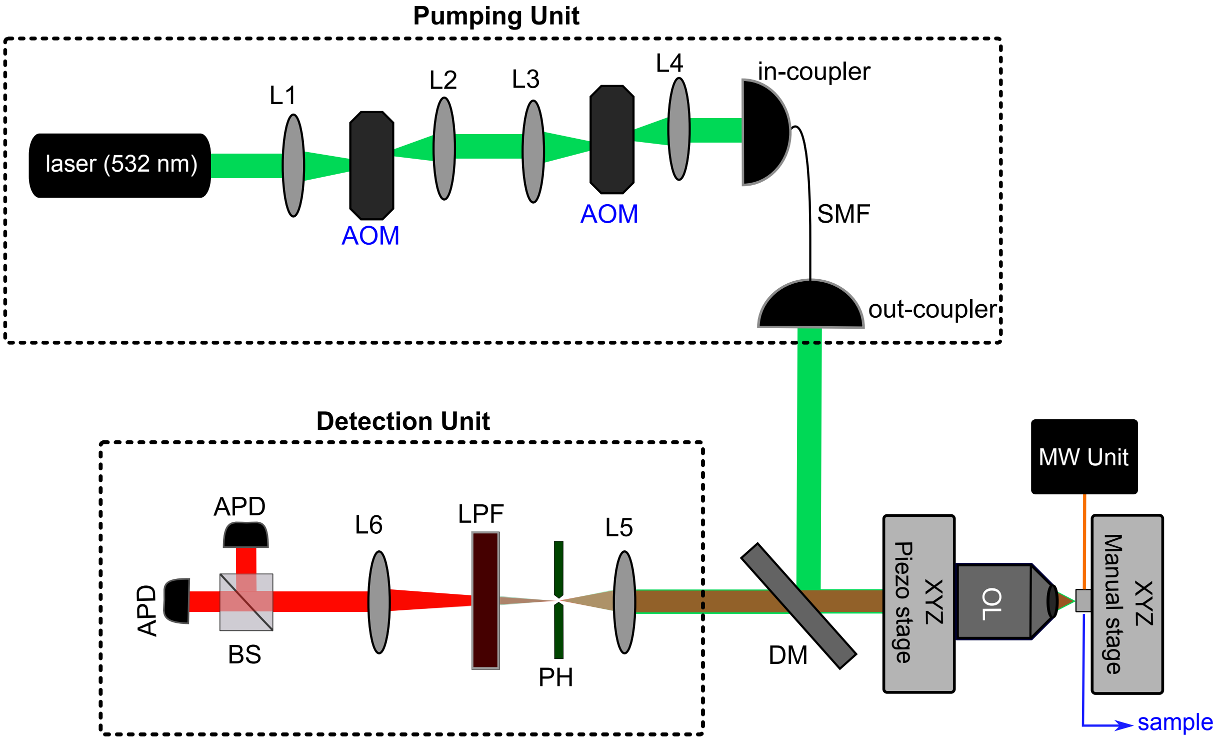

Figure A.1.: Sketch of the developed confocal setup is demonstrated.

so far, two avalanche photodiodes (APDs) as photodetectors are used in Hanbury Brown and Twiss (HBT) configuration. To split the collected beam equally onto these two APDs, a non-polarizing beam splitter (BS) is used.

ii) Electronic and MW part: To produce the desired MW frequency and power, and generally to perform the confocal scanning, CW and pulsed optical and MW measurements, several units are exploited in the measurement setup. The sketch of the electronic and MW units is illustrated in Figure A.2.

The microwaves are synthesized by the MW source (frequency generator), which are then split to two equal-power outputs, however with 90° phase shift. This is of crucial importance for the dynamical decoupling measurements (see chapter 3). Each output intensity is controlled by MW switches, governed by the FPGA unit. Then, these two outputs are combined again, amplified and sent to the sample holder. To avoid back reflection from the sample holder to the amplifier, a MW circulator is embedded between the amplifier and the sample holder. By means of these equipments, CW and pulsed microwaves with power of ≈ 1 W (in case of pulsed: with durations down to ~ 50 ns) can be applied to the targeted NVC.

To perform the measurements, data acquisition unit (DAQ) from National Instruments (NI) and FPGA units are utilized. NI DAQ unit is used to control the XYZ piezo stage, to count the detected photons by APDs, and also to control the MW source, all in a synchronized way. For

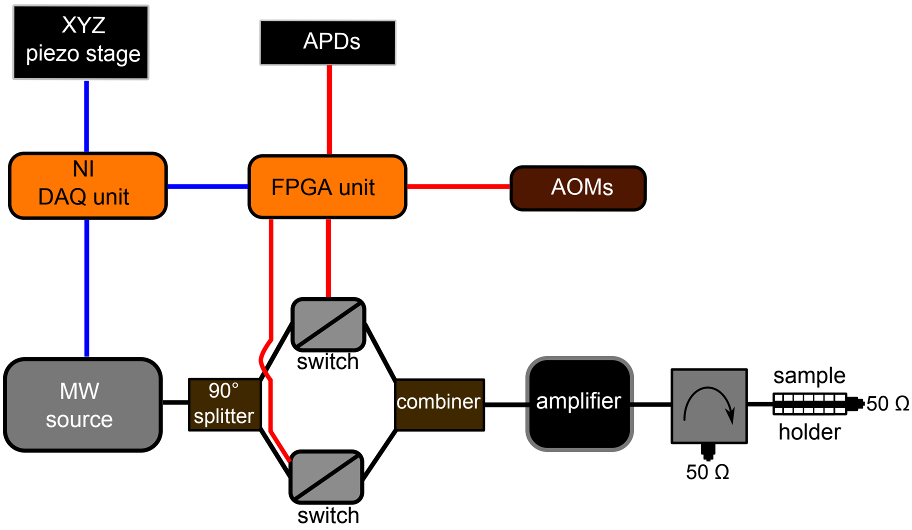

Figure A.2.: The electronic and MW parts of the measurement setup are demonstrated.

example, confocal scanning and ODMR measurements are accomplished based on this unit. To generate optical and microwave pulses and also to acquire the photons in a synchronized way, thus to be able to perform Rabi, Hahn echo, dynamical decoupling measurements, etc, two FPGA units are used. These FPGA units are acting as pulse generators and time taggers. These FPGAs govern the APDs, AOMs, and MW switches. With the aid of these units, pulsed measurements with the time resolution of sub-nanosecond is feasible. The whole hardware involved in the measurements are controlled by a PC with a software written in Python programming language.

ii) Sample holder: The exploited sample holder in this thesis is a printed circuit board (PCB) with a MW structure to which two SMA connectors are connected. This MW structure is designed to show 50 Ω impedance at 3 GHz frequency. Possibilities of applying gas pressure, and vibrations via the piezo chip to the diamond sample are embedded on this sample holder (see chapter 4).

To apply static magnetic fields to the NVCs, a permanent magnet from Neodymium-Iron-Boron (NdFeB) is mounted on another XYZ manual stage by which the magnetic field can be aligned precisely to the axis of the desired NVC. The whole arrangement shows maximum 1 μm drift for the NVC in the confocal scan, and $\ll 1$ % drift in the applied magnetic field at the location of the NVC, over the course of 12 hours.

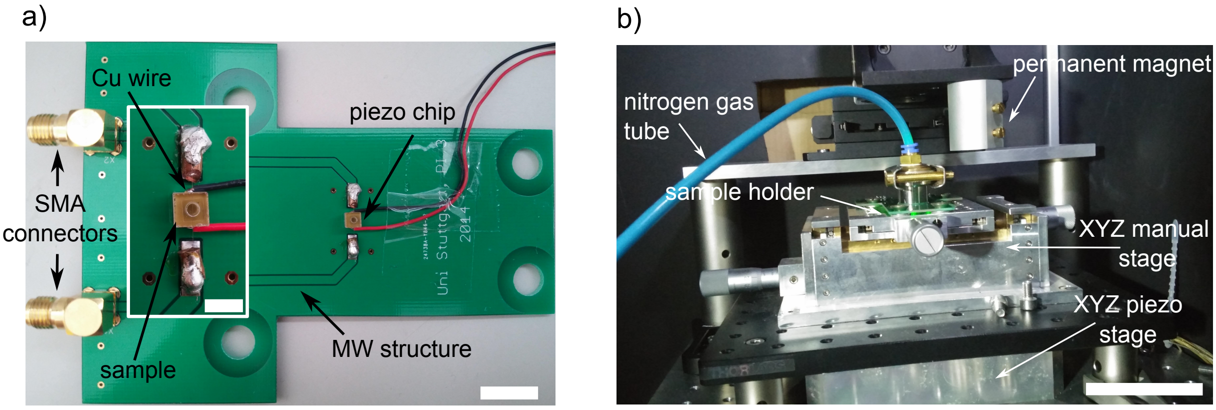
a)
Cu wire
SMA
connectors
sample
piezo chip
MW structure
b)
permanent magnet
nitrogen gas
tube
sample holder
XYZ manual
stage
XYZ piezo
stage

Figure A.3.: Figures of the designed sample holder and the mechanical mounting of the sample and the magnet are depicted. The scale bar in Figure (a)-main shows 2 cm, 5 mm in its inset, and 5 cm in Figure (b).

Bibliography

[1] Sussmann, R. S. *CVD Diamond for Electronic Devices and Sensors* (WILEY, 2009).

[2] Treasury of National Jewels, link = `http://www.cbi.ir/page/2091.aspx`, last checked = Accessed: 23.12.2016.

[3] Wur, D. R., Davidson, J. L., Kang, W. P. & Kinser, D. L. Polycrystalline diamond pressure sensor. *Journal of Microelectromechanical Systems* **4**, 34–41 (1995).

[4] Janssens, S. D., Drijkoningen, S. & Haenen, K. Ultra-thin nanocrystalline diamond membranes as pressure sensors for harsh environments. *Applied Physics Letters* **104**, 073107 (2014). URL `http://aip.scitation.org/doi/abs/10.1063/1.4866028`. `http://aip.scitation.org/doi/pdf/10.1063/1.4866028`.

[5] Zaitsev, A. M. *Optical Properties of Diamond; A Data Handbook* (Springer, 2001).

[6] Zaitsev, A. M. Vibronic spectra of impurity-related optical centers in diamond. *Phys. Rev. B* **61**, 12909–12922 (2000). URL `http://link.aps.org/doi/10.1103/PhysRevB.61.12909`.

[7] Jelezko, F. & Wrachtrup, J. Single defect centres in diamond: A review. *physica status solidi (a)* **203**, 3207–3225 (2006). URL `http://dx.doi.org/10.1002/pssa.200671403`.

[8] Hepp, C. *et al.* Electronic structure of the silicon vacancy color center in diamond. *Phys. Rev. Lett.* **112**, 036405 (2014). URL `http://link.aps.org/doi/10.1103/PhysRevLett.112.036405`.

[9] Balmer, R. S. *et al.* Chemical vapour deposition synthetic diamond: materials, technology and applications. *Journal of Physics: Condensed Matter* **21**, 364221 (2009). URL `http://stacks.iop.org/0953-8984/21/i=36/a=364221`.

[10] Dean, P. J., Lightowlers, E. C. & Wight, D. R. Intrinsic and extrinsic recombination radiation from natural and synthetic aluminum-doped diamond. *Phys. Rev.* **140**, A352–

A368 (1965). URL `http://link.aps.org/doi/10.1103/PhysRev.140.A352`.

[11] Aharonovich, I., Greentree, A. D. & Prawer, S. Diamond photonics. *Nat Photon* **5**, 397–405 (2011). URL `http://dx.doi.org/10.1038/nphoton.2011.54`.

[12] Bundy, F. P. Direct conversion of graphite to diamond in static pressure apparatus. *The Journal of Chemical Physics* **38**, 631–643 (1963). URL `http://aip.scitation.org/doi/abs/10.1063/1.1733716`. `http://aip.scitation.org/doi/pdf/10.1063/1.1733716`.

[13] Sumiya, H., Toda, N. & Satoh, S. Growth rate of high-quality large diamond crystals. *Journal of Crystal Growth* **237-239, Part 2**, 1281 – 1285 (2002). URL `http://www.sciencedirect.com/science/article/pii/S0022024801021455`. The thirteenth international conference on Crystal Growth in conjunction with the eleventh international conference on Vapor Growth and Epitaxy.

[14] Balasubramanian, G. *et al.* Ultralong spin coherence time in isotopically engineered diamond. *Nat Mater* **8**, 383–387 (2009). URL `http://dx.doi.org/10.1038/nmat2420`.

[15] Obraztsov, A. N. *et al.* Single crystal diamond tips for scanning probe microscopy. *Review of Scientific Instruments* **81**, 013703 (2010). URL `http://aip.scitation.org/doi/abs/10.1063/1.3280182`. `http://aip.scitation.org/doi/pdf/10.1063/1.3280182`.

[16] Yuan, G. *et al.* Growth of diamond on silicon tips. *Journal of Crystal Growth* **186**, 382 – 385 (1998). URL `http://www.sciencedirect.com/science/article/pii/S0022024897005204`.

[17] Element Six, link = `https://e6cvd.com/`, last checked = Accessed: 24.12.2016.

[18] Barnes, W. L. *et al.* Solid-state single photon sources: light collection strategies. *Eur. Phys. J. D* **18**, 197–210 (2002). URL `http://dx.doi.org/10.1140/epjd/e20020024`.

[19] Rogers, L. J. *et al.* All-optical initialization, readout, and coherent preparation of single silicon-vacancy spins in diamond. *Phys. Rev. Lett.* **113**, 263602 (2014). URL `http://link.aps.org/doi/10.1103/PhysRevLett.113.263602`.

[20] Schirhagl, R., Chang, K., Loretz, M. & Degen, C. L. Nitrogen-vacancy centers in diamond: Nanoscale sensors for physics and biology. *Annual Review of Physical Chemistry* **65**, 83–105 (2014). URL `http://dx.doi.org/10.1146/annurev-physchem-040513-103659`. PMID: 24274702, `http://dx.doi.org/10.1146/annurev-physchem-040513-103659`.

[21] Gruber, A. *et al.* Scanning confocal optical microscopy and magnetic resonance on single defect centers. *Science* **276**, 2012–2014 (1997). URL `http://science.sciencemag.org/content/276/5321/2012`. `http://science.sciencemag.org/content/276/5321/2012.full.pdf`.

[22] Neumann, P. *et al.* Excited-state spectroscopy of single nv defects in diamond using optically detected magnetic resonance. *New Journal of Physics* **11**, 013017 (2009). URL `http://stacks.iop.org/1367-2630/11/i=1/a=013017`.

[23] Batalov, A. *et al.* Low temperature studies of the excited-state structure of negatively charged nitrogen-vacancy color centers in diamond. *Phys. Rev. Lett.* **102**, 195506 (2009). URL `http://link.aps.org/doi/10.1103/PhysRevLett.102.195506`.

[24] Ofori-Okai, B. K. *et al.* Spin properties of very shallow nitrogen vacancy defects in diamond. *Phys. Rev. B* **86**, 081406 (2012). URL `http://link.aps.org/doi/10.1103/PhysRevB.86.081406`.

[25] Fávaro de Oliveira, F. *et al.* Effect of low-damage inductively coupled plasma on shallow nitrogen-vacancy centers in diamond. *Applied Physics Letters* **107** (2015). URL `http://scitation.aip.org/content/aip/journal/apl/107/7/10.1063/1.4929356`.

[26] Fávaro de Oliveira, F. *et al.* Toward optimized surface δ-profiles of nitrogen-vacancy centers activated by helium irradiation in diamond. *Nano Letters* **16**, 2228–2233 (2016). URL `http://dx.doi.org/10.1021/acs.nanolett.5b04511`. PMID: 26938259, `http://dx.doi.org/10.1021/acs.nanolett.5b04511`.

[27] Siyushev, P. *et al.* Monolithic diamond optics for single photon detection. *Applied Physics Letters* **97**, 241902 (2010). URL `http://aip.scitation.org/doi/abs/10.1063/1.3519849`. `http://aip.scitation.org/doi/pdf/10.1063/1.3519849`.

[28] Jamali, M. *et al.* Microscopic diamond solid-immersion-lenses fabricated around single defect centers by focused ion beam milling. *Review of Scientific Instruments* **85**, 123703 (2014). URL `http://aip.scitation.org/doi/abs/10.1063/1.4902818`. `http://aip.scitation.org/doi/pdf/10.1063/1.4902818`.

[29] Babinec, T. M. *et al.* A diamond nanowire single-photon source. *Nat Nano* **5**, 195–199 (2010). URL `http://dx.doi.org/10.1038/nnano.2010.6`.

[30] Choy, J. T. *et al.* Enhanced single-photon emission from a diamond-silver aperture. *Nat Photon* **5**, 738–743 (2011). URL `http://dx.doi.org/10.1038/nphoton.2011.249`.

[31] Riedel, D. *et al.* Low-loss broadband antenna for efficient photon collection from a coherent spin in diamond. *Phys. Rev. Applied* **2**, 064011 (2014). URL `http://link.aps.org/doi/10.1103/PhysRevApplied.2.064011`.

[32] Li, L. *et al.* Efficient photon collection from a nitrogen vacancy center in a circular bullseye grating. *Nano Letters* **15**, 1493–1497 (2015). URL `http://dx.doi.org/10.1021/nl503451j`. PMID: 25714414, `http://dx.doi.org/10.1021/nl503451j`.

[33] Marseglia, L. *et al.* Nanofabricated solid immersion lenses registered to single emitters in diamond. *Applied Physics Letters* **98**, 133107 (2011). URL `http://aip.scitation.org/doi/abs/10.1063/1.3573870`. `http://aip.scitation.org/doi/pdf/10.1063/1.3573870`.

[34] Hausmann, B. J. *et al.* Fabrication of diamond nanowires for quantum information processing applications. *Diamond and Related Materials* **19**, 621 – 629 (2010). URL `http://www.sciencedirect.com/science/article/pii/S0925963510000312`. Proceedings of Diamond 2009, The 20th European Conference on Diamond, Diamond-Like Materials, Carbon Nanotubes and Nitrides, Part 1.

[35] Hausmann, B. J. M. *et al.* Single-color centers implanted in diamond nanostructures. *New Journal of Physics* **13**, 045004 (2011). URL `http://stacks.iop.org/1367-2630/13/i=4/a=045004`.

[36] Maletinsky, P. *et al.* A robust scanning diamond sensor for nanoscale imaging with single nitrogen-vacancy centres. *Nature Nanotechnology* **7**, 320–324 (2012). URL `doi:10.1038/nnano.2012.50`.

[37] Widmann, M. *et al.* Coherent control of single spins in silicon carbide at room temperature. *Nat Mater* **14**, 164–168 (2015). URL `http://dx.doi.org/10.1038/nmat4145`. Letter.

[38] Siyushev, P. *et al.* Coherent properties of single rare-earth spin qubits. *Nature Communications* **5**, 3895 EP – (2014). URL `http://dx.doi.org/10.1038/ncomms4895`. Article.

[39] Dolde, F. *et al.* Room-temperature entanglement between single defect spins in diamond. *Nat Phys* **9**, 139–143 (2013). URL `http://dx.doi.org/10.1038/nphys2545`.

[40] Waldherr, G. *et al.* Quantum error correction in a solid-state hybrid spin register. *Nature* **506**, 204–207 (2014). URL `http://dx.doi.org/10.1038/nature12919`. Letter.

[41] Yang, S. *et al.* High-fidelity transfer and storage of photon states in a single nuclear spin. *Nat Photon* **10**, 507–511 (2016). URL `http://dx.doi.org/10.1038/nphoton.2016.103`. Letter.

[42] Balasubramanian, G. *et al.* Nanoscale imaging magnetometry with diamond spins under ambient conditions. *Nature* **455**, 648–651 (2008). URL `http://www.nature.com/nature/journal/v455/n7213/suppinfo/nature07278_S1.html`.

[43] Dolde, F. *et al.* Electric-field sensing using single diamond spins. *Nat Phys* **7**, 459–463 (2011). URL `http://dx.doi.org/10.1038/nphys1969`.

[44] Neumann, P. *et al.* High-precision nanoscale temperature sensing using single defects in diamond. *Nano Letters* **13**, 2738–2742 (2013). URL `http://dx.doi.org/10.1021/nl401216y`. PMID: 23721106, `http://dx.doi.org/10.1021/nl401216y`.

[45] Lee, D., W. Lee, K., V. Cady, J., Ovartchaiyapong, P. & Bleszynski Jayich, A. C. Topical review: Spins and mechanics in diamond. *ARXIV* **xxx112**, xxx3866–3873 (2016). URL `http://www.pnas.org/content/112/13/3866.abstract`. `http://www.pnas.org/content/112/13/3866.full.pdf`.

[46] Maze, J. R. *et al.* Nanoscale magnetic sensing with an individual electronic spin in diamond. *Nature* **455**, 644–647 (2008). URL `http://dx.doi.org/10.1038/nature07279`.

[47] Hong, S. *et al.* Nanoscale magnetometry with nv centers in diamond. *MRS Bulletin* **38**, 155–161 (2013).

[48] Jakobi, I. *et al.* Efficient creation of dipolar coupled nitrogen-vacancy spin qubits in diamond. *Journal of Physics: Conference Series* **752**, 012001 (2016). URL `http://stacks.iop.org/1742-6596/752/i=1/a=012001`.

[49] Toyli, D. M., Weis, C. D., Fuchs, G. D., Schenkel, T. & Awschalom, D. D. Chip-scale nanofabrication of single spins and spin arrays in diamond. *Nano Letters* **10**, 3168–3172 (2010). URL `http://dx.doi.org/10.1021/nl102066q`. PMID: 20698632, `http://dx.doi.org/10.1021/nl102066q`.

[50] Burek, M. J. *et al.* Free-standing mechanical and photonic nanostructures in single-crystal diamond. *Nano Letters* **12**, 6084–6089 (2012). URL `http://dx.doi.org/10.1021/nl302541e`. PMID: 23163557, `http://dx.doi.org/10.1021/nl302541e`.

[51] Mohammad, M. A., Muhammad, M., Dew, S. K. & Stepanova, M. *Fundamentals of Electron Beam Exposure and Development*, 11–41 (Springer Vienna, Vienna, 2012). URL `http://dx.doi.org/10.1007/978-3-7091-0424-8_2`.

[52] Rommel, M. *et al.* Sub-10nm resolution after lift-off using hsq/pmma double layer resist. *Microelectron. Eng.* **110**, 123–125 (2013). URL `http://dx.doi.org/10.1016/j.mee.2013.02.101`.

[53] Wang, J. *et al.* High-sensitivity temperature sensing using an implanted single nitrogen-vacancy center array in diamond. *Phys. Rev. B* **91**, 155404 (2015). URL `http://link.aps.org/doi/10.1103/PhysRevB.91.155404`.

[54] Lis, S., Dylewicz, R., Mysliwiec, J. & Miniewicz, A. Application of flowable oxides in photonics. *Materials Science Poland* **Vol. 26, No. 1**, 189–194 (2008).

[55] Sugawara, M. *Plasma Etching: Fundamentals and Applications (Series on Semiconductor Science and Technology)* (Oxford University Press, 1998).

[56] RIE-ICP etching, Oxford Instruments, link = `https://www.oxford-instruments.com/products/etching-deposition-and-growth/plasma-etch-deposition/icp-etch`, last checked = Accessed: 17.12.2016.

[57] Wu, B., Kumar, A. & Pamarthy, S. High aspect ratio silicon etch: A review. *Journal of Applied Physics* **108**, 051101 (2010). URL `http://aip.scitation.org/doi/abs/10.1063/1.3474652`. `http://aip.scitation.org/doi/pdf/10.1063/1.3474652`.

[58] Lee, C., Gu, E., Dawson, M., Friel, I. & Scarsbrook, G. Etching and micro-optics fabrication in diamond using chlorine-based inductively-coupled plasma. *Diamond and Related Materials* **17**, 1292 – 1296 (2008). URL `http://www.sciencedirect.com/science/article/pii/S0925963508000174`. Proceedings of Diamond 2007, the 18th European Conference on Diamond, Diamond-Like Materials, Carbon Nanotubes, Nitrides and Silicon CarbideDiamond 2006Proceedings of Diamond 2007, the 18th European Conference on Diamond, Diamond-Like Materials, Carbon Nanotubes, Nitrides and Silicon Carbide.

[59] Mehedi, H.-a., Mille, V., Achard, J., Brinza, O. & Gicquel, A. Effect of the process parameters of inductively coupled plasma reactive ion etching on the fabrication of diamond nanotips. *physica status solidi (a)* **211**, 2343–2346 (2014). URL `http://dx.doi.org/10.1002/pssa.201431258`.

[60] Cleland, A. N. *Foundations of Nanomechanics* (Springer, 2001).

[61] Boyd, G. D., Coldren, L. A. & Storz, F. G. Directional reactive ion etching at oblique angles. *Applied Physics Letters* **36**, 583–585 (1980). URL `http://aip.scitation.org/doi/abs/10.1063/1.91554`. `http://aip.scitation.org/doi/pdf/10.1063/1.91554`.

[62] Burek, M. *et al.* High quality-factor optical nanocavities in bulk single-crystal diamond. *Nature Communications* **5** (2014).

[63] Sipahigil, A. *et al.* An integrated diamond nanophotonics platform for quantum optical networks. *Science* (2016). URL `http://science.sciencemag.org/content/early/2016/10/12/science.aah6875`. `http://science.sciencemag.org/content/early/2016/10/12/science.aah6875.full.pdf`.

[64] Momenzadeh, S. A. *et al.* Nanoengineered diamond waveguide as a robust bright platform for nanomagnetometry using shallow nitrogen vacancy centers. *Nano Letters* **15**, 165–169 (2015). URL `http://dx.doi.org/10.1021/nl503326t`. PMID: 25438091.

[65] Tisler, J. *et al.* Highly efficient fret from a single nitrogen-vacancy center in nanodiamonds to a single organic molecule. *ACS Nano* **5**, 7893–7898 (2011). URL `http://dx.doi.org/10.1021/nn2021259`. PMID: 21899301, `http://dx.doi.org/10.1021/nn2021259`.

[66] Rondin, L. *et al.* Nanoscale magnetic field mapping with a single spin scanning probe magnetometer. *Applied Physics Letters* **100** (2012). URL `http://scitation.aip.org/content/aip/journal/apl/100/15/10.1063/1.3703128`.

[67] Tisler, J. *et al.* Fluorescence and spin properties of defects in single digit nanodiamonds. *ACS Nano* **3**, 1959–1965 (2009). URL `http://dx.doi.org/10.1021/nn9003617`. PMID: 21452865, `http://dx.doi.org/10.1021/nn9003617`.

[68] Staudacher, T. *et al.* Nuclear magnetic resonance spectroscopy on a (5-nanometer)^3 sample volume. *Science* **339**, 561–563 (2013). URL `http://science.sciencemag.org/content/339/6119/561`. `http://science.sciencemag.org/content/339/6119/561.full.pdf`.

[69] Inam, F. A. *et al.* Modification of spontaneous emission from nanodiamond colour centres on a structured surface. *New Journal of Physics* **13**, 073012 (2011). URL `http://stacks.iop.org/1367-2630/13/i=7/a=073012`.

[70] VISSCHER, K., BRAKENHOFF, G. J. & VISSER, T. D. Fluorescence saturation in confocal microscopy. *Journal of Microscopy* **175**, 162–165 (1994). URL `http://dx.doi.org/10.1111/j.1365-2818.1994.tb03479.x`.

[71] Kurtsiefer, C., Mayer, S., Zarda, P. & Weinfurter, H. Stable solid-state source of single photons. *Phys. Rev. Lett.* **85**, 290–293 (2000). URL `http://link.aps.org/doi/10.1103/PhysRevLett.85.290`.

[72] Berthel, M. *et al.* Photophysics of single nitrogen-vacancy centers in diamond nanocrystals. *Phys. Rev. B* **91**, 035308 (2015). URL `http://link.aps.org/doi/10.1103/PhysRevB.91.035308`.

[73] Saleh, B. E. A. & Teich, M. C. *Fundamentals of Photonics, 2nd edition* (John Wiley and Sons, Inc., 2007).

[74] Träger, F. *Springer Handbook of Lasers and Optics* (Springer, 2007).

[75] Novotny, L. & Hecht, B. *Principles of Nano-Optics* (Cambridge, 2012).

[76] Henderson, M. R., V., S. A., Greentree, A. D. & Monro, T. M. Dipole emitters in fiber: interface effects, collection efficiency and optimization. *Opt. Express* **19**, 16182–16194 (2011). URL `http://www.opticsexpress.org/abstract.cfm?URI=oe-19-17-16182`.

[77] Appel, P. *et al.* Fabrication of all diamond scanning probes for nanoscale magnetometry. *Review of Scientific Instruments* **87** (2016). URL `http://scitation.aip.org/content/aip/journal/rsi/87/6/10.1063/1.4952953`.

[78] Ohno, K. *et al.* Engineering shallow spins in diamond with nitrogen delta-doping. *Applied Physics Letters* **101** (2012). URL `http://scitation.aip.org/content/aip/journal/apl/101/8/10.1063/1.4748280`.

[79] Sun, R. *et al.* Impedance matching vertical optical waveguide couplers for dense high index contrast circuits. *Opt. Express* **16**, 11682–11690 (2008). URL `http://www.opticsexpress.org/abstract.cfm?URI=oe-16-16-11682`.

[80] Ziegler, J. F., Ziegler, M. & Biersack, J. Srim - the stopping and range of ions in matter (2010). *Nuclear Instruments and Methods in Physics Research Section B: Beam Interactions with Materials and Atoms* **268**, 1818 – 1823 (2010). URL `http://www.sciencedirect.com/science/article/pii/S0168583X10001862`. 19th International Conference on Ion Beam Analysis.

[81] Yamada, T. *et al.* Cycle of two-step etching process using icp for diamond mems applications. *Diamond and Related Materials* **16**, 996 – 999 (2007). URL `http://www.sciencedirect.com/science/article/pii/S0925963506004171`. Proceedings of Diamond 2006, the 17th European Conference on Diamond, Diamond-Like Materials, Carbon Nanotubes, Nitrides and Silicon CarbideDiamond 2006.

[82] Ruijgrok, P. V., Wüest, R., Rebane, A. A., Renn, A. & Sandoghdar, V. Spontaneous emission of a nanoscopic emitter in a strongly scattering disordered medium. *Opt. Express* **18**, 6360–6365 (2010). URL `http://www.opticsexpress.org/abstract.cfm?URI=oe-18-6-6360`.

[83] de Lange, G., Wang, Z. H., Ristè, D., Dobrovitski, V. V. & Hanson, R. Universal dynamical decoupling of a single solid-state spin from a spin bath. *Science* **330**, 60–63 (2010). URL `http://science.sciencemag.org/content/330/6000/60`. `http://science.sciencemag.org/content/330/6000/60.full.pdf`.

[84] Romach, Y. *et al.* Spectroscopy of surface-induced noise using shallow spins in diamond. *Phys. Rev. Lett.* **114**, 017601 (2015). URL `http://link.aps.org/doi/10.1103/PhysRevLett.114.017601`.

[85] Naydenov, B. *et al.* Dynamical decoupling of a single-electron spin at room temperature. *Phys. Rev. B* **83**, 081201 (2011). URL `http://link.aps.org/doi/10.1103/PhysRevB.83.081201`.

[86] Rosskopf, T. *et al.* Investigation of surface magnetic noise by shallow spins in diamond. *Phys. Rev. Lett.* **112**, 147602 (2014). URL `http://link.aps.org/doi/10.1103/PhysRevLett.112.147602`.

[87] Schaefer-Nolte, E., Reinhard, F., Ternes, M., Wrachtrup, J. & Kern, K. A diamond-based scanning probe spin sensor operating at low temperature in ultra-high vacuum. *Review of Scientific Instruments* **85** (2014). URL `http://scitation.aip.org/content/aip/journal/rsi/85/1/10.1063/1.4858835`.

[88] Schäfer-Nolte, E. *et al.* Tracking temperature-dependent relaxation times of ferritin nanomagnets with a wideband quantum spectrometer. *Phys. Rev. Lett.* **113**, 217204 (2014). URL `http://link.aps.org/doi/10.1103/PhysRevLett.113.217204`.

[89] Steinert, S. *et al.* Magnetic spin imaging under ambient conditions with sub-cellular resolution. *Nature Communications* **4** (2013).

[90] Bar-Gill, N. *et al.* Solid-state electronic spin coherence time approaching one second. *Nature Communications* **4**, 1743 (2013).

[91] Jarmola, A., Acosta, V. M., Jensen, K., Chemerisov, S. & Budker, D. Temperature- and magnetic-field-dependent longitudinal spin relaxation in nitrogen-vacancy ensembles in diamond. *Phys. Rev. Lett.* **108**, 197601 (2012). URL `http://link.aps.org/doi/10.1103/PhysRevLett.108.197601`.

[92] Redman, D. A., Brown, S., Sands, R. H. & Rand, S. C. Spin dynamics and electronic states of n- v centers in diamond by epr and four-wave-mixing spectroscopy. *Phys. Rev. Lett.* **67**, 3420–3423 (1991). URL `http://link.aps.org/doi/10.1103/PhysRevLett.67.3420`.

[93] Zhang, J., Wang, C.-Z., Zhu, Z. Z. & Dobrovitski, V. V. Vibrational modes and lattice distortion of a nitrogen-vacancy center in diamond from first-principles calculations.

Phys. Rev. B **84**, 035211 (2011). URL `http://link.aps.org/doi/10.1103/PhysRevB.84.035211`.

[94] Häberle, T. *et al.* Nuclear quantum-assisted magnetometer. *Review of Scientific Instruments* **88**, 013702 (2017). URL `http://dx.doi.org/10.1063/1.4973449`. `http://dx.doi.org/10.1063/1.4973449`.

[95] Pelliccione, M. *et al.* Scanned probe imaging of nanoscale magnetism at cryogenic temperatures with a single-spin quantum sensor. *Nat Nano* **11**, 700 (2016). URL `http://dx.doi.org/10.1038/nnano.2016.68`.

[96] Nomura, S. *et al.* Nanopillar sheets as a new type of cell culture dish: detailed study of hela cells cultured on nanopillar sheets. *Journal of Artificial Organs* **9**, 90–96 (2006). URL `http://dx.doi.org/10.1007/s10047-006-0329-0`.

[97] Momenzadeh, S. A. *et al.* Thin circular diamond membrane with embedded nitrogen-vacancy centers for hybrid spin-mechanical quantum systems. *Phys. Rev. Applied* **6**, 024026 (2016). URL `http://link.aps.org/doi/10.1103/PhysRevApplied.6.024026`.

[98] Kurizki, G. *et al.* Quantum technologies with hybrid systems. *Proceedings of the National Academy of Sciences* **112**, 3866–3873 (2015). URL `http://www.pnas.org/content/112/13/3866.abstract`. `http://www.pnas.org/content/112/13/3866.full.pdf`.

[99] Aspelmeyer, M., Kippenberg, T. J. & Marquardt, F. Cavity optomechanics. *Rev. Mod. Phys.* **86**, 1391–1452 (2014). URL `http://link.aps.org/doi/10.1103/RevModPhys.86.1391`.

[100] Jöckel, A. *et al.* Sympathetic cooling of a membrane oscillator in a hybrid mechanical-atomic system. *Nat nano* **10**, 55–59 (2014). URL `http://dx.doi.org/10.1038/nnano.2014.278`.

[101] Etaki, S. *et al.* Motion detection of a micromechanical resonator embedded in a d.c. squid. *Nat Phys* **4**, 785–788 (2008). URL `http://dx.doi.org/10.1038/nphys1057`.

[102] YeoI. *et al.* Strain-mediated coupling in a quantum dot-mechanical oscillator hybrid system. *Nat Nano* **9**, 106–110 (2014). URL `http://dx.doi.org/10.1038/nnano.2013.274`. Letter.

[103] Irgens, F. *Continuum Mechanics* (Springer, 2008).

[104] Tao, Y., Boss, J. M., Moores, B. A. & Degen, C. L. Single-crystal diamond nanomechanical resonators with quality factors exceeding one million. *Nature Communications* **5**, 3638 (2014).

[105] Tsaturyan, Y., Barg, A., Polzik, E. S. & Schliesser, A. Ultra-coherent nanomechanical resonators via soft clamping and dissipation dilution. *Arxiv* (2016). URL `arXiv:1608.00937v1`.

[106] W. Greiner, H. S., L. Neise. *Thermodynamics and Statistical Mechanics* (Springer, 1995).

[107] Schwabl, F. *Quantum Mechanics* (Springer, 2007).

[108] Chan, J. *et al.* Laser cooling of a nanomechanical oscillator into its quantum ground state. *Nature* **478**, 89–92 (2011). URL `http://dx.doi.org/10.1038/nature10461`.

[109] Hauer, B., Doolin, C., Beach, K. & Davis, J. A general procedure for thermomechanical calibration of nano/micro-mechanical resonators. *Annals of Physics* **339**, 181 – 207 (2013). URL `http://www.sciencedirect.com/science/article/pii/S0003491613001723`.

[110] Anetsberger, G. *et al.* Near-field cavity optomechanics with nanomechanical oscillators. *Nat Phys* **5**, 909–914 (2009). URL `http://dx.doi.org/10.1038/nphys1425`.

[111] Anetsberger, G. *et al.* Measuring nanomechanical motion with an imprecision below the standard quantum limit. *Phys. Rev. A* **82**, 061804 (2010). URL `http://link.aps.org/doi/10.1103/PhysRevA.82.061804`.

[112] Klein, C. A. & Cardinale, G. F. Young's modulus and poisson's ratio of cvd diamond. *Diamond and Related Materials* **2**, 918 – 923 (1993). URL `http://www.sciencedirect.com/science/article/pii/0925963593902506`.

[113] Ovartchaiyapong, P., Pascal, L. M. A., Myers, B. A., Lauria, P. & Bleszynski Jayich, A. C. High quality factor single-crystal diamond mechanical resonators. *Applied Physics Letters* **101** (2012). URL `http://scitation.aip.org/content/aip/journal/apl/101/16/10.1063/1.4760274`.

[114] Meesala, S. *et al.* Enhanced strain coupling of nitrogen-vacancy spins to nanoscale diamond cantilevers. *Phys. Rev. Applied* **5**, 034010 (2016). URL `http://link.aps.org/doi/10.1103/PhysRevApplied.5.034010`.

[115] Kara, V. *et al.* Nanofluidics of single-crystal diamond nanomechanical resonators. *Nano Letters* **15**, 8070–8076 (2015). URL `http://dx.doi.org/10.1021/acs.nanolett.5b03503`. PMID: 26509332, `http://dx.doi.org/10.1021/acs.nanolett.5b03503`.

[116] Lee, K. W. *et al.* Strain coupling of a mechanical resonator to a single quantum emitter in diamond. *Phys. Rev. Applied* **6**, 034005 (2016). URL `http://link.aps.org/doi/10.1103/PhysRevApplied.6.034005`.

[117] Bennett, S. D. *et al.* Measuring mechanical motion with a single spin. *New Journal of Physics* **14**, 125004 (2012). URL `http://stacks.iop.org/1367-2630/14/i=12/a=125004`.

[118] Arcizet, O. *et al.* A single nitrogen-vacancy defect coupled to a nanomechanical oscillator. *Nat Phys* **7**, 879–883 (2011). URL `http://dx.doi.org/10.1038/nphys2070`.

[119] Kolkowitz, S. *et al.* Coherent sensing of a mechanical resonator with a single-spin qubit. *Science* **335**, 1603–1606 (2012). URL `http://science.sciencemag.org/content/335/6076/1603`. `http://science.sciencemag.org/content/335/6076/1603.full.pdf`.

[120] Teissier, J., Barfuss, A., Appel, P., Neu, E. & Maletinsky, P. Strain coupling of a nitrogen-vacancy center spin to a diamond mechanical oscillator. *Phys. Rev. Lett.* **113**, 020503 (2014). URL `http://link.aps.org/doi/10.1103/PhysRevLett.113.020503`.

[121] Ovartchaiyapong, P., Lee, K. W., Myers, B. A. & Jayich, A. C. B. Dynamic strain-mediated coupling of a single diamond spin to a mechanical resonator. *Nature Communications* **5**, 4429 EP – (2014). URL `http://dx.doi.org/10.1038/ncomms5429`. Article.

[122] Doherty, M. W. *et al.* Measuring the defect structure orientation of a single NV^- centre in diamond. *New Journal of Physics* **16**, 063067 (2014). URL `http://stacks.iop.org/1367-2630/16/i=6/a=063067`.

[123] Schuetz, M. J. A. *et al.* Universal quantum transducers based on surface acoustic waves. *Phys. Rev. X* **5**, 031031 (2015). URL `http://link.aps.org/doi/10.1103/PhysRevX.5.031031`.

[124] Rodriguez-Madrid, J. G. *et al.* Super-high-frequency saw resonators on aln/diamond. *IEEE Electron Device Letters* **33**, 495–497 (2012).

[125] Burek, M. J., Ramos, D., Patel, P., Frank, I. W. & Lonćar, M. Nanomechanical resonant structures in single-crystal diamond. *Applied Physics Letters* **103**, 131904 (2013). URL `http://scitation.aip.org/content/aip/journal/apl/103/13/10.1063/1.4821917`.

[126] Barfuss, A., Teissier, J., Neu, E., Nunnenkamp, A. & Maletinsky, P. Strong mechanical driving of a single electron spin. *Nature Physics* **11**, 820 (2015).

[127] Schomburg, W. *Introduction to Microsystem Design* (Springer, 2011).

[128] Thompson, J. D. *et al.* Strong dispersive coupling of a high-finesse cavity to a micromechanical membrane. *Nature* **452**, 72 (2008).

[129] Jayich, A. M. *et al.* Cryogenic optomechanics with a Si_3N_4 membrane and classical laser noise. *New Journal of Physics* **14**, 115018 (2012). URL `http://stacks.iop.org/1367-2630/14/i=11/a=115018`.

[130] Glenn, D. R. *et al.* Single-cell magnetic imaging using a quantum diamond microscope. *Nature Methods* **12**, 736 (2015).

[131] Jacobs, C. R., Huang, H. & Kwon, R. Y. *Introduction to Cell Mechanics and Mechanobiology* (Garland Science, 2012).

[132] Schwarz, U. S. & Soiné, J. R. Traction force microscopy on soft elastic substrates: A guide to recent computational advances. *Biochimica et Biophysica Acta (BBA) - Molecular Cell Research* **1853**, 3095 – 3104 (2015). URL `http://www.sciencedirect.com/science/article/pii/S0167488915001822`. Mechanobiology.

[133] MacQuarrie, E. R., Gosavi, T. A., Jungwirth, N. R., Bhave, S. A. & Fuchs, G. D. Mechanical spin control of nitrogen-vacancy centers in diamond. *Phys. Rev. Lett.* **111**, 227602 (2013). URL `http://link.aps.org/doi/10.1103/PhysRevLett.111.227602`.

[134] MacQuarrie, E. R. *et al.* Coherent control of a nitrogen-vacancy center spin ensemble with a diamond mechanical resonator. *Optica* **2**, 233–238 (2015). URL `http://www.osapublishing.org/optica/abstract.cfm?URI=optica-2-3-233`.

[135] Barson, M. S. *et al.* Nanomechanical sensing using spins in diamond. *Arxiv* (2016).

[136] Yu, H.-S. *Plasticity and Geotechnics* (Springer, 2006).

[137] Appel, P. *et al.* Fabrication of all diamond scanning probes for nanoscale magnetometry. *Review of Scientific Instruments* **87** (2016). URL `http://scitation.aip.org/content/aip/journal/rsi/87/6/10.1063/1.4952953`.

[138] Lee, R. E. Microfabrication by ion-beam etching. *Journal of Vacuum Science and Technology* **16**, 164–170 (1979). URL `http://scitation.aip.org/content/avs/journal/jvst/16/2/10.1116/1.569897`.

[139] Hess, P. The mechanical properties of various chemical vapor deposition diamond structures compared to the ideal single crystal. *Journal of Applied Physics* **111** (2012). URL `http://scitation.aip.org/content/aip/journal/jap/111/5/10.1063/1.3683544`.

[140] Zang, Y., Zhang, F., Di, C.-a. & Zhu, D. Advances of flexible pressure sensors toward artificial intelligence and health care applications. *Mater. Horiz.* **2**, 140–156 (2015). URL `http://dx.doi.org/10.1039/C4MH00147H`.

[141] Wang, Q., Hong, W. & Dong, L. Graphene "microdrums" on a freestanding perforated thin membrane for high sensitivity mems pressure sensors. *Nanoscale* **8**, 7663–7671 (2016). URL `http://dx.doi.org/10.1039/C5NR09274D`.

[142] Choi, W. *et al.* Enhanced sensitivity of piezoelectric pressure sensor with microstructured polydimethylsiloxane layer. *Applied Physics Letters* **104** (2014). URL `http://scitation.aip.org/content/aip/journal/apl/104/12/10.1063/1.4869816`.

[143] Zhang, Y., Howver, R., Gogoi, B. & Yazdi, N. A high-sensitive ultra-thin mems capacitive pressure sensor. In *2011 16th International Solid-State Sensors, Actuators and Microsystems Conference*, 112–115 (2011).

[144] Persano, L. *et al.* High performance piezoelectric devices based on aligned arrays of nanofibers of poly(vinylidenefluoride-co-trifluoroethylene). *Nat Commun* **4**, 1633 (2013). URL `http://www.nature.com/ncomms/journal/v4/n3/suppinfo/ncomms2639_S1.html`.

[145] Taylor, J. M. *et al.* High-sensitivity diamond magnetometer with nanoscale resolution. *Nat Phys* **4**, 810–816 (2008). URL `http://dx.doi.org/10.1038/nphys1075`.

[146] Ivády, V., Simon, T., Maze, J. R., Abrikosov, I. A. & Gali, A. Pressure and temperature dependence of the zero-field splitting in the ground state of nv centers in diamond: A first-principles study. *Phys. Rev. B* **90**, 235205 (2014). URL `http://link.aps.org/doi/10.1103/PhysRevB.90.235205`.

[147] Bennett, S. D. *et al.* Phonon-induced spin-spin interactions in diamond nanostructures: Application to spin squeezing. *Phys. Rev. Lett.* **110**, 156402 (2013). URL `http://link.aps.org/doi/10.1103/PhysRevLett.110.156402`.

[148] de Lépinay, L. M. *et al.* Nano-optomechanical measurement in the photon counting regime. *Arxiv* (2015).

[149] Longenecker, J. G. *et al.* High-gradient nanomagnets on cantilevers for sensitive detection of nuclear magnetic resonance. *ACS Nano* **6**, 9637–9645 (2012). URL `http://dx.doi.org/10.1021/nn3030628`. PMID: 23033869, `http://dx.doi.org/10.1021/nn3030628`.

[150] Jakobi, I. *et al.* Measuring broadband magnetic fields on the nanoscale using a hybrid quantum register. *Nat Nano* **advance online publication** (2016). URL `http://dx.doi.org/10.1038/nnano.2016.163`. Article.

[151] Rabl, P. *et al.* A quantum spin transducer based on nanoelectromechanical resonator arrays. *Nat Phys* **6**, 602–608 (2010). URL `http://dx.doi.org/10.1038/nphys1679`.

[152] S., H. *et al.* Single-protein nanomechanical mass spectrometry in real time. *Nat Nano* **7**, 602–608 (2012). URL `http://dx.doi.org/10.1038/nnano.2012.119`.

[153] Hanay, M. S. *et al.* Inertial imaging with nanomechanical systems. *Nat Nano* **10**, 339–344 (2015). URL `http://dx.doi.org/10.1038/nnano.2015.32`. Article.

[154] Guillon, S. *et al.* Effect of non-ideal clamping shape on the resonance frequencies of silicon nanocantilevers. *Nanotechnology* **22**, id 245501 (2011). URL `https://hal.archives-ouvertes.fr/hal-01343625`.

[155] Deng, G.-W. *et al.* Coupling two distant double quantum dots with a microwave resonator. *Nano Letters* **15**, 6620–6625 (2015). URL `http://dx.doi.org/10.`

`1021/acs.nanolett.5b02400`. PMID: 26327140, `http://dx.doi.org/10.1021/acs.nanolett.5b02400`.

[156] Delbecq, M. R. *et al.* Photon-mediated interaction between distant quantum dot circuits. *Nature Communications* **4**, 1400 EP – (2013). URL `http://dx.doi.org/10.1038/ncomms2407`. Article.

[157] Wei, B.-B., Burk, C., Wrachtrup, J. & Liu, R.-B. Magnetic ordering of nitrogen-vacancy centers in diamond via resonator-mediated coupling. *EPJ Quantum Technology* **2**, 18 (2015). URL `http://dx.doi.org/10.1140/epjqt/s40507-015-0032-2`.

[158] Oh, S. & Kim, J. Entanglement between qubits induced by a common environment with a gap. *Phys. Rev. A* **73**, 062306 (2006). URL `http://link.aps.org/doi/10.1103/PhysRevA.73.062306`.

[159] Rao, D. D. B., Momenzadeh, S. A. & Wrachtrup, J. Heralded control of mechanical motion by single spins. *Phys. Rev. Lett.* **117**, 077203 (2016). URL `http://link.aps.org/doi/10.1103/PhysRevLett.117.077203`.

[160] Nakajima, M., Wang, D. F., Ikehara, T. & Maeda, R. Synchronized oscillation in micro mechanically coupled opposite c-shaped cantilever-based oscillator system. In *2011 16th International Solid-State Sensors, Actuators and Microsystems Conference*, 1492–1495 (2011).

[161] Endo, D., Yabuno, H., Higashino, K., Yamamoto, Y. & Matsumoto, S. Self-excited coupled-microcantilevers for mass sensing. *Applied Physics Letters* **106** (2015). URL `http://scitation.aip.org/content/aip/journal/apl/106/22/10.1063/1.4921082`.

[162] Spletzer, M., Raman, A., Wu, A. Q., Xu, X. & Reifenberger, R. Ultrasensitive mass sensing using mode localization in coupled microcantilevers. *Applied Physics Letters* **88** (2006). URL `http://scitation.aip.org/content/aip/journal/apl/88/25/10.1063/1.2216889`.

[163] Sato, M. *et al.* Observation of locked intrinsic localized vibrational modes in a micromechanical oscillator array. *Phys. Rev. Lett.* **90**, 044102 (2003). URL `http://link.aps.org/doi/10.1103/PhysRevLett.90.044102`.

[164] Janitz, E. *et al.* Fabry-perot microcavity for diamond-based photonics. *Phys. Rev. A* **92**, 043844 (2015). URL `http://link.aps.org/doi/10.1103/PhysRevA.92.043844`.

[165] Rabl, P. Cooling of mechanical motion with a two-level system: The high-temperature regime. *Phys. Rev. B* **82**, 165320 (2010). URL `http://link.aps.org/doi/10.1103/PhysRevB.82.165320`.

[166] Rabl, P. *et al.* Strong magnetic coupling between an electronic spin qubit and a mechanical resonator. *Phys. Rev. B* **79**, 041302 (2009). URL `http://link.aps.org/doi/10.1103/PhysRevB.79.041302`.

List of Figures

1.1. a) Absorption coefficient of diamond is shown vs. the wavelength. As can be seen, diamond is transparent from the UV to IR region of the spectral range. Figure is taken from [9]. b) Refractive index of bulk diamond (n) is shown vs. the wavelength. As demonstrated, the refractive index of diamond decreases for $\approx 20\%$ as the wavelength is increased from 200 nm to 1000 nm. 22

1.2. Lattice structure of an NVC defect in diamond is depicted. As shown, NVC is formed of a substituting nitrogen impurity attached to the neighbor lattice vacancy. 25

1.3. Energy structure diagram of an NVC in diamond in room temperature is depicted. a) The energy levels of NVC are located within the band gap of diamond. Ground state ($|\mathrm{g}\rangle$), excited state ($|\mathrm{e}\rangle$), and metastable singlet state ($|\mathrm{m}\rangle$) form the energy scheme of an NVC. The allowed transitions between these states are depicted. The wavy arrows show the radiative transitions (which are also spin-preserving) where the straight solid arrows present the non-radiative ones. Figure is adapted from [20]. b) The $|\mathrm{g}\rangle$ of an NVC is focused, noting the zero-field splitting term (D) and the magnetic Zeeman interaction. c) An emission spectrum of an NVC under pumping wavelength of 532 nm is demonstrated, showing the ZPL and broad phonon sideband. 26

1.4. a) ODMR measurement revealing the $m_s = \pm 1$ spin sublevels is shown. As can be seen, with respect to the Zeeman interaction, the ODMR technique can also give information about the magnetic field applied to the NVC. b) By applying ODMR technique, the present nearby ^{15}N nuclear spin coupled to the electron spin of the NVC can be detected. c) The ground-state spin sublevels of the NVC form a quantum mechanical two-level system for which, by applying the resonant MW pulses, the Rabi period can be measured to be $\approx$ 100 ns. d) The frequently-used Hahn echo scheme to measure the T_2 coherence times of NVCs is shown. Initially the NVC is pumped (P) into its $m_s = 0$ state. Then $\pi/2$-$\tau/2$-π-$\tau/2$-π sequence consisting of resonant MW pulses and delay times is applied to the NVC. Finally the readout (R) of the spin state of the NVC is performed. This process is repeated for multiple times to achieve sufficient signal-to-noise ratio. The Hahn echo decay signal for NVCs with different depths are shown in Figure 1.4-(e) to -(f). The decay behavior can be either Gaussian which is imposed by the slowly fluctuating ^{13}C nuclear spin environment, or be exponential which is set by rapidly fluctuating surface impurities. Figures (e) - (f) are taken from [24]. 28

1.5. a) Total internal reflection (TIR) process with the critical angle (θ_c) is shown as an obstacle imposing poor collection efficiency of NVCs. b) Macro- and microscale diamond solid immersion lenses (SILs) are developed to increase the photon collection efficiency of bulk NVCs. Figures are taken from [27, 28]. The scale bar in the lower figure presents 10 μm. c) Nanopillars are waveguides which are fabricated directly onto the diamond substrate to increase the number of collected photons from shallow and bulk NVCs. Figure is taken from [29]. Besides the monolithic solutions to the enhancement of photon collection efficiency of NVCs, non-monolithic solutions are also developed, as shown in d), e) and f). In d) silver layer is employed to apply Purcell enhancement to the photon count rate of NVCs integrated in the nanopillars. Figure is taken from [30]. e) Another approach can be utilization of a GaP lens which guides the photons emitted by the NVC to the objective lens. Figure is taken from [31]. f) By means of bullseye diamond structure which is mounted on top of a glass substrate, more than one order of magnitude enhancement is obtained in the photon collection efficiency of NVCs. Figure is taken from [32]. 30

2.1. Fabrication scheme of the diamond thin films from the starting bulk diamond substrate is depicted. (a) The bulk substrate is first bisected by means of high power laser beam (e.g. along the white lines). b) Then, to remove the cutting-induced rough surface and also approach the desired thickness, they are thinned down and polished by means of mechanical tools (e.g. along the red lines). This step is a time-consuming process which is of crucial importance for the suitability of the output films in their applications. (c) Afterward, to provide more diamond films, they are transversely cut into few more pieces, usually with the dimensions of ~ 2 mm $\times$ 2 mm $\times$ 30 μm (e.g. along the white lines). (d) As an illustrative presentation of the final thin diamond films, one of them, which is glued on top of a type-I diamond (marked with a blue circle), is shown. Scale bar shows 2 cm. 35

2.2. Fabrication and characterization of the NVC array arrangement is demonstrated. (a) As the first step, $\sim$ 1000 apertures with the diameter of $\approx$ 50 nm are formed in $\approx$ 400 nm-thick PMMA with the matrix distance of 4 μm on top of a diamond substrate. (b) Then, 30 nm of chromium (Cr) is deposited by means of high vacuum thermal deposition technique on top of the whole mask. Next, the lift-off process is performed, which leaves finally only the deposited Cr layer within the PMMA apertures. This way is utilized to verify the PMMA aperture size. (c) An SEM image of one of these Cr points reveals a diameter of $\approx$ 52 nm. Scale bar shows 50 nm. (d) After verifying the right aperture size, step (a) is repeated again. Then, nitrogen ions are implanted through the PMMA apertures into the diamond lattice to generate NVCs. (e) An exemplary confocal image of the developed NVC array system is depicted. Scale bar shows 10 μm. (f) Statistics on the formation of NVCs within 1941 developed PMMA apertures is shown. As can be seen, $\sim$ 20% of the apertures possess double NVCs. The statistics is assessed based on the fluorescence intensity acquired from each spot. 38

2.3. Scheme of an RIE-ICP chamber is depicted. Gas molecules are introduced from top into the chamber. The substrate is positioned on top of the electrode connected to the RIE source. By interacting with the reactive species, the substrate is etched, then the volatile etch product gas will be pumped out from the chamber. In the case of RIE-ICP chambers, a separate power generator is exploited to control the magnetic field applied to the plasma through the coils surrounding the chamber (shown by brown symbols). This system gives high density of low-energy plasma with high uniformity, which yields in high etching rates associated with highly-anisotropic etching performance. Figure is adapted from [56]. 42

2.4. Transverse (a, b, c) and angled (d ,e, f) etching of diamond substrate is demonstrated. a) Shows the FOX 25 etching mask on top of the diamond substrate. Scale bar shows 400 nm. b) Diamond substrate is etched by means of oxygen RIE-ICP procedure using the mask shown in (a). As can be seen, the diamond nanopillar geometry is realized, while $\sim$ 150 nm of the FOX 25 remains. Scale bar shows 400 nm. (c) Residual of the etching mask is removed by leaving the sample for few minutes in buffered HF solution. Scale bar shows 400 nm. (d) Shows the constructed Faraday cage to perform the angled etching process of diamond substrate. The cage is an aluminum prism with triangular cross-section of $\sim$ 2 cm. Scale bar shows 2 cm. To perform such a way of etching, first transverse etching of diamond is accomplished. Then, angled way of diamond etching is pursued by introducing the Faraday cage shown in (d) to the etching chamber. f) An example of angled etching process is shown. Single-side and double-side clamped nanobeams with lateral dimensions of $\sim$ 200 nm and length of $\sim$ 5 μm are fabricated. The white color of the structures is due to presence of the residual of Cr etching mask. Scale bar shows 10 μm. 45

3.1. Optical absorption and excitation are shown in an optical two-level system. The absorption, radiative, and non-radiative decay rates are noted with κ_a, κ_r, and κ_{nr}, respectively. 51

3.2. The scheme of an optical three-level system including the GS, ES, and the MS states is shown. The pumping and decay rates of k, Γ_1, Γ_2, and Γ_3, respectively, are depicted. 53

3.3. The scheme of a step-index fiber with the radii of r_a and r_b of the core and cladding, respectively, is shown. As mentioned, the refractive index of the cladding is smaller than that of the core ($n_{cl} < n_c$). 55

3.4. The variation of the normalized propagation constant and accordingly the effective refractive index of the fundamental mode of the fiber is shown vs. its V parameter. As depicted, the effective refractive index of the fiber for the fundamental mode is bound between the refractive index of the cladding and that of the core. 56

3.5. a) Schematic cross-sectional view of an NVC dipole inside a step-index fiber is shown. b) and c) The normalized power of an NVC dipole oriented radially at the center of the fiber core emitting at $\lambda = 700$ nm captured by the total modes (b) and only guided modes (c) of the fiber is plotted vs. the fiber core diameter. Insets in (b) and (c) give different refractive indexes associated with different core material. Fluctuation behavior in the normalized power due to the presence of new modes inside the fiber is observed. d) The normalized power of a radially-oriented NVC emitting at $\lambda = 700$ nm inside a fiber core with $n_c = 2.02$ and diameter of 220 nm is plotted vs. its radial position (a is the radius of the fiber core). At $r/a = 1$, the sharp change is due to the discontinuity of the radial field at the core-cladding interface. Figures (b), (c), and (d) are taken from [76]. 58

3.6. The general sketch of the purely-cylindrical (a) and conically-tapered (b) nanopillar geometries hosting a single shallow NVC is depicted. 59

3.7. FEM simulations towards optimization of the collected photon intensity of an NVC located on the axis of the purely-cylindrical nanopillar geometry, 5 nm below the diamond surface is shown. This plot shows the intensity of the collected electric field vs. the diameter of the purely-cylindrical nanopillar geometry (and equivalently, number of the guided modes). 61

3.8. Optimization of the collected photon intensity of an NVC located 5 nm below the diamond surface at the axis of the conically-tapered nanopillar geometry with the top diameter of 400 nm, via FEM simulation is shown. The intensity of the collected electric field intensity is studied vs. the bottom diameter of the nanopillar (d_b) while the height and top diameter are fixed (see the inset) at 1.2 μm and 400 nm, respectively. 62

3.9. The electric field intensity pattern emitted by an NVC 5 nm below the diamond surface radially at the center of a conically-tapered nanopillar with bottom and top diameters and height of 900 nm, 400 nm, and 1.2 μm, respectively, obtained from FEM simulations, is shown. (a) and (b) show the in-plane and out-of-plane emission intensity patterns, respectively. 63

3.10. Dependency of the collected electric field intensity of an NVC with the depth of 5 nm inside a conically-tapered nanopillar (height: 1.2 μm, bottom diameter: 900 nm, top diameter: 400 nm) on its distance from the nanopillar axis using the FEM simulation is presented. In this plot the effect of receding both in-plane (black curve) and out-of-plane (red curve) of the electric dipole with respect to the nanopillar axis (see the inset) is shown. 64

3.11. Realization scheme of the conically-tapered nanopillar geometry is shown. The thin diamond film substrate hosting shallow-implanted NVCs and the adhesion Cr layer (a) will be addressed in the next steps for the generation of the FOX 25 mask (b) by means of e-beam lithography technique. The RIE-ICP etching method is applied (c) to transfer the shape of the mask to the diamond substrate. After the etching step, the diamond sample is cleaned (d) in buffered HF, Cr etching, and triacid mixture solutions. 65

3.12. SEM image of the conically-tapered nanopillar geometry is shown. a) An array of tapered nanopillars (scale bar = 5 μm) is depicted. (b) SEM image of a conically-tapered diamond nanopillar with the approximate bottom and top diameter of 900 nm and 400 nm, respectively, is shown where its height is $\approx$ 1.2 μm (scale bar = 500 nm). 66

3.13. (a) Confocal image of an array of the hybrid nanopillar-NVC photonic structure is shown. The relatively low background signal in the etched area and also the tapered nanopillars lacking NVCs is clear. For the sake of clarity, example of nanopillars with no, single, and multiple NVCs are marked. Scale bar represents 10 μm. Sketch of the HBT setup (b) to perform the second-order fluorescence autocorrelation ($g^{(2)}$) measurements (c) is depicted. As can be seen in (c), the $g^{(2)}(\tau=0) \approx 0.18$ indicates a clean (see the main text) fluorescence signal proving a single-photon emission behavior. (d) Number of NVCs inside the nanopillar geometry can be estimated using the output of autocorrelation measurements. As demonstrated, almost 30% of the hybrid systems possess single NVC. 68

3.14. Decay rates of the excited state emission of NVCs located few nanometers below the diamond surface inside and outside of the nanopillar geometry vs. the implantation energy are shown. As can be seen in most of the cases, the decay shows two-component exponential decay (nonzero fast decay shown in black squares) while the slow-decay (shown in red circles) mostly has values longer than the well-known bulk value of 12 ns (shown with a dashed orange line). To compare the effect of the presence of the nanopillar geometry and NVCs' depth (equivalently their implantation energy), NVCs resulting from different implantation energies inside and outside of the nanopillar geometry (inside the gray-filled rectangle) are investigated. The plotted results in this figure do not conclude any systematic effect of the nanopillar waveguide on the excited-state lifetime of the embedded shallow NVCs. 69

3.15. (a) Saturation plot of an NVC few nanometers below the facet of the presented conically-tapered nanopillar geometry is shown. The total, net, and background signals are shown by gray-dotted, blue-dotted, and orange-dotted curves, where the black line shows the fit based on the model given in Eq. (3.5). (b) Saturation fluorescence rate and power of NVCs inside the conically-tapered nanopillar geometry with the height of 1.2 μm and top diameter of 400 nm, where the bottom diameter is varied. As can be seen, the larger the bottom diameter the higher (lower) will be the saturation count rate (power). This indeed proves that the presented structure is a broadband waveguide for both the excitation and emission of the embedded NVCs. The horizontal error bars of 20 nm show the tolerance in the bottom diameter due to the precision of the fabrication process and also the SEM imaging accuracy. 70

3.16. Simulated and measured detected saturation intensities of the NVCs embedded in the conically-tapered nanopillar geometry are compared. The red dots show the measured data (error bar of 20 nm in bottom radius) for four different bottom diameters of the nanopillar structure, where the blue curve shows the simulated collected electric field intensity. As can be seen, consistent match exists between these two curves, proving the validity of the FEM simulations with respect to the experimental achievements. 72

3.17. (a) Scheme of the NVC-tapered nanopillar hybrid system in spin-dephasing time measurements; magnetic field of 100-150 G is aligned to the NVC axis, where MW pulses are applied to the NVC via a copper wire spanned over the nonstructured side of the diamond substrate. (b) Plot of T_2 times of NVCs inside the hybrid system and also under the bare (nonstructured) diamond surface vs. different N^+ implantation energies is given. As can be seen, similar values from two different cases are obtained. This notes the preservation of the spin properties of shallow NVCs inside the nanopillars due to the designed geometry and applied fabrication process. 73

3.18. a) Scheme of the CPMG pulse sequence is depicted. b) The measured T_2 (CPMG-N) vs. N for an NVC generated from 2.5 keV of implantation energy is depicted (applied magnetic field of 117 G). By fitting this data to T_2 (CPMG) $= N^{\gamma} \cdot T_2$ (Hahn echo), γ exponent of ≈ 0.50 is derived. 74

3.19. (a) T_1 dephasing curves of a single shallow NVC at the extremity of the conically-tapered nanopillar at $T \approx 5$K in the presence (green color) and absence (black color) of 100 G aligned magnetic field are depicted. The blue and orange exponential fits give approximate T_1 values of 300 ms and 100 ms, respectively. (b) The inverse T_1 values of the investigated NVC in the absence of applied magnetic field is shown vs. temperature. As it is demonstrated, going from room temperature down to ≈ 5 K, the T_1 relaxation time increases from ~ 5 ms to ~ 100 ms. This dependency is fitted by the model given in Eq. (3.19). 75

3.20. Diamond scanning probe including a tapered nanopillar geometry is shown. (a) A tapered nanopillar directly fabricated onto a diamond cantilever (marked with the black oval) is attached to a quartz fiber which is then glued into an AFM tuning fork. (b) The marked area in image (a) is magnified here. As shown in the black circle, the nanopillar geometry is a key element of this diamond scanning probe. Scale bars in figures (a) and (b) depicts 100 μm and 5 μm, respectively. The demonstrated figures (a) and (b) are courtesy of Anurag Kanase and Amit Finkler. 77

4.1. Scheme of the spin-phonon interaction via magnetic coupling is demonstrated. (a) Shows the scheme of a mechanical resonator with resonance frequency of ω with an attached magnetized AFM tip (blue triangle) to generate a spatially-modulated magnetic field. In this case, an NVC is located inside the diamond bulk substrate. (b) Mechanical resonator oscillation with respect to the MW pulses of the Hahn echo sequence is depicted. In such a manner, the Hahn echo signal of the NVC probe can be used to describe the oscillation of the mechanical system. Figures are adapted from Ref [45]. 84

4.2. Scheme of the strain-mediated spin-phonon coupling is demonstrated. (a) Shows the scheme of a diamond mechanical resonator (microcantilever) with an embedded NVC. The deflection of the cantilever induces strain. With respect to the FEM simulations (b) the maximum strain (ε_{xx}) is found to occur at the vicinity of the clamping point of the cantilever. (c) The effect of axial and transverse strain on the m_s=$|\pm1\rangle$ spin levels is depicted. The axial strain causes a linear shift added to the zero-field splitting, while the transverse strain mixes these states. Figures (a) and (c) are adapted from [45]. 86

4.3. Schematic geometry of the spin-phonon coupling of NVC via the piezomagnetic material is shown. (a) Shows a piezomagnetic material deposited on top of a diamond substrate hosting an NVC close to its surface. (b) Depicts an NVC inside a diamond nanocrystal which is positioned to the nanoscale proximity of the piezomagnetic material with the aid of an AFM tip. 87

4.4. The scheme of thick (a), thin (b), and flexible (c) circular membranes is depicted. The flexible membranes do not show well-defined behavior and hence, are out of the current study. The comparison of the thickness (t) and central deflection (w) under an applied pressure, divides the circular membranes into two main categories of thick and thin ones. Figure is adapted from [127]. . . 89

4.5. Unit cell of the diamond with an NVC is shown to illustrate the different (x,y,z) and (X,Y,Z) notations used in the analytical study of the stress applied to the NVC spin. As depicted, (X,Y,Z) demonstrates the Cartesian coordinate system for the diamond unit cell, where (x,y,z) presents the NVC. Regarding the NVC, orientation along z is named as longitudinal, whereas x and y demonstrate transverse orientations. 91

4.6. General scheme of the exploited etching technique to transfer the circular membrane geometry to an implanted thin diamond film is depicted. The superiority of angled-wall hole in the diamond mask (b) in comparison to the vertical-wall hole (a) is shown. By using this etching mask with angled-wall hole through, no trace of trenching and cracking can be seen. 92

4.7. The hybrid NVC-diamond membrane system is demonstrated. The fabrication process results in a (a) ≈ 2 mm $\times$ 2 mm $\times$ 0.027 mm diamond film with a 1.1 mm diameter thin membrane at its center. It is glued on a glass with a hole at its center to avoid mechanical contact to the membrane. Scale bar shows 500 μm. (b) The etching profile of the fabricated sample is shown, where the etching depth of > 25 μm is revealed. By using the angled-wall hole in the diamond mask substrate, no trace of cracks and trenching can be seen in the final sample, where only a minor thickness deviation of $\sim 0.1\%$ through the whole diameter is left. 94

4.8. The mounting of the hybrid diamond membrane-NVC system is schematically illustrated. (a) It shows the hybrid device mounted under a nitrogen gas vessel in a home-built confocal setup. (b) The confocal image from an area near the center of the membrane is presented. It shows no negative effect caused by the applied fabrication process. Scale bar represents 3 μm. 95

4.9. Optical investigations of the membrane-NVC hybrid system are depicted. (a) Applied DC pressure to the system vs. deflection at its center is plotted. The cubic polynomial behavior of the curve is a clear characteristic of the mechanics of a thin circular membrane. Vertical error bars demonstrate 0.05 bar whereas the horizontal error bars are not shown. (b) Recording the fluorescence rate of a single NVC located at the center of the membrane in the absence and presence of a small applied pressure is shown. As explained in the main text, this pressure is calculated to be ≈ 40 Pa. 96

4.10. (a) The simulation of the longitudinal frequency shift (absolute value) distribution over the membrane area is plotted (for an applied pressure of 1 bar) for two different sets of NVC crystallographic orientations. There is an azimuthal asymmetry in both of the plots, which is imposed by breaking of the symmetry due to the nonsymmetric orientation of the NVCs. (b) The absolute value of the experimental and the model data of the longitudinal frequency shift detected by a single NVC located at the center of the membrane is depicted. The developed model considering the membrane mechanics and the spin-mechanical interactions predicts similar behavior as the ODMR measurements. 97

4.11. A histogram of the longitudinal frequency shift of approximately 15 NVCs per each crystallographic orientation (A-D) from $D = 2.870$ GHz is measured. Common to all four different orientations, most of the NVCs show longitudinal frequency shifts lower than 1 MHz. As mentioned in the main text, this yields in average frequency shift of 0.82 MHz which is translated in approximately 52 MPa of net radial residual stress. 98

4.12. (a) Measurement of the fundamental mode frequency of the membrane by means of embedded single NVC is shown. (b) In-resonance vibration amplitude of the membrane vs. the piezo driving voltage is estimated by means of single NVCs, revealing an overall nonlinear behavior. Nevertheless, this behavior can be approximated to a linear fit with slope of 0.38 μm/V for voltages <2 V. 101

4.13. (a) Hahn echo signal under $\approx$ 290 G in absence (green curve with blue fit [24]) and presence (black curve with red fit) of in-resonance mechanical driving is demonstrated. An oscillation behavior obeying Bessel function proves that the system is in driven regime, as presented theoretically before [117]. (b) Coupling parameter of the spin of a single NVC to a single phonon of membrane vibration vs. the piezo driving voltage is shown. As depicted, almost a constant value is obtained to be $g = 6.12 \pm 1.09 \times 10^{-4}$ rad/s. 102

4.14. (a) Driven decoherence rate is plotted vs. the driving voltage of the piezo chip. Nonlinear behavior of the membrane oscillator and possible heating effects can cause ascending decoherence rate. (b) Simulated spin-phonon coupling parameter (g in Hz) is shown vs. radius and thickness of the membrane. In this simulation, residual stress of the membrane and the magnetic field gradient are considered to be 100 MPa and 5×10^6 T/m, respectively. 103

4.15. Scheme of a single-side clamped microcantilever with rectangular cross-section is shown. (a) 2D scheme of the cantilever with the length and thickness of l and t, respectively, under a transverse (parallel to y axis) applied force F at its free end is demonstrated. This force induces a deflection (w) parallel to the cantilever thickness, which depends on the coordinate along its length (x). Figures (b) and (c) present the first two vibrational flexural modes of the cantilever. (b) Presents the 1^{st} flexural mode of the cantilever which is called as fundamental mode. (c) Shows the 2^{nd} vibrational flexural mode of the cantilever. In figures (b) to (c), the FEM-simulated spatial distribution of the strain component ε_{xx} through the cantilever geometry is shown. For instance, given the fundamental mode, strain is maximum close to the clamping point of the cantilever. 104

4.16. (a) Two NVCs are located each at the extremity of two separated cantilevers which are mechanically coupled to each other. Based on the mechanical coupling of these two cantilevers, they show common mechanical modes. Applying an identical magnetic field gradient to both of these NVCs, due to their location, they feel the same vibrational behavior and hence, spin-phonon coupling strength. Thereupon, although these two cantilevers are separated from each other and can be addressed, initialized, and readout separately, they can be coupled through the common modes featuring a mechanical quantum bus. (b) As mentioned in the main text, the spin-phonon interaction (g), i.e. the coupling strength between each NVC spin and the common mechanical mode phonons (g) play a crucial role, since the indirect coupling strength of two separated NVCs through the mechanical mode as the quantum bus is dependent on g^2. 106

4.17. Scheme of two coupled damped mechanical oscillators is depicted. (a) Shows two masses each connected to a spring associated with spring constant k, while these two are connected together by spring constant k'. (b) and (c) present FEM simulated strain (ε_{XX}) distribution in coupled modes for two cantilevers with length, width, and thickness, of 80, 5, and 2 μm, respectively, that are separated for 5 μm from each other. As depicted, the first coupled mode shows symmetric deflection behavior (b) whereas the second mode show asymmetric behavior (c). 108

4.18. (a) Scheme of the coupled cantilevers used in the FEM simulation is depicted, where the outer edge of the shown picture is mechanically constrained. In this simulation, the geometry is fixed, only the distance (r) between two cantilevers is swept symmetrically with respect to the whole geometry (blue dashed line). (b) The FEM simulation result on the effect of the distance between two cantilevers on the common modes frequency difference is presented. As can be seen, the splitting between these two resonance frequencies increase as the distance between the two cantilevers decrease. 109

4.19. Realization of mechanically-coupled diamond microcantilevers is schematically demonstrated. (a) A thin diamond film is produced as the starting point, then PMMA and FOX 25 resists are spin coated on it, followed by e-beam lithography process of FOX 25 resist. The designed layout to expose the FOX 25 resist is indeed not the desired structure geometry, but its inverted geometry. This makes the exposure time much shorter in comparison to the ordinary case. (b) The PMMA layer is etched through by means of O_2 etching plasma, then 150 nm of Ti is deposited via thermal evaporation technique. (c) After preparing the Ti mask, the diamond film is etched using O_2 RIE-ICP plasma recipe. At the end, SF_6-CF_4 RIE-ICP step is applied to remove the residual of the Ti mask. (d) shows an SEM image of one of the resulting mechanically-coupled microcantilevers. Scale bar denotes 20 μm. 110

4.20. (a) Optical image of mechanically-coupled cantilevers is shown. (b) These two dips show two different resonance frequencies of the fast and slow modes of mechanically-coupled cantilevers. To prove the validity of the statement about realization and observation of coupled cantilevers, one of these two cantilevers is broken (c). Then as shown in (d), only one resonance frequency is observable. Scale bars in (a) and (c) present 20 μm. 113

4.21. Modified geometry of the microcantilevers is shown (left side). In this way, center of these microcantilevers is etched through. In comparison to the ordinary geometry (right side), they can yield in larger ZPF and consequently larger spin-phonon coupling parameter. Scale bar shows 20 μm. 114

A.1. Sketch of the developed confocal setup is demonstrated. 118

A.2. The electronic and MW parts of the measurement setup are demonstrated. . . 119

A.3. Figures of the designed sample holder and the mechanical mounting of the sample and the magnet are depicted. The scale bar in Figure (a)-main shows 2 cm, 5 mm in its inset, and 5 cm in Figure (b). 120

List of Publications

1) Coherent control of single spins in silicon carbide at room temperature
Matthias Widmann, Sang-Yun Lee, Torsten Rendler, Nguyen Tien Son, Helmut Fedder, Seoyoung Paik, Li-Ping Yang, Nan Zhao, Sen Yang, Ian Booker, Andrej Denisenko, Mohammad Jamali, **S. Ali Momenzadeh** , Ilja Gerhardt, Takeshi Ohshima, Adam Gali, Erik Janzén & Jörg Wrachtrup
Nature Materials **14**, 164-168 (2015), DOI:10.1038/nmat4145

2) Nanoengineered diamond waveguide as a robust bright platform for nanomagnetometry using shallow nitrogen vacancy centers
S. Ali Momenzadeh , Rainer J. Stöhr, Felipe Fávaro de Oliveira, Andreas Brunner, Andrej Denisenko, Sen Yang, Friedemann Reinhard, and Jörg Wrachtrup
Nano Lett., **2015**, 15 (1), pp 165-169, DOI: 10.1021/nl503326t

3) Effect of low-damage inductively coupled plasma on shallow nitrogen-vacancy centers in diamond
Felipe Fávaro de Oliveira, **S. Ali Momenzadeh** , Ya Wang, Mitsuharu Konuma, Matthew Markham, Andrew M. Edmonds, Andrej Denisenko and Jörg Wrachtrup
Appl. Phys. Lett. **107**, 073107 (2015); http://dx.doi.org/10.1063/1.4929356

4) Toward optimized surface δ-profiles of nitrogen-vacancy centers activated by helium irradiation in diamond
Felipe Fávaro de Oliveira, **S. Ali Momenzadeh** , Denis Antonov, Jochen Scharpf, Christian Osterkamp, Boris Naydenov, Fedor Jelezko, Andrej Denisenko, and Jörg Wrachtrup
Nano Lett., **2016**, 16 (4), pp 2228-2233, DOI: 10.1021/acs.nanolett.5b04511

5) High-fidelity transfer and storage of photon states in a single nuclear spin
Sen Yang, Ya Wang, D. D. Bhaktavatsala Rao, Thai Hien Tran, **S. Ali Momenzadeh** , M. Markham, D. J. Twitchen, Ping Wang, Wen Yang, Rainer Stöhr, Philipp Neumann, Hideo Kosaka & Jörg Wrachtrup
Nature Photonics **10**, 507-511 (2016), DOI:10.1038/nphoton.2016.103

6) On the efficiency of combined ion implantation for the creation of near-surface nitrogen-vacancy centers in diamond
Felipe Fávaro de Oliveira, **S. Ali Momenzadeh** , Denis Antonov, Helmut Fedder, Andrej Denisenko & Jörg Wrachtrup

Phys. Status Solidi A **213**, No. 8, 2044-2050 (2016), DOI: 10.1002/pssa.201600326

7) Heralded control of mechanical motion by single spins

D. D. Bhaktavatsala Rao, **S. Ali Momenzadeh** , and Jörg Wrachtrup

Phys. Rev. Lett. **117**, 077203 (2016), DOI: 10.1103/PhysRevLett.117.077203

8) Thin circular diamond membrane with embedded nitrogen-vacancy centers for hybrid spin-mechanical quantum systems

S. Ali Momenzadeh , Felipe Fávaro de Oliveira, Philipp Neumann, D. D. Bhaktavatsala Rao, Andrej Denisenko, Morteza Amjadi, Zhiqin Chu, Sen Yang, Neil B. Manson, Marcus W. Doherty, and Jörg Wrachtrup

Phys. Rev. Applied **6**, 024026 (2016), DOI: 10.1103/PhysRevApplied.6.024026

9) Efficient creation of dipolar coupled nitrogen-vacancy spin qubits in diamond

Ingmar Jakobi, **S. Ali Momenzadeh**, Felipe Fávaro de Oliveira, Julia Michl, Florestan Ziem, Matthias Schreck, Philipp Neumann, Andrej Denisenko, and Jörg Wrachtrup

Journal of Physics: Conference Series, **752**, 012001, (2016), DOI: 10.1088/1742-6596/752/1/012001

10) Nuclear Quantum-Assisted Magnetometer

Thomas Häberle, Thomas Oeckinghaus, Dominik Schmid-Lorch, Matthias Pfender, Felipe Fávaro de Oliveira, **S. Ali Momenzadeh**, Amit Finkler, and Jörg Wrachtrup

Review of Scientific Instruments **88**, 013702 (2017), DOI: http://dx.doi.org/10.1063/1.4973449

11) Tailoring spin defects in diamond by lattice charging

Felipe Fávaro de Oliveira, Denis Antonov, Ya Wang, Philipp Neumann, **S. Ali Momenzadeh**, Timo Häußermann, Albert Pasquarelli, Andrej Denisenko, and Jörg Wrachtrup

To be published in Nature Communications